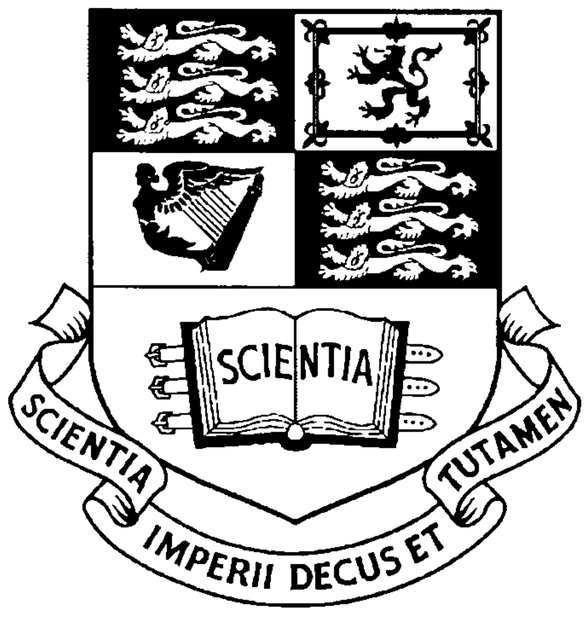
PhD Thesis

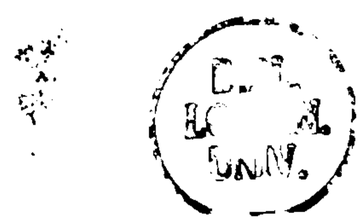


Imperial College

Statistical Methods for Functional Neuroimaging Data

John Alexander David Aston

January 2002



Abstract

Statistical methods are now an intrinsic part of neuroimaging. This thesis concerns two related themes. Firstly, estimation and inference procedures for the analysis of neuroimaging data are developed within a statistical frame of reference. Secondly, the dimensional nature of the data, namely spatial, temporal, and spatio-temporal, is considered and new algorithms and procedures developed to facilitate statistical modelling. Partial Volume Effects, resulting from the limited spatial resolution of the data, are considered within a statistical framework, and an algorithmic solution developed for the case of a general noise model. Temporal compartmental modelling is concerned with the estimation of parameters governing the time course of PET tracer compounds. Statistical methods are developed for not only the estimation of the parameters, but also the error associated with these, allowing inference to be made about changes of the parameter. This is developed in the case of both a-priori known and unknown compartmental structures. Wavelet models allow for full spatio-temporal analysis of the data, and methods for PET and fMRI developed and discussed. Finally, the application of random effects models to neuroimaging data sets is discussed, and a method developed for application to neuroimaging data, using the full spatio-temporal nature of the data.

Contents

Nomenclature **12**

Acknowledgements **14**

1 Introduction **15**

1.1 Statement of Problem 16

1.2 Outline of Thesis 17

1.3 Contributions & Recognition 20

2 Data and Modalities **22**

2.1 Positron Emission Tomography 23

2.1.1 Principles of PET 23

2.1.2 Applications 27

2.2 Magnetic Resonance Imaging 28

2.2.1 Principles of MRI and fMRI 29

3 Current Methods of Analysis **31**

3.1 PET 31

3.1.1 Spatial Modelling 32

3.1.2 Temporal Modelling 33

3.1.3 Spatio-Temporal Modelling 37

3.2 Magnetic Resonance Imaging 38

3.2.1 Spatial Modelling 38

3.2.2 Temporal Modelling 39

3.2.3 Spatio-Temporal Modelling 41

3.3 Statistical Estimation and Inference 42

3.3.1 Mean Squared Error 43

3.3.2 Statistical Parametric Mapping (SPM) 43
3.3.3 Non Parametric Methods 45

4 Partial Volume Correction **47**
4.1 Partial Volume 47
4.2 Spatially Correlated Noise 49
4.2.1 Noise Models 49
4.3 Signal and Variance Estimation 50
4.3.1 The Methods of Labbé and Rousset 54
4.3.2 1-D Simulations 55
4.4 Algorithms for 3-D Solution 57
4.4.1 Tensor Implementation 57
4.4.2 Estimation of $\mathbf{x}$ and $\mathbf{var}(\mathbf{x})$ with Correlated Noise 59
4.4.3 Application 60
4.5 Syringe Simulations / Measured 61
4.6 Flum Simulations / Measured 65
4.7 Inhomogeneity Testing 70
4.7.1 Simulations / Measured 71
4.8 Future Work 72
4.9 Summary 72

5 Non-Linear Compartmental Regression **73**
5.1 PET Compartmental Models 74
5.2 Neuroreceptor Studies 76
5.2.1 Receptor Compartmental Models 76
5.2.2 Synaptic Neurotransmission 78
5.2.3 Reference Tissue Models 79
5.3 Non-Linear Regression 80
5.3.1 Linear Regression 80
5.3.2 Non-Linear Regression 81
5.4 Non-Linear Compartmental Regression 83
5.4.1 Simplified Reference Tissue Model 83
5.4.2 Separable Least Squares 84
5.4.3 Asymptotic Evaluation 85

5.4.4 Stability Analysis 86
5.4.5 Autocorrelation 87
5.4.6 Hypothesis Testing 88
5.5 Validation Studies 91
5.5.1 Simulation Studies 91
5.5.2 Measured Data Sets 96
5.5.3 Limitations 97
5.6 Current Usage of the Methods and Future Ideas 98
5.7 Summary 98

6 Bayesian Spectral Analysis **100**
6.1 PET Spectral Analysis - $SA_{Classic}$ 101
6.1.1 PET Spectral Analysis Bootstrapped Error Estimation - SA_{Boot} . . 102
6.2 Bayesian Data Analysis 102
6.2.1 Gibbs Sampler 103
6.3 Bayesian Spectral Analysis - SA_{Bayes} 104
6.3.1 Constrained Analysis 104
6.4 Simulation Studies 105
6.5 FDG Cortical Studies 110
6.6 Limitations and Future Improvements 110
6.7 Summary 111

7 Wavelet Methods **112**
7.1 Spatial-Temporal Modelling 113
7.2 Wavelets 113
7.2.1 Wavelet Transformations 114
7.2.2 Wavelet Thresholding 117
7.2.3 Wavelets Bases 119
7.2.4 Variance Estimation 120
7.3 Wavelet Denoising in Neuroimaging 123
7.3.1 PET Wavelet Kinetic Modelling 123
7.3.2 Wavelet Anova and Wavelet SPM 124
7.4 fMRI Spatio-Temporal Analysis 124
7.4.1 fMRI Temporal Analysis 125

7.4.2 Simulation Study 126
7.4.3 Measured Data 128
7.5 Future Work - Four Dimensional Wavelet Modelling 129
7.6 Summary 130

8 Random Effects **131**
8.1 Random Effects Models 132
8.2 Current Random Effect Methods 133
8.2.1 SPM Random Effect Model 133
8.2.2 Voxel Pooling 134
8.3 Neuroreceptor Ligand Studies 135
8.3.1 Voxel Pooling 135
8.3.2 Variance Ratio 135
8.3.3 Restricted Maximum Likelihood (ReML) Algorithm 136
8.3.4 Variance Ratio Smoothing 138
8.3.5 Degrees of Freedom 138
8.4 Validation Studies 139
8.5 Summary 141

9 Concluding Remarks **142**

A Mathematical Functions and Algorithms **143**
A.1 Khatri-Rao Row Product 143
A.2 Residuals Bootstrap 143
A.3 Bias Reduction of Autocorrelations 144
A.4 Random Field Theory for Multiple Comparisons 144

Bibliography **146**

List of Figures

1.1 Levels of Estimation and Inference 17

2.1 Raclopride compound labelled with ^{11}C 24

2.2 A Example of a sinogram. 25

2.3 Integral ^{18}F-FDG Image. This is a glucose analogue and can be used as a measure of metabolic rate. 28

2.4 ^{11}C-Flumazenil Image. A summed image of the radioactivity measured during the scan. This radioligand binds to the Benzodiazapine receptor. . . 29

2.5 Structural MRI Image 30

2.6 Functional MRI Image. 30

3.1 Continuum of Analysis for PET 34

4.1 1D PVC Example: (a) (top) Tissue Radioactivity with (*) and without (o) application of PSF, (middle) Tissue Classification (Grey and White only), (bottom) Region Definitions (b) Matrix construction of the recovery problem, where x_{gi} and x_{wi} are the recovered grey and white matter values respectively for region i. 52

4.2 1D PVC Example: Noise Distribution. Histogram: Estimated values, Solid Line: Expected Theoretical Parameter Distribution. X-axis: estimated parameter values, Y-axis: probability. This data is simulated using a heterogeneous correlated and homogeneous uncorrelated noise model. The presented method uses this noise structure, whilst the methods of Labbé and Rousset have implicit assumptions about the noise. This figure is intended as a graphical representation of the performance of the differing methods in differing noise situations. 56

4.3 Tensor Operators for Problem and Solution in Three Dimensions 58

4.4 Definition of the 5 regions (including background) for the syringe data set represented by different grey levels (corresponding to R). 62
4.5 Measured Syringe Data: (top) 10s acquisitions (one half life apart), (bottom) 120s acquisitions (one half life apart). 65
4.6 Flumazenil Data Set : (a) Definition of the 43 regions for the flumazenil data set represented by different grey levels (corresponding to R). (b) grey (c) white and (d) CSF tissue classification probabilities (corresponding to T). 66
4.7 Flumazenil (a) Volume of Distribution and (b) standard deviation data prior to correction. 67
4.8 Simulated Flumazenil data projected onto MRI template. 68
4.9 Measured Flumazenil data projected onto segmented MRI template; (a) Total (b) Grey Matter (c) White Matter (d) CSF. 69
4.10 Typical Krylov iterations for simulated syringe. 71

5.1 The assumptions allowing the full model to be characterised by a single compartmental structure. These assumptions can be made in both the reference and plasma input function cases, and is here demonstrated for the plasma input case. 76
5.2 A typical binding potential parametric map for $[^{11}C]$SCH23390. 78
5.3 Diagramatic Representation of Synaptic Neurotransmitter Release 78
5.4 The Simplified Reference Tissue Model. 79
5.5 Temporal Variance Model 83
5.6 Simulated Parameter Distributions (derived from 5000 noisy realisations) and their theoretical estimated distributions (derived from Eqn 5.19) for the simplified reference tissue model. 86
5.7 ΔK_1 - Δk_3 surface plots for 1000 simulated TACs showing the effects of simulated changes in K_1 and k_3 on the estimated BP. (i) ΔBP (ii) ΔBP sd 87
5.8 Durbin-Watson Test Statistic derived from simulated $[^{11}C]$SCH 23390 baseline scans. Mean DWTS image from 6 scans, indicating no autocorrelation. The DWTS has a value in the interval [0,4], where 0 and 4 equate to positive and negative correlation, while 2 indicates no correlation. 88
5.9 Group Level Inference 89

5.10 Scheme for generation and analysis of simulated data. Characteristic TACs are assigned to each region of a segmented MRI. This enables generation of the dynamic PET data, which are subsequently fitted with the reference tissue model to generate images of model parameters and their SDs 92

5.11 Simulated [^{11}C]SCH 23390 study with six subjects, each having a baseline and activation scan. In the activation scan there is a 20 % reduction in k_3 in the striatum and frontal cortex for the duration of the scan (90 min). Statistical map of the change in BP; (a) Residuals t test (t > 4.7, P < 0.05 corrected); (b) Standard t test (t > 23.4, P < 0.05) 94

5.12 Simulated [^{11}C]SCH 23390 study with six subjects, each having a baseline and activation scan. In the activation scan there is a 10 % reduction in k_3 in the left caudate for the duration of the scan (90 min). Statistical map of the change in BP with the residuals t test (t > 4.7, P < 0.05 corrected). . . 95

5.13 Single subject: simulated [^{11}C]SCH 23390 study with a baseline and activation scan. In the activation scan there is a 20 % reduction in k_3 in the left caudate for the duration of the scan (90 min). Statistical map of the change in BP with the residuals t test (t > 4.7, P < 0.05 corrected). 95

5.14 Voxel by voxel plot of t values obtained by the residuals method and by pooling over groups, for 12 simulated [^{11}C]SCH 23390 scans. The high correlation supports the assumptions made in the residual method. 97

6.1 Subject Level Estimation and Inference 106

6.2 Compartmental model structures for simulated data sets. Dotted boxes indicate simulated PET data. 106

6.3 Convergence and Stability of Estimates of Mean and Std 109

6.4 NNLS ($SA_{Classic}$; SA_{Boot}) and Bayesian (SA_{Bayes}) fits to the real FDG PET data 111

7.1 1-D Signal and wavelet transform 116

7.2 Tomographic 2-D Example Signal and Battle-Lemarie wavelet transform . . 116

7.3 Battle-Lemarie Wavelet Basis Quadrature Filters. 120

7.4 Subject Level Estimation 123

7.5 Simulation Template 126

7.6 MSE for different thresholding procedures. 127

7.7 Variance Images for Hard Universal thresholding procedures. 128

7.8 Estimation of Effect for Wavelet and Image based methods. 129

8.1 Population Level Inference 131

8.2 Standard deviation image of BP generated from 34 normal subjects who each underwent two $[^{11}C]$SCH 23390 scans. The sd map is in colour overlayed on the average MRI from all the subjects. The sd distribution has anatomical structure, with high sd in areas of high ligand binding. This precludes the use of pooling the sd over voxels. 136

8.3 Mean Binding Potential Image of Control Data. 139

8.4 Variance Ratio Smoothing. 140

List of Tables

4.1 Results from partial volume correction of simulated syringe data (Syringe diameters 14.8, 11.9, 8.6 and 4.7mm) from Rousset, Labbé and Presented method: value with no correction (NC) value after correction ($\hat{x}$) and estimated standard deviation of value ($sd(\hat{x})$). 63

4.2 Results from partial volume correction of measured syringe data (Syringe diameters 14.8, 11.9, 8.6 and 4.7mm) from Rousset, Labbé and Presented method: value with no correction (NC) value after correction ($\hat{x}$) and estimated standard deviation of value ($sd(\hat{x})$). 64

4.3 Results from simulated [^{11}C]flumazenil data set: Grey Matter (GM) and White Matter (WM) V_D values recovered by partial volume correction (Rec) for a representative set of anatomical regions. 68

4.4 Results from measured [^{11}C]flumazenil data set: Grey Matter (GM) and White Matter (WM) V_D values recovered by partial volume correction (Rec) for a representative set of anatomical regions. 70

5.1 Simulated and Measured [^{11}C]SCH 23390 Data Set Results 96

6.1 Rate constants used for the simulated tracer data sets 107

6.2 Summary of results for the 4 PET tracer simulations 108

6.3 Summary of results for the real FDG data 110

7.1 MSE Mean and Max Values for Analysis Methods across the Image 127

Nomenclature

Λ	Diagonal Operator: vector to matrix diagonal or visa versa
λ	Decay Constant, Threshold Value
$\odot$	Khatri-Rao Product
$\otimes$	Kronecker Product
τ	Relaxation Parameter
IRF	Impulse Response Function
b	PET data
BP	Binding Potential
C_P	Plasma Concentration
C_R	Reference Tissue Concentration
C_T	Tissue Concentration
H, G	Quadrature Mirror Filters
IW	Inverse Wavelet Transform
k	Biological Rate Constants
K_I	Irreversible Rate Constant
n	Number of Pixels
P	Point Spread Matrix
R	Region Definition Matrix

R_1 Relative Rate of Delivery

T Tissue Definition Matrix

$T(w, \lambda)$ Threshold

V_D Volume of Distribution

W Weighting or Wavelet Matrix

w Wavelet Coefficient

Var Variance

SSQ Sum of Squares

Acknowledgements

Throughout my PhD I have had great cause to be grateful to many people. Firstly to my supervisors, Dr Roger Gunn, Professor Keith Worsley and Professor Vin Cunningham, without whose tireless support and encouragement this thesis would not have been completed. I am also indebted to Dr Federico Turkheimer, for sharing both an office and his many ideas, and to Professor Alan Evans and Dr Alain Dagher for their encouragement and support during my time in Montreal. I would also like to thank the staff and researchers at the MRC Cyclotron Unit, McConnell Brain Imaging Center and the McGill Mathematics and Statistics Department for all of their help in explaining the data, useful discussions about its analysis and their ability to cope with my frequent disappearance to the other side of the Atlantic.

I would like to dedicate this thesis to my Mum, Dad and Brother.

Chapter 1

Introduction

The aim of neuroimaging is to enhance understanding of the brain through in-vivo measurement of physiological processes. Neuroimaging is an achievement of science transcending boundaries between different fields. It allows clinical and medically driven research questions to be answered through the use of Physics, Chemistry, Biology, Engineering, Mathematics and Statistics. No other scientific discipline can claim to have created such co-operation.

Neuroimaging data sets provide the unique opportunity to experiment within an in-vivo environment. Most research into the brain has previously relied on post-mortem data which, while providing much information on the physical structure of the brain, revealed little in the way of knowledge about the underlying systems and the neurological processes involved. Neuroimaging techniques are constantly advancing, providing better and more extensive methods of understanding these underlying processes, and the interactions between the different physical systems.

This thesis concentrates on the application of statistics to neuroimaging data sets. Statistics is at the forefront of neuroimaging, and indeed much statistical research is driven by its immediate application to neuroimaging. Whilst some theory is developed here, the major goal of this thesis is to enhance and develop statistical methods, based on theoretical results, to allow inference and estimation of biological parameters of interest within neuroimaging data sets.

1.1 Statement of Problem

Neuroimaging has a tendency to analyse problems from two differing standpoints. The first point of view is that of quantification, in so much that estimation of the signal is the single most important property that can be derived from the data, whilst the second is that of inference, where the most important information is whether the signal has changed regardless of the underlying quantification of that change. This tends to ignore the advantages of an analysis combining both these approaches. However, in recent years, it has become increasingly obvious that the most effective methods of analysis are those which implement methods to both estimate the signal and determine the error on that signal such that inference can be made.

The aim of this thesis is to provide new methods for the analysis, estimation and inference of neuroimaging data through the use of statistical methods and algorithms. There are several areas of neuroimaging where statistical methods have so far been unavailable as the emphasis has been placed on signal estimation, without direct reference to underlying noise models. The methods developed in this thesis combine both these ideas, such that error estimates can be made, along with determination of the underlying signal.

The methods in the thesis are considered in terms of two differing emphases. The first emphasis is that of the dimension of the analysis. Neuroimaging data is usually four dimensional and as such the analysis can be concerned with one of three possibilities; Spatial, Temporal or Spatio-Temporal Analysis. The methods presented here are classified according to the dimension of the data that is modelled, as consideration of the data dimension leads to the application of different techniques based on the data type. This is often not explicitly considered, but can yield insight into the analyses, which would be lost without formulation of the problem in this way.

Secondly, the estimation and inference can be carried out at one of three observational levels (Figure 1.1). These levels determine the error variances that are considered in the analysis. The first level is that of subject analysis. Here the estimation and inference are concerned with the data from a single subject and are primarily connected with experimental or measurement variance. The second level is that of the group, where a set of subjects provide a case study, with no generalisation outside the group. The final level is that of the population, where the group is considered to be a representative sample of the population as a whole, and the variance associated with the population must be considered.

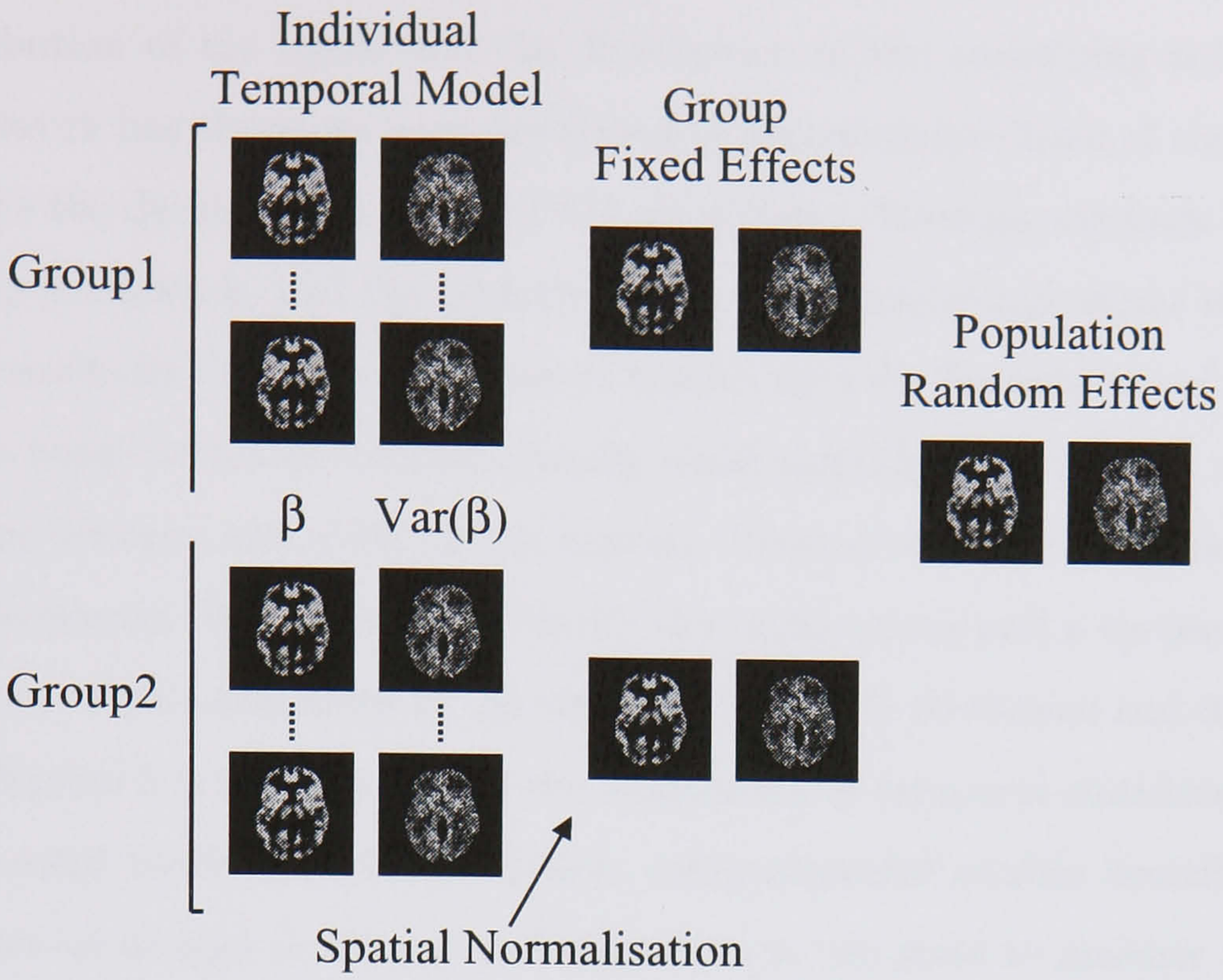


Figure 1.1: Levels of Estimation and Inference

1.2 Outline of Thesis

The thesis runs through the themes of Spatial, Temporal and Spatio-Temporal modelling. These follow the classical order of data analysis, and the interpretability of results in terms of, first, region of interest data (spatial modelling), then voxel by voxel analysis (temporal modelling) and then full temporal modelling dependent on spatial constraints or models (spatio-temporal modelling).

Chapter 2 gives a brief introduction to the data. There are two main data types interrogated using the new methods, that of PET and fMRI. Chapter 3 gives an overview of some other methods that are currently used to analyse the data, and the statistical methods involved in answering clinically derived questions from the experimental designs currently used. The novel frameworks for analysis, methods and algorithms developed in this thesis are contained in chapter 4 to chapter 8.

Chapter 4 details the statistical methods for analysis of the partial volume correction (PVC) problem. Partial volume effects occur due to the blurring of the signal by the point spread function of the tomograph. These effects result from the heterogeneity at tomographic resolution of both the different regions in the brain, and the different tissue types in those regions. PVC has previously been analysed purely as a signal recovery problem.

However, the formulation of appropriate algorithms for PVC is dependent on both the distribution of the signal and the distribution of the underlying noise. A mathematical framework has therefore been developed to accommodate both of these factors and to facilitate the development of new PVC algorithms. Previous methods have been described in this framework, and the underlying implicit assumptions about the noise clarified for these methods. The incorporation of tensors into the formulation of the problem has led to the construction of computationally rapid algorithms taking into account both heterogeneity between and within brain regions. These methods are assessed on both simulated and measured PET data sets. Finally the implications and a theoretical method for the analysis of inhomogeneity in the classified regions is developed and discussed.

Chapter 5 is concerned with the application of temporal statistical modelling to compartmental model structures. Linear compartmental models describe, in simple terms, the rate of change in time of radioligand from one state to another assuming first order differential kinetics. This yields non-linear models for the data in terms of the parameters of interest. Previous methods for the analysis of these data have concentrated on solution of the model, without estimation of the errors associated with the estimates of the parameters. Through the use of non-linear regression theory, a novel analysis of PET compartmental model errors is developed which allows for estimation of both the parameters and the errors associated with them. The assumptions of the model are formulated and if possible assessed. The method is then validated using both simulated, from a realistic PET simulator, and measured PET data. Finally a review of the usage of these methods in experiments by other groups is presented.

Ideas from bayesian analysis are then incorporated into temporal models, in chapter 6. Bayesian methods differ from classical statistical methods based on the underlying assumptions about the data and the parametric representation of it. These methods can be especially useful in situations where there is prior knowledge about the parameters. This is the case in PET Spectral Analysis (Cunningham and Jones, 1993) where parameters from temporal model solutions are assumed to be non-negative. This constraint leads to great difficulty in classical estimation of errors on the parameters. Through the use of bayesian analysis, the prior knowledge that these parameters are non-negative is incorporated into the estimation procedure, as with classical Spectral Analysis, but in addition incorporated into the estimation of the errors on those parametric estimates. The bayesian methods employed are empirical, and as such distributions of the parameters are generated numer-

ically. These methods are assessed with both simulated and measured PET data, and compared to the estimates from Spectral Analysis, and previously proposed non-bayesian empirical methods for the estimation of the errors.

Wavelets are now routinely used in the signal processing and image restoration fields. This is due to the properties that well chosen wavelet transforms impart to the data. Neuroimaging is no exception in the recognition that the use of wavelet transforms might provide a more efficient estimation space for parameters. Chapter 7 continues on from previous work in spatial wavelet modelling to investigate spatio-temporal modelling particularly in fMRI. The wavelet transform provides a spatial model that is then temporally solved using current statistical models for fMRI time series, and then the parameters thresholded in wavelet space. The inverse transform is then applied to produce parametric images in the original image space. A novel method for the estimation of the errors of the image space parameters is also presented based on the decorrelating properties of the wavelet transform. The analysis is then investigated with both simulated and measured fMRI data, and compared to the analysis using the temporal model in image space alone.

No thesis on statistical methods in neuroimaging would be complete without mentioning the problems and methods of analysis of random effects, and this is indeed discussed in chapter 8. Random effects models are the current 'in-vogue' statistical issue in neuroimaging, and as such methods of analysis for these models are required. This chapter firstly introduces the random effects model, and reviews other methods for its solution. A method is then presented for the analysis of random effects using variance ratio smoothing. This method estimates the variance of both the fixed and random components of the data, and using the ratio of the two, which displays greater homogeneity than the original random variance map, then develops a smooth estimate of the random variance component. This increases the sensitivity, as the degrees of freedom are increased due the large number of degrees of freedom in the fixed effects model, as compared with the small number in the random effects model. The method is then validated for PET neuroreceptor ligand data, using the data from chapter 5.

Finally chapter 9 gives a brief summary of the novel methods developed in this thesis, as well as commenting on some areas where these ideas may be developed as future work.

1.3 Contributions & Recognition

The main contributions of this thesis are the introduction, development and validation of novel methods for the construction of neuroimaging problems, and the new algorithms and methods for their solution. The formulation of the problem in terms of the dimension of the data to be analysed allows for the exploitation of the many similarities in different methods. This would not be explicit were it not for the formulation of the problem in terms of spatial, temporal and spatio-temporal data types, and the underlying intrinsic properties of data in these dimensions.

- The formulation of PET Partial Volume Correction in a statistical framework. This allows the comparison of previous methods in terms of their implicit noise models. It also leads to new methods for the correction of data, allowing explicit noise models to be used. Novel rapid tensor algorithms based on the inherent spatial structure of the data have also been developed and their convergence assessed.

- The development of a statistical framework for the analysis of compartmental models for PET neuroreceptor ligand data sets through the use of non-linear regression. This allows inference to be made about data in experimental designs where this was not previously possible. This is achieved through the estimation of errors of the parameters using the residuals to the compartmental model. The assumptions associated with such an analysis have been formulated and assessed.

- The development of a novel method of estimation of the non-negatively constrained parameters generated by PET Spectral Analysis, and the estimation of distributions of these parameters. This is achieved through the use of bayesian techniques, more specifically the Gibbs sampler. This allows a more knowledgeable assessment of both the concept of Spectral Analysis and the effect of noise on the estimation of parameters.

- The application of wavelets to 4-D neuroimaging data sets, through the use of linear temporal models in the spatial wavelet domain, especially in fMRI applications. A novel formulation of error estimates of the thresholded parameters in image space has also been developed, leading to possibilities of application of wavelets in most current linear image space analysis methods.

- The application of random effects models to the data sets generated using the tem-

poral modelling methods. This includes the development of a method with increased sensitivity using the spatial nature of the data and the validation of these variance ratio methods for PET neuroreceptor ligand studies.

The work presented in this thesis has contributed either wholly or in part to the following journal publications.

- **Aston, J.A.D.**, Cunningham, V.J., Asselin, M.C., Hammers, A., Evans, A.C., and Gunn, R.N. Positron Emission Tomography Partial Volume Correction. *Journal of Cerebral Blood Flow and Metabolism*, in press.

- **Aston, J.A.D.**, Gunn, R.N., Worsley, K.J., Ma, Y., Evans, A.C., and Dagher A. A Statistical Method for the Analysis of Positron Emission Tomography Neuroreceptor Ligand Data. *Neuroimage* **12**:245-256 (2000).

- Turkheimer, F.E., **Aston, J.A.D.**, Banati, R.B., Riddell, C., and Cunningham, V.J. A linear wavelet filter for parametric imaging with dynamic PET. *IEEE Transactions on Medical Imaging*, in press.

- Turkheimer, F.E., Brett, M., **Aston, J.A.D.**, Leff, A.P., Sargent, P.A., Wise, R.J.S., Grasby, P.M., and Cunningham, V.J. Statistical Modelling of positron emission tomography images in wavelet space. *Journal of Cerebral Blood Flow and Metabolism* **20(11)**:1610-1618 (2000).

- Turkheimer, F.E., Banati, R.B., Visvikis, D., **Aston, J.A.D.**, Gunn, R.N., and Cunningham, V.J. Modelling dynamic PET/SPECT studies in the wavelet domain. *Journal of Cerebral Blood Flow and Metabolism* **20(5)**:879-893 (2000).

- Worsley, K.J., Liao, C., **Aston, J.A.D.**, Petre, V., Duncan, G.H., and Evans, A.C. A general statistical analysis for fMRI data. *Neuroimage* **15(1)**:1-15 (2002).

- Dagher, A., Bleicher, C., **Aston, J.A.D.**, Gunn, R.N., Clarke, P.B.S., and Cumming, P. Reduced dopamine D1 receptor binding in the ventral striatum of cigarette smokers. *Synapse* **42(1)**:48-53 (2001).

The work also received the following recognition

Young Investigator Award, *Neuroreceptor Mapping 2000*, New York. (Estimation and Errors in Partial Volume Correction).

Chapter 2

Data and Modalities

Neuroimaging is now a multimodality discipline where no one imaging technique can be considered without reference to others either explicitly in the experiment or implicitly in the complimentary knowledge which aids understanding. There are two main areas in neuroimaging; Structural Imaging and Functional Imaging.

Structural Imaging is concerned with anatomical definition and localisation. This has its origin in drawings from post mortem studies, and has a long tradition in neuroanatomy. Current techniques include high resolution magnetic resonance imaging (MRI), where high strength magnetic fields are used to acquire high resolution ($\sim$ 1mm) three dimensional images.

Functional Imaging is concerned with quantification of neuronal activity, through either direct measurement or the measurement of associated physiological processes. This has its origins in Electroencephelograpy (EEG), where evoked potentials are measured, arising from electrical output of neurons (firing). Techniques are continuously being introduced, refined, updated, but the major techniques currently in use continue to be Positron Emission Tomography (PET), functional Magnetic Resonance Imaging (fMRI), EEG and Magnetoencephelography (MEG).

This thesis is primarily concerned with the analysis of functional imaging data sets, specifically PET and fMRI. This analysis includes both the testing of experimental hypotheses and the quantification of biological parameters of interest.

2.1 Positron Emission Tomography

Positron Emission Tomography is an imaging technique that uses radioisotopes to image *in vivo* physiological processes. The three principle types of physiological processes well suited to PET measurement are regional Cerebral Blood Flow (rCBF), metabolic rate and characterisation of neuroreceptor sites. These processes are fundamental to the many neurological systems, and deviations from normal are casual or symptomatic of many neurological or psychological diseases, eg Schizophrenia and Parkinson's diseases. However before considering the roles these process play in different systems, it is important to understand the principles of PET measurement, in order to fully appreciate the experimental ideas that can be investigated using this imaging technique.

2.1.1 Principles of PET

PET is probably best described as the interaction of many different disciplines to achieve a common result; a 4-D data set. These different disciplines range from the starting Chemistry, through the Physics of the scanner, and the Engineering that makes this possible, to the Mathematics and Statistics of the reconstruction and data correction. This is all carried out in a clinical framework in an effort to understand the underlying Biology, making this a truly multidisciplinary approach. The precise nature of the data set is determined by the experimental question it is being used to address, and by the limitations set by each stage of the data acquisition.

There are many excellent descriptions of the PET data acquisition and reconstruction process and the underlying problems involved (Muehllehner and Colsher, 1982; Holmes, 1994). The descriptions below are a very concise overview of the issues involved.

Radiochemistry

The fundamental principle behind PET is that of positron decay. A unstable positron emitting radionucleide can be produced by bombardment of stable nuclei with accelerated protons or deuterium ions (Comar et al., 1982). These ions can be accelerated using a cyclotron. For example ^{15}O can be produced by bombardment of Nitrogen with deuterium. These positron emitting radioisotopes can then be used to label different compounds, and an example of which is given in Figure 2.1.

Positron emission occurs randomly from the unstable nuclei. The positron then travels a short distance (up to a few millimeters in tissue) before it annihilates an electron. This

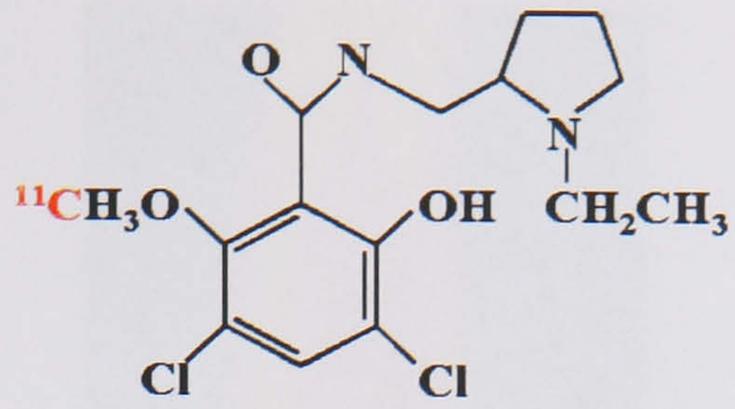


Figure 2.1: Raclopride compound labelled with ^{11}C

annihilation results in the release of energy in the form of two (almost) colinear gamma rays. These gamma rays are emitted at the point of annihilation rather than the point of decay which leads to an intrinsic blurring in the measurement. This is a gross simplification of the true process, with all the above steps involving probability distributions on all the parameters in the process. However the principles of the PET scanner are derived from the ability to detect the coincident gamma rays.

The Scanner

The PET scanner is designed to detect the resulting gamma rays that are emitted from the annihilation of the positron with an electron. Photosensitive compounds have particular properties, in that when a photon in a specific energy range hits the surface of these compounds, the photoelectric energy is converted via a photomultiplier tube into an electrical signal. As these gamma rays occur in pairs coincidently, an event is said to be recorded if two of these electrical signals are recorded within a defined time window (of the order of 20 nanoseconds). This localises the position of the annihilation to a line between the two coincident detectors. A PET scanner consists of a set of rings of detectors. New PET scanners are increasingly employed in three dimensional mode. Any detector in any ring can be paired with any other detector, allowing a fully three dimensional spatial data set to be collected.

Thus, from a record of these events, a spatio-temporal data set is derived. This data set comprises the time the event occurred and the detector pair that was involved. This data set is called a sinogram (Figure 2.2), and is a set of counts of the coincident detector pairs during a given time.

Reconstruction

Having collected the data in the form of a sinogram, it is necessary to reconstruct the data into the usual format such that it is able to be analysed in a framework that is easily



Figure 2.2: A Example of a sinogram.

understood. There are two main types of reconstruction that are currently used; Filter Back Projection and Iterative Reconstruction.

Filter back projection is essentially a linear transformation of the sinogram back into image space. Each detector pair in the sinogram can be associated with a voxel in the image depending on the probability that an event at that voxel would lead to a coincident detection for that pair of detectors. It has the advantage that it is linear and analytic, and so is non-iterative, and results in the same reconstructed data each time. Filter back projection is the most frequently used reconstruction technique.

Iterative reconstruction is based on the expectation maximisation procedure (Lange and Carson, 1984). These methods are based on statistical estimation methods, which incorporate the noise characteristics and other physical properties of the scanner. Fourier methods such as filter back projection are deterministic in nature as opposed to the stochastic nature of the iterative reconstruction algorithms. There is also the possibility to build into the iterative models, prior knowledge about the system, and use this to aid the reconstruction.

The acquisition of the data in PET is not without its problems. Although the principle of the data collection is simple, there are practical problems that have to be accounted for in the reconstruction process. Whilst there are many things to account for, four main problems need to be mentioned. Firstly, normalisation is necessary, as there is non-uniformity in both the detector pair sensitivity and geometry of the scanner. Attenuation must also be accounted for. This is easy, in principle, if the attenuation coefficients are known, but practically these are not, and these have to be estimated, usually using a transmission scan. Thirdly, there is scatter, which occurs when the emitted photon(s) is deflected and the line between the coincident detectors does not contain the annihilation

point. The final problem that must be accounted for, is randoms. These are when multiple events occur and two photons from differing events are recorded as an event whilst not being from the same annihilation. There are many methods to correct for these different problems which can be built into both filter back projection and iterative reconstruction.

The aim of reconstruction is to produce an image which is primarily composed of signal, whilst still having the ability to characterise the noise in the image. Iterative reconstruction reduces the noise of the image compared with filter back projection but the noise which remains is very difficult to characterise. The image is composed of voxels, which are usually quantified into counts if quantification is available. Voxels are also often known as pixels, although strictly voxels refer to "volume elements" in 3-D images whilst pixels refer to "picture elements" within 2-D images. These size of the voxels are determined by the reconstruction and the resolution of the scanner.

PET studies are usually temporally combined into a series of temporal frames. Typical PET receptor ligand studies have 20-35 frames, whilst blood flow studies often only have one temporal frame (static image). The number of frames depends both on the kinetics of the ligand, as well as the half-life of the radioisotope. For example ^{15}O has a very short half life ($\approx$ 2 mins) whilst ^{18}F has a longer half life ($\approx$ 110 mins). However the half life must be short enough that the number of counts required for a PET scan will not continue to be emitted within the subject for any longer than necessary. This acquisition sequence yields a rich spatio-temporal data set. Typically it has dimensions of 128 x 128 x 91 x 30 in the newest 3-D scanners.

Tracer Studies

The experimental protocol which results in the above data collection needs to be grounded in a design that allows an understanding of the underlying system under observation. The typical goal in PET experiments is to mimic in some way the properties of the system, whilst the experiment itself does not alter these properties. This is known as a tracer protocol, where the ligand is present only in tracer quantities, and hence does not change the balance in the system itself.

This leads to important design issues for the manufacture of the radioligand. It is important that the proportion of labelled ligand to unlabelled be high, as this facilitates using the minimal amount of ligand for a specified dosage of radioactivity. Whilst this may be an easy principle to follow in theory, often in practice the proportional yield may

be much lower than ideal, and tracer assumptions must be verified or the ligand discarded.

2.1.2 Applications

PET can be used in a wide variety of applications. These are certainly not limited to neuroimaging, or even solely clinical. However, this thesis is concerned with neuroimaging data sets and as such the applications to PET to this type of data will be the main consideration.

The three main applications of PET in neuroimaging involve different experimental protocols and different radioligands. The types of study and the requirements of the experiment also dictate the types of radioligand that is needed.

Blood Flow Studies

Blood flow studies are performed most commonly using ^{15}O-radiolabeled tracers. These tracers are combined with other compounds in the body to produce radiolabelled water. For example, the continuous inhalation of ^{15}O-Carbon Dioxide provides a steady arterial infusion of ^{15}O-Water (Jones, 1982). ^{15}O-Water can also be made directly and infused into the subject. If the measurements of the tomograph are calibrated with an arterial blood concentration, quantification of rCBF can be achieved.

Blood flow studies were of much initial interest in neuroimaging as it was assumed that neuronal activation was linked with increased blood flow, and thus blood flow studies could be used to investigate brain function. However, with the advent of fMRI, where no radioactivity is needed, blood flow studies are becoming less frequently used, except in certain situations where fMRI is not appropriate.

There are probably more methods of analysis for blood flow studies than any other PET technique. This is partly due to the fact that water studies are easier to perform in terms of chemistry than other studies. This is no longer the case with the advent of fMRI which can now do similar activation studies without the need for radioactivity, chemistry and over a shorter temporal time frame.

Metabolic Rate Studies

Metabolic rate studies are most often performed using the glucose analogue ^{18}F-FDG. This is a tracer analogue of glucose, and hence a tracer for the mechanism of metabolism. Metabolism studies are of growing clinical importance. It is expected that tumours are

growing rapidly - far more rapidly than other cells in the body. This is often the basis of treatment. Cells that grow rapidly will require more glucose, and hence there will be greater uptake of the tracer. This allows the tracer to become a marker for cancerous cells.

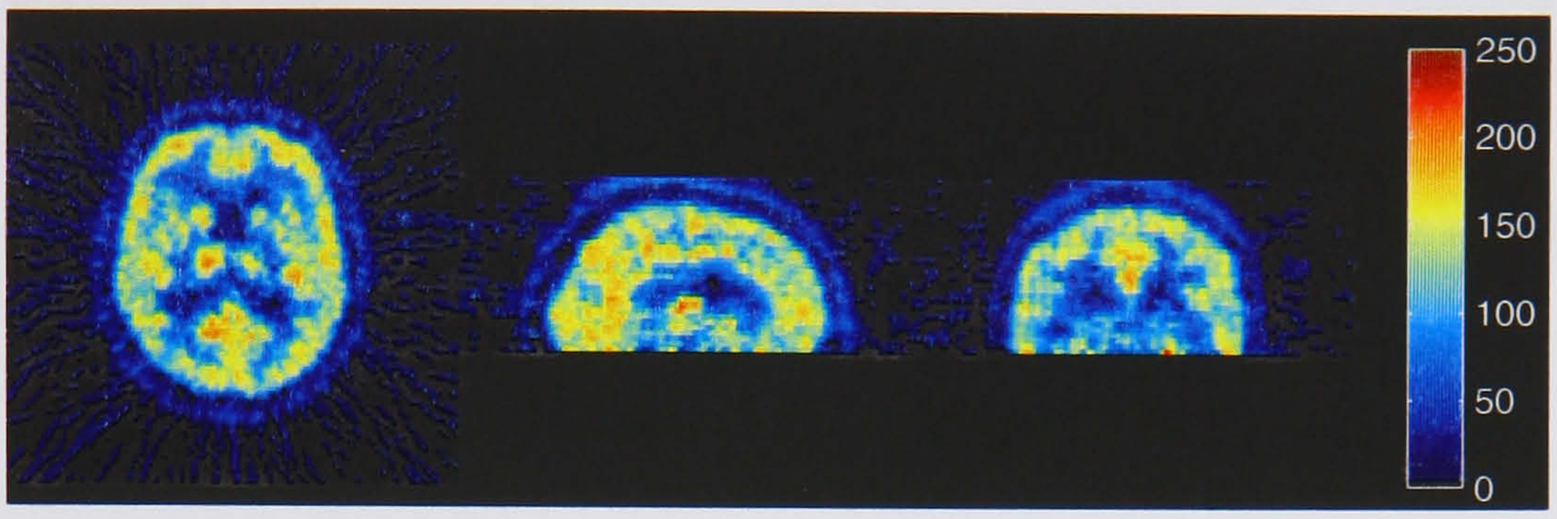


Figure 2.3: Integral ^{18}F-FDG Image. This is a glucose analogue and can be used as a measure of metabolic rate.

An example of an ^{18}F-FDG image is shown in Figure 2.3. Metabolic rate studies can also be used to look at regions of the brain where metabolism has slowed or even stopped. This may be of use in such diseases as Alzheimer's, where the cause may be due to atrophy in certain regions.

Neuroreceptor Studies

The fastest growing area of clinical research in PET is that of neuroreceptor studies. This is an area which is well suited to study with PET, and no alternative has yet been shown to allow *in vivo* imaging, as fMRI has with blood flow. Tracers can be designed to target particular transmitter systems, such as the Benzodiazapine (Figure 2.4), Dopamine or Seratonin systems. However this is a complicated process and there is much still to be done in terms of producing different ligands to allow this, and the analysis which will be associated with these ligands. However, many ligands now do exist and can be used to analyse these different systems.

2.2 Magnetic Resonance Imaging

Magnetic Resonance Imaging has emerged as a major tool in both clinical and research based neuroimaging. Structural imaging used MRI is now routinely used in clinical practice, just as X-rays are used in skeletal imaging. Functional MRI or fMRI is now the most widely used form of research based neuroimaging, due to the ease of adaptation of clinical

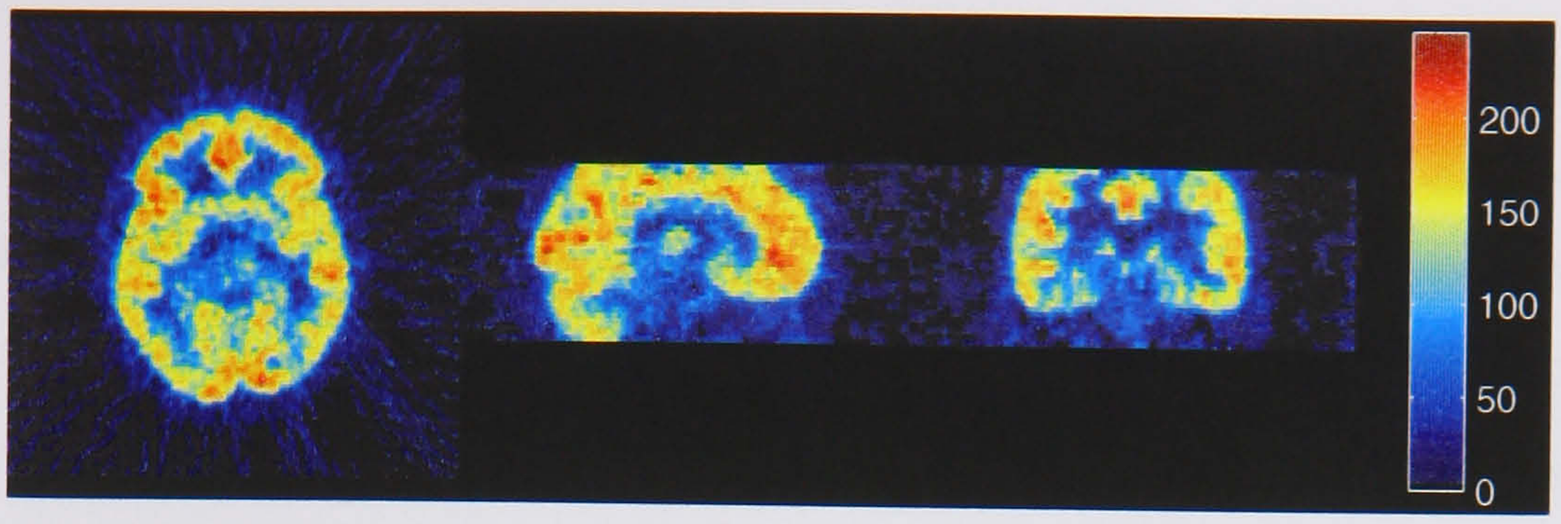


Figure 2.4: ^{11}C-Flumazenil Image. A summed image of the radioactivity measured during the scan. This radioligand binds to the Benzodiazapine receptor.

scanners to allow functional experiments to be performed.

The following is a much simplified expression of the principles behind MRI and fMRI. Much more detailed explanations are widely available (Westbrook and Kaut, 1998).

2.2.1 Principles of MRI and fMRI

The MRI signal derives from the protons in the water contained in tissue (Turner et al., 1997), and whilst the image intensity is dependent on the proton density, it is also profoundly affected by the local environment. The protons themselves act as 'magnets' and are aligned randomly throughout, but when a strong magnetic field is applied, these all align with the external field (Westbrook and Kaut, 1998).

Radio Frequency (RF) Signals and Pulsing

The MR signal itself is the result of resonance (Westbrook and Kaut, 1998). When an RF pulse of energy at the resonant frequency of the hydrogen atom is delivered, this causes the magnetisation to move out of alignment. This movement of the magnetic field, by Faraday's Law, induces a current in a receiver coil. If the RF signal is stopped, these relax into their original states with decay constants T1 and T2, T1 being the magnetisation in the longitudinal plane and T2 being in the transverse plane. Different materials have different T1 and T2 times, which yields different intensity signals from different materials. The RF signals are pulsed with certain repetition times producing contrasts in the images.

K-Space

The images themselves result from gradients in the magnetic field. Firstly the signal is localised to a slice using a gradient along the z axis, isolating a particular slice. This is of particular importance in functional MRI, as the slices will not be collected at the

same time. Therefore responses will be measured at different times in different slices. The resonant frequency (precessional frequency) is dependent on the magnetic field, and therefore the position of a nucleus can be determined from the frequency of excitation within the gradient field. There is also a phase gradient which alters the phase of the signal, and using the frequency and phase gradients, it is possible to localise the signal. This is known as K-space. There exists a fourier relationship between K-space and Image space, and as such a fourier transform of the K-space data yields the image. An example

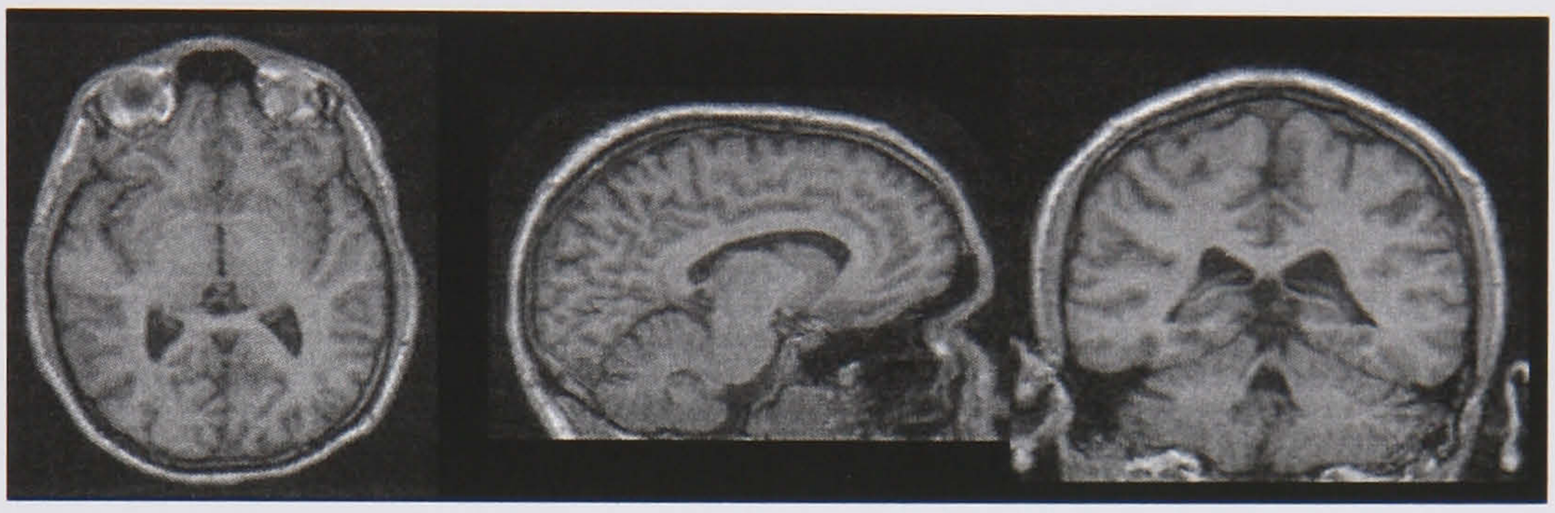


Figure 2.5: Structural MRI Image

of an MRI image is shown in Figure 2.5.

Blood Oxygenation Level Dependent Signal

It was noticed that deoxyhaemoglobin in blood is more paramagnetic than oxyhaemoglobin (see review by Turner et al (1997) for more information). Therefore if the level of oxygenation in blood is changed so are the magnetic properties, and this can act as a contrast agent. This was shown by Ogawa (Ogawa et al., 1990) and others to be sufficient to be seen with an MRI, and this procedure was dubbed 'blood oxygenation level dependent' contrast. This discovery resulted in functional MRI (Figure 2.6).

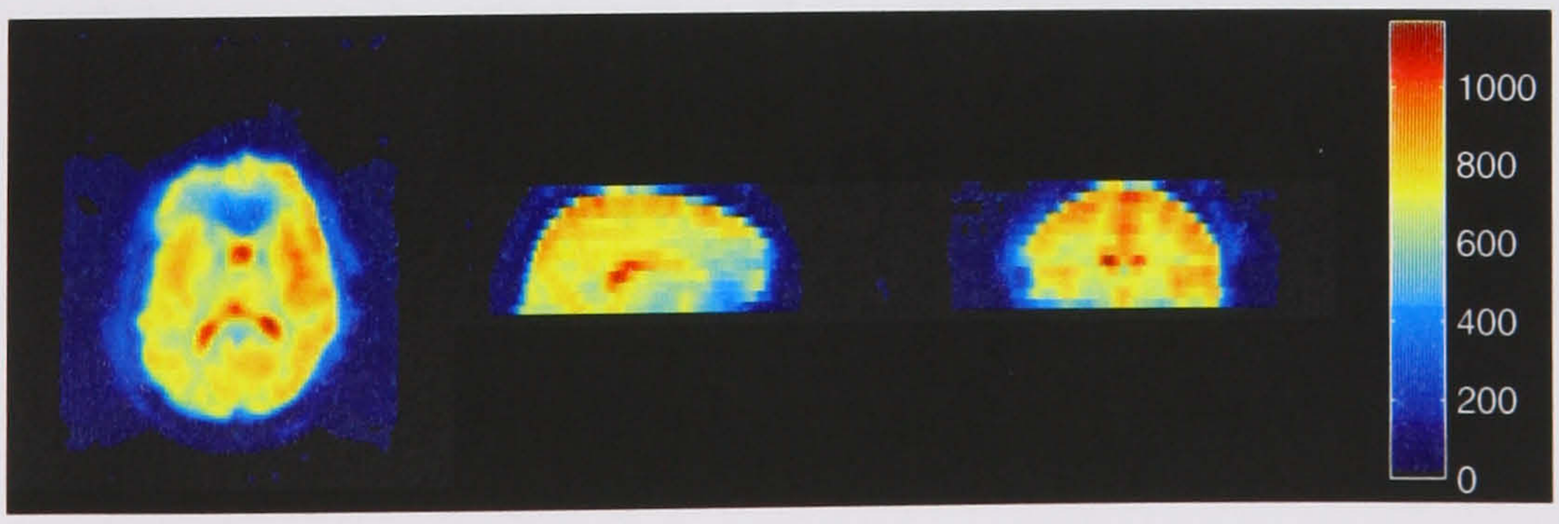


Figure 2.6: Functional MRI Image.

Chapter 3

Current Methods of Analysis

There are many methods of analysis of both PET and fMRI data sets. These methods, whilst often being different, with differing spatial, temporal and spatio-temporal components, often utilise similar principles of analysis, as whilst the data sets are different, the intrinsic experimental questions that are asked are often the same.

The methods described in this chapter for PET and fMRI are some of the current methods used for analysis. This is by no means a complete summary and new methods are continuously being developed and refined.

3.1 PET

One of the primary advantages of PET is that it can be used quantitatively rather than just comparatively. If there is a method of calibration of the data from the camera with the true radioactivity concentration, then quantitative measurements of radioligand uptake and concentration can be made. This is usually achieved through phantom measurement, where a radioactive source of known spatial radioactivity concentration and distribution is placed into the scanner, and the reconstructed data then used to calculate a calibration factor for subsequent scans where the spatial distribution is not known.

The methods here are split into the three data types; spatial, temporal and spatio-temporal. A summary of some of the statistical methods that can be used in PET has been previously published (McColl et al., 1994) including both spatial and temporal methods.

3.1.1 Spatial Modelling

Spatial quantification is important to understand the distribution of the radioligand through out the brain. However, spatial quantification is most usually a component of a spatio-temporal analysis, where a spatial model is implemented in the analysis prior to or post the application of a temporal model. However, any reconstruction of the data, could be seen as a spatial quantification in that, every voxel represents a spatial measurement.

As such, most quantitative modelling in PET has concentrated on temporal quantification. There are, however, a few methods which are worth mentioning here, as they can be used either on their own to look at spatial distribution, or alternatively be used in a spatio-temporal analysis.

ROI Analysis

Region of Interest (ROI) analysis is where the spatial data is assumed to come from anatomically specific locations. The data is usually sampled onto a grid of points, regularly spaced, but often anatomical information is known, which can improve the signal to noise ratio of the data. Data can be classified as belonging to a region of multiple voxel size, and each voxel can be seen as a realisation of the concentration of the region as a whole.

ROIs can be defined in a number of ways. The easiest, but probably least quantitatively accurate method, is the definition of the ROI simply based on the distribution of the tracer. This is done by defining a region directly onto the PET data set. More complex definitions can come from additional information provided by anatomical MRIs, or from anatomically informed basis functions (Kiebel et al., 2000). However, there are problems associated with these methods, most notably spatial normalisation and co-registration of the differing imaging modalities.

Image Normalisation and Co-Registration

Image normalisation and co-registration is crucial to analysis of images at anything other than the voxel level. In order to gain accurate interpretation of results, it is important that the anatomically defined structures be well localised even if it is only in an analysis where the spatial definitions are not made a-priori. Current methods are of increasing accuracy in both normalisation within an image modality and co-registration to another modality. Non-linear normalisation techniques (Ashburner and Friston, 1999) are now used which make use of low spatial frequency basis functions to model the differences between

images. Mutual Information (MI) techniques (Studholme et al., 1997) allow accurate co-registration between images of different modalities such as PET and MRI, allowing accurately defined regions on the MRI to be associated with regions on the PET image. Whilst these routines are discussed here in terms of PET, they are equally applicable to fMRI.

Partial Volume Correction

Partial volume correction is a method for correcting the data based on the spatial distribution of the radioligand and the point spread function (PSF) of the data. The PSF has the effect of blurring the data, and as such a method to acquire true quantitative data must be used.

$$\text{PSF} \otimes \text{True} = \text{Data} \tag{3.1}$$

where $\otimes$ represents the convolution operator. The true inhomogeneous spatial distribution of the radioligand leads to the under or over estimation as a result of the blurring. The methods and the development of new techniques to incorporate statistical information are considered in much greater detail in chapter 4.

3.1.2 Temporal Modelling

The majority of analysis methods developed for PET are intrinsically concerned with the temporal modelling of PET data. Temporal models are needed to allow the data to be expressed in terms of different parameters which are assumed to be associated with biological or pharmacological processes. These methods can range from simple difference methods based on frame by frame data, to complex modelling using both the data and model framework to define the final model structure. Particularly in metabolism and neuroreceptor ligand studies, the tracer uptake is non-linear (where here we consider any model with linear parameters as linear) in time, and as such different modelling techniques need to be used to estimate parameters from the data.

There are many techniques for the analysis of PET data and they can essentially be specified in terms continuum of methods from data driven methods to model driven methods (Figure 3.1). Data driven techniques, make few or no assumptions about the form of the model but simply use the data. However, this tends to result in classification of regions that have similar kinetic properties as opposed to generating parameters of biological interest. Model driven techniques make assumptions about the underlying models that

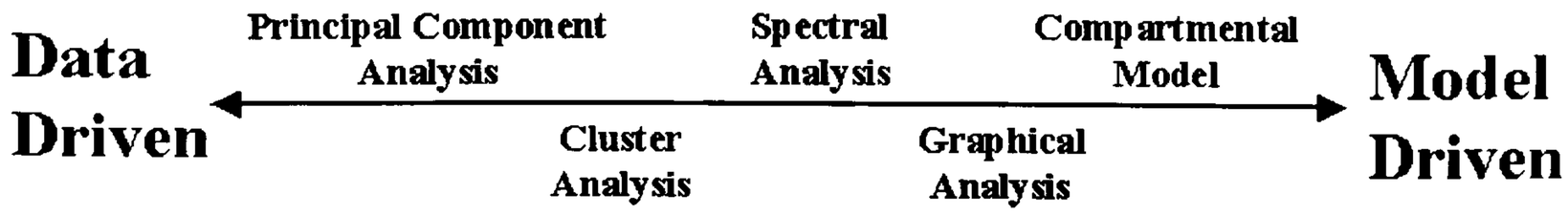


Figure 3.1: Continuum of Analysis for PET

describe the data. This leads to a description of the data in terms of a set of parameters. Techniques such as PET Spectral Analysis can be classified as somewhere between the model driven and data driven as they include some model assumptions but use the data to inform the actual model structure.

Tracer Kinetic Modelling

Tracer kinetic modelling is the use of models to describe the time course of the tracer. This is needed whenever the time course of the tracer is assumed to be changing over the period of the scan, and one frame can be related to another through a model. In blood flow studies the frames are assumed to be independent and each frame represents a different experiment. However, in metabolism and neuroreceptor ligand studies the kinetics of the tracer are much slower and the entire scan is essentially one experiment, with different measurements taken over the course of that experiment. The model can either be found from the data itself as in data driven analysis, or a model assumed and parameters fitted for the assumed model.

Tracer Kinetic analysis, especially model driven techniques, requires the fundamental knowledge of whether the radioligand binds reversibly or irreversibly to the binding site. This affects not only the analysis but the appropriate parameters that can be estimated. As will be seen, the differing techniques are often classified based on the assumptions of reversibility. Also if techniques that require blood-sampling are used then a separate calibrated measurement of the arterial blood concentration is also needed.

Principal Component Analysis

Principal component analysis is a statistical data driven technique which has been applied to the analysis of PET data sets (Friston et al., 1993). The variant for PET analysis was developed for blood flow studies but can be used for different types of analysis of parametric values. The present usage of these techniques includes multivariate analysis of the eigenimages, where eigenimages are spatial components that represent spatial modes

of the image space (Friston et al., 1996). This reduces the dimension of the problem to one where there are less components to analyse than there are scans, and hence multivariate techniques can be used.

Cluster Analysis

Cluster analysis is a method of functional segmentation of data sets and can be used with either PET or fMRI data (Gunn et al., 2001a). The data is segmented into a predefined number of clusters, such that the variance of the clusters is minimised. A volume is generated which associates each voxel to a cluster through a p-value. The highest p-value is then selected in the segmentation. The data must be normalised so that the distribution is based only on the shape as opposed to the magnitude of the curves.

Graphical Analysis

A type of analysis for PET data sets was developed by Patlak in order to find a linear relation between the data and the parameter of interest in irreversible uptake studies (Patlak et al., 1983).

$$\frac{C_T(t)_{(t>t*)}}{C_P(t)} = K_i \frac{\int_0^t C_P(t)d\tau}{C_P(t)} + V_0 + V_P \tag{3.2}$$

where C_T is the tissue concentration, C_P the concentration in plasma, V_0 the volume of distribution, V_P the volume of plasma in tissue, and K_i the irreversible uptake constant to be estimated. This relationship becomes linear after a sufficient time $t*$. In practice $t*$ is determined by assessment of when the line becomes linear. The analysis is independent of the number of reversible compartments in the system. The Patlak plot was intimately linked with the development of deoxyglucose tracer techniques.

The analysis has been adapted to reversible systems (Logan et al., 1990), but this analysis has problems with noise levels entering the solution in a non-linear fashion, and differing levels affecting the solution (Slifstein and Laruelle, 2000).

Spectral Analysis

PET Spectral Analysis (Cunningham and Jones, 1993) is a technique that is both data driven and model driven. It is model driven in that it assumes that there is a compartmen-

tal structure to the data, and hence the data can be modelled by a sum of exponentials,

$$C_T(t) = \sum_{i=1}^{n} \alpha_i e^{-\beta_i t} \otimes C_P(t) \tag{3.3}$$

$$\text{s.t. } \alpha_i \geq 0 \tag{3.4}$$

where the tissue time-activity curve $C_T(t)$ is modeled as a convolution ($\otimes$) of the measured plasma/blood input function $C_P(t)$ with a sum of n exponential terms, the β_i's are predefined as a spectrum of logarithmically spaced values between very rapid kinetics and the slowest possible kinetics which corresponds to irreversible trapping of the tracer, and α_i's are to be estimated. However the technique is data driven in that the number of exponentials, and hence the number of compartments assumed to describe the data, is not fixed, and is estimated from the data, by estimating the α_i. In this way, different time courses in the data, such as different ROIs or different voxels can be modelled by different numbers of exponential components. Spectral Analysis will be described in more detail in chapter 6

A-Priori Compartmental Modelling

A-priori compartmental modelling consists of selecting the model that best describes the data, and fitting the parameters of that model to the data set. This allows easy interpretability of the parameters that are estimated, as they relate directly to features in the model. However it is the least flexible of the approaches as the model is fixed, and only the parameters differ from time course to time course. This is often unimportant as the advantages of direct estimability and interpretability outweigh the small possibility that the model changes within the data set. The models themselves are a simplification of the underlying biological models, but describe the major dynamic processes involved.

These structures define the number of compartments that are assumed to be present within the data. Almost all compartmental systems used in PET are linear compartmental systems, where the parameters are assumed to be fixed rate constants in first order differential equations connecting the compartments. For example, the equations of a single tissue compartmental model are defined

$$\frac{dC_T(t)}{dt} = K_1 C_P - k_2 C_T \tag{3.5}$$

where K_1, k_2 are the rate constants of transfer to and from the compartment.

There are many forms of compartmental system, both reversible and irreversible, and these can all be described in terms of linear system theory (see chapter 5). There are

also many ways of fitting the data to these models. The principal methods concerning compartmental models will be discussed in chapter 5.

3.1.3 Spatio-Temporal Modelling

Spatio-temporal quantification is now a common method of analysis in PET. These methods are often just a combination of both the spatial and temporal methods described above. Either an ROI is defined and then a temporal time course is extracted for the ROI and analysed, or a temporal model is fitted to each data point and then an ROI used to average the parameters over the data points.

Although these two analyses seem as if they would be identical, this is not the case unless the temporal model is linear. This is because the sum of non-linear models does not necessarily yield a sum of the individual parameters. Often, however, the non-linearities are small over the parameter ranges, and this means that the two analyses are often almost identical. The equivalent analyses can also be done with partial volume correction, which could be seen as an extended ROI analysis.

It could indeed be argued that the Principle Component Analysis and Cluster Analysis discussed in temporal modelling are in fact spatio-temporal modelling. However the spatial component in these analyses are purely based on the temporal shape of these components, and as such do not really include an a-priori spatial model.

Wavelet Modelling

One method of spatio-temporal modelling is through the use of wavelets. Wavelets are a linear transform of the data into a functional space that better represents the data, in terms of the number of coefficients needed to represent the data in that space. There has been much work done in the implementation of wavelet methods in PET, both in spatial modelling and spatio-temporal modelling. Spatio-temporal modelling consists of transforming each spatial frame into the wavelet domain and then fitting a linear model to the data, and then transforming the fitted components of the linear model back into image space. Depending on the thresholding used in wavelet space, it is possible to make the transformation optimal in terms of different criteria; noise removal, mean squared error, minimax estimation. Wavelet techniques are discussed in chapter 7.

3.2 Magnetic Resonance Imaging

There are different types of analysis for MRI depending on the type of scanning protocol used. MRI has two very different uses, one for functional imaging and the other for structural. Whilst these two types of imaging are similar, there is a trade off between resolution in space and time.

3.2.1 Spatial Modelling

Spatial modelling is usually associated with structural MRI. A very high resolution ($\sim$ 1mm) image is produced over a long time interval compared with functional images.

Anatomical Localisation

One major usage of structural images, is anatomical localisation. As the image is of high resolution, it is possible to accurately define different regions of the brain. These are produced mostly by hand, although automatic techniques are in development. The regions defined can then be used in subsequent analysis for functional imaging studies, both PET and fMRI. For example, structural images can be used to define ROIs for PET ROI analysis. The ROIs are then transformed into the PET image space. This can allow, depending on the accuracy of the transformation, excellent definition of ROIs, where definition would be difficult using the PET alone. Anatomical MRIs are especially important when there is perceived to be structural abnormality in the brain, as quantification and localisation of this can dramatically alter assumed quantification in other modality measurement, e.g. when atrophy is present.

Tissue Classification

Tissue classification is the process of classifying brain tissue into a number of subtypes, independent of the assumed region of the brain. These subtypes are grey matter, white matter, and cerebro-spinal fluid, and these have different intensity distributions in MRI images. This can allow automatic classification of these subtypes based on the intensity (Lemieux et al., 1999). These measurements can be used in a variety of ways. Firstly global quantities of these tissue types can be evaluated across populations to determine changes with respect to covariates such as age. Also the probabilistic maps of tissue types can be analysed voxel by voxel to determine changes across subjects (Ashburner and Friston, 2000). This is intrinsically more difficult and is still the subject of debate as

to its application in practice (Bookstein, 2001). Finally the subtypes can be included in ROI definition, in so much as ROIs are defined not only by region, but also by subtype, to produce classified regions of interest. This is important as it is often expected that classified tissue behaves differently within regions.

3.2.2 Temporal Modelling

Temporal modelling for MRI is specifically designed for fMRI where temporal frames are taken every few seconds. fMRI has a much lower spatial resolution than MRI, but has the advantage that frames can be rapidly collected. As a point of interest, the slices in fMRI are collected in different ways depending on the protocol, and as such this needs to be taken into account in the analysis, as the onset of any stimulus will have a different delay to each of the slices.

Temporal methods are generally split into different types of analysis. The first is the characterisation of the Hemodynamic Response Function (HRF), where the signal response from a impulse is determined. The second type of analysis is the determination of differences or effects related to the design of the experiment, e.g. Activation / Baseline Protocol where a difference between activation and baseline response is tested, or where covariates of interest are tested to see if their inclusion in the model is of benefit. The third type of analysis is a more signal processing type of analysis, where methods are used to try to denoise the temporal signal, before other methods of analysis are used for either HRF or effect estimation.

Hemodynamic Response Function and BOLD Effect

There is now significant interest in modelling the underlying hemodynamic response function (HRF) of fMRI data. This is the impulse response function of the blood oxygen level dependent (BOLD) contrast mechanism (Buxton and Frank, 1997) which temporally smoothes the response to the stimulus as measured with fMRI. This is equivalent to the input function in PET. There are several models available for the HRF from very complex physiologically accurate models, such as the balloon model (Buxton et al., 1998), or mathematically descriptive models, which balance interpretability with the need for simplicity to enable parameter estimation (Glover, 1999). These models are often based on gamma functions which can model the two peaks which occur in the data, as well as the undershoot of the data (Friston et al., 1998).

Time Series Analysis

Time series approaches are popular for analyzing fMRI data. This is because fMRI has correlated measurement errors and as such these need to be calculated in order to efficiently estimate the parameters. One such method of analysis is that of non-linear fourier time series (Lange and Zeger, 1997) where the model of the signal Y at time t and location u is given by

$$Y(t,u) = X(t,\theta_u)\beta_u + \epsilon(t,u) \tag{3.6}$$

$$X(t,\theta_u) = \sum_{0\leq s,t-s\leq T-1} \lambda(s,\theta_u)x(t-s) \tag{3.7}$$

and is fitted using a fourier transform of the data, where $X(t,\theta_u)$ is the convolution of the stimulus with unknown hemodynamic response functions $\lambda(t,\theta_u)$ which vary spatially. This is done for two reasons. Firstly the errors which have temporal autocorrelation in the time domain, are independent in the fourier domain and secondly, the data can then be analysed in the appropriate frequency domain of the stimulus signal. The HRF is characterised by a two parameter gamma function.

Linear Models

Linear models are very popular in neuroimaging due to their simplicity of both specification and analysis. They are also interpretable with respect to the parameters in the model. Several models have been suggested and used, but they all tend to be refinements on a theme. Currently a robust and flexible model used for the analysis of fMRI (Worsley et al., 2002) is given by

$$Y(t) = (\mathrm{HRF}(t) \otimes X)\beta + Z\gamma + \epsilon \tag{3.8}$$

where X defines the stimulus matrix, Z the variables not associated with the stimulus, such as drift, and ϵ the error model which in this case is AR(p).

The HRF is specified by a double gamma function (Glover, 1999) which can adapt to some of the features seen in measured HRFs. The design matrix is convolved with this function and the parameters associated with the stimulus estimated, having prewhitened the data to account for the autocorrelations. This model is used in chapter 7 for the analysis of wavelet coefficients and discussed in more detail there.

Bayesian Methods

There is an increasing use of bayesian methods in neuroimaging, and fMRI is no exception. A non-linear bayesian time course model (Genovese, 2000) has been suggested for analysis where prior information from existing sources is incorporated into the over-parameterised model. The model used has four distinct components

$$Y(t) = \mu + d(t) + a(t; \mu, \gamma, \theta) + \sigma\epsilon(t) \tag{3.9}$$

where μ determines the baseline signal, $d(t)$ represents the drift of the signal, a the activation represented by the model parameters μ, γ, θ and $\epsilon(t)$ the noise function. The model parameters are estimated using a mixture of Metropolis-Hastings and Gibbs algorithms.

Independent Component Analysis

There has been work on using independent component analysis (ICA) to analyse fMRI data (McKeown et al., 1998). This work has its origins in principle component analysis, and can be useful in exploratory data analysis when the activation time course is not explicitly known in advance (McKeown et al., 1998). ICA splits the data into independent spatial components with the number equal to the number of temporal points. Each spatial location is assumed to be a linear sum of spatially independent components. If a task or time course is assumed the components can then be correlated with the task function. These methods have been shown through simulated and measured data to reveal spatial components in the data which relate well with the task, and perform better than corresponding PCA analysis (McKeown et al., 1998).

3.2.3 Spatio-Temporal Modelling

Spatio-temporal modelling in fMRI concerns the spatial localisation of temporal signal, or temporal connectivity between different regions. These connections can be seen at a different temporal resolution than with PET, as the time frames between data collection are much shorter, of the order of a few seconds.

Functional Connectivity

Functional connectivity or integration (Buechel and Friston, 1997) is used in neuroimaging to describe a variety of similar phenomena. These all follow the theme of describing connections from one region to another (Friston et al., 1993), but differ in the definition of

the temporal order. Some authors ignore temporal order, whilst others attempt to assign direction to the spatio-temporal model, such that the regions are not only connected but connect in a certain order. These orders can be based on neuronal connections and used in specifying prior functions, or derived purely from the data itself. This truly requires using temporal lagged models where data from one region at a previous time is the input for another region. However models are complex and the data difficult to model. Non-temporally specified models where regions are only connected, range from the simple use of one region's time course as a linear predictor of another's, to complex models based on the correlation functions of one region to another (Friston et al., 1993). Path analysis and structural equation modelling are also used (McIntosh, 1998) but the validity of the models can be called into question as the models depend heavily on the assumed construction.

Anatomically Informed Basis Functions

Anatomically informed basis function analysis (Kiebel et al., 2000) is a method of specifying prior anatomically informed information into the model, to allow spatio-temporal analysis. The method uses spatially defined basis functions, defined on the cortical surface, such that each basis function models a small part of the cortical surface. This assumes that the activation or response occurs on the cortical surface, as opposed to being localised below the surface. The basis functions are fitted to the spatial data set, using a regularised least squares model to ensure fitting when the models are close to being ill-posed. Temporal models (often linear models) are then used to analyse the subsequent spatial parameters generated from the fit. Anatomically informed basis functions were shown to improve the performance of signal localisation onto the cortical surface compared with SPM (Kiebel et al., 2000).

3.3 Statistical Estimation and Inference

This thesis is primarily about statistical estimation and inference. In some fields such as tracer kinetic modelling, the emphasis is on signal estimation as opposed to inference or error estimation. In other areas, such as activation studies, particularly with fMRI, the emphasis is on inference, where the most important consideration is whether there is a difference between two states, not necessarily the magnitude of that difference. These two ideas are fundamentally linked and it is often necessary to incorporate knowledge about one to properly calculate the other.

3.3.1 Mean Squared Error

There are several different ways of evaluating the estimation and inference criteria. The most often used in neuroimaging is to use a BLUE (Best Linear Unbiased Estimate) such that the estimate is unbiased. However, if signal estimation is required, then a minimiser of Mean Squared Error (MSE) may well be more appropriate. This allows a certain amount of bias into the estimate, if it results in an appropriate reduction in variance. The MSE links bias to variance as follows;

$$\begin{aligned} \text{MSE} &= \text{bias}^2 + \text{variance} && (3.10) \\ &= \left(E(\hat{\theta} - \theta)\right)^2 + \text{Var}(\theta) && (3.11) \end{aligned}$$

The MSE is then minimised to determine the best estimate in terms of MSE.

Whilst many of the algorithms developed in the thesis are based on achieving unbiased estimates, MSE is an important concept, especially in areas such as spatio-temporal modelling where signal distributions are as important as unbiased estimates.

3.3.2 Statistical Parametric Mapping (SPM)

Statistical Parametric Mapping (SPM) (Ashburner et al., 1999) is a software package developed for the statistical analysis of neuroimaging data. However, it has become far more than just a statistical software package, and is now a complete analysis framework for neuroimaging, and techniques are often described in terms of SPM regardless of whether the software package itself is used.

SPM contains two analysis steps; Image Manipulation and Statistical Analysis. The image manipulation techniques (Ashburner and Friston, 1999) consist of spatial normalisation, co-registration and segmentation algorithms. These allow the data to be put into a state where the subsequent statistical analysis can be performed. The statistical analysis is based on the linear model, in many different forms, and it is this that is of interest here.

The linear model can be described in terms of the matrix equation

$$y = X\beta + \epsilon \qquad (3.12)$$

where y is the data, X a matrix which describes the model, β the parameters associated with the model, and ϵ the noise in the data usually taken to be iid $N(0, \sigma^2)$, although more complicated noise models have also been used, such as temporally autocorrelated noise in fMRI time series. This can also be described in terms of many other statistical analysis.

which are all subtypes of the linear model, including regression, analysis of variance, and t-tests. SPM is based on the linear model, and much of the analysis is described in terms of the subtype, but it is all intrinsically the same general model. Much of the temporal analysis described earlier, as well as some of the spatial and spatio-temporal analysis, is included in the SPM software package. SPM does not specifically allow for tracer kinetic modelling, although it is often used to analyse the parameters generated. SPM was originally developed for PET blood flow studies, but is now most commonly used with fMRI studies.

The major advantages of SPM statistical analysis, and the main reason for its widespread use, is the ease of specification of models, and the framework of specification and analysis of the data. The incorporation of the image manipulation routines into the software allow easy preparation for analysis, and the most common models used in neuroimaging are easily specified. However, SPM is constrained in how this analysis is used by the models it presents, but new analysis techniques tend to become incorporated into the SPM framework either through inclusion in the core software, or by development of additional toolboxes which interface with the SPM routines, and use the SPM graphical user interface. One other criticism often levelled at SPM is that the threshold levels are often different between different studies with no apparent justification, but this criticism should be levelled at the users rather than the authors of the software, as the analysis can only be as good as the design by the users.

Multiple Comparison Correction

Multiple comparison correction is an important concept in neuroimaging, much more so than in other experimental sciences, due to the very large quantity of data that is collected in each experiment.

The most useful and sensitive method of multiple comparison correction is to use hypothesis driven methods. In this case, only the data that is of interest in tested, whilst other data is ignored. This limits the amount of data that is tested, and as such reduces the number of tests made. This is an important distinction, as often in neuroimaging, hypothesis driven methods are considered in the experimental design, and then the entire data set is analysed and corrected for multiple comparisons. This significantly reduces the ability to test the underlying hypotheses.

However, there are occasions where hypothesis testing is needed across entire data

sets, or subsets, and as such multiple comparisons correction is required. The simplest multiple comparisons correction procedure is the Bonferroni procedure, where significance level is scaled according to the number of tests. The Bonferroni procedure is based on the bonferroni inequality which although can be satisfied (equality) for independent events, can also result in very conservative tests for correlated events.

More complex methods of multiple comparisons correction are now routinely used in neuroimaging studies, especially those based on random field theory (Worsley et al., 1996b; Worsley et al., 1996a). These methods are incorporated into SPM. The underlying results to carry out multiple comparisons corrections using random field theory are given in Appendix A.4. These methods can be used due to the spatial correlation in the data, which means that the tests are not independent. However, the multiple comparison formulae derived from random field theory are approximations, and as such for small spatial correlations, the thresholds can be greater than the thresholds derived from Bonferroni correction, and as such a mixture of both methods is recommended.

3.3.3 Non Parametric Methods

There is increasing literature on the use of non parametric methods in neuroimaging. This is mainly due to the increasing computing power available for analysis of data, and as such computationally intensive techniques are more readily usable. However, the size of data sets often increases at a similar rate to computing power, and as such the computational burden becomes even greater.

Non parametric methods are valued due to the reduction in the number of assumptions that are required about the data. However, this reduction in assumptions does come at the price of a loss of sensitivity over parametric methods, where the assumptions are correct. However it was found (Nichols and Holmes, 2002) that whilst this is generally the case, in functional neuroimaging this is not necessarily true and non parametric methods can perform as well as bonferroni or random field correction methods, even with a small number of images. The thesis is, however, primarily concerned with parametric methods, due to the assumptions allowing possibly more sensitive analyses and the reduction in the computation burden, as most of the techniques are moderately computationally intensive in themselves, and non parametric versions would be computationally intractible in real time. However, certain non parametric methods are now used in neuroimaging and have been formulated in such a way that they can be used even with moderately large data

sets.

Statistical Non Parametric Mapping (SnPM)

Statistical non parametric mapping (Nichols and Holmes, 2002) is a toolbox for SPM. These methods are based on the permutation test where the scans are randomized and then analysed (such as looking at mean differences between conditions) and then the probability that the true order lies within a certain proportion of the empirically determined distribution calculated. These methods can be used to look at the multiple comparisons problem, and even approximate t-statistic images can be generated. SnPM also presents analysis using locally pooled estimates of variance to increase the power of the analysis, but whilst these can be validly used in activation studies, for other types of study such as neuroreceptor ligand studies the assumptions that these methods are based on, may not be valid (see chapter 8).

Bootstrap Methods

The bootstrap is another form of non parametric method. This involves using the data as the best estimate of its own distribution (Efron and Tibshirani, 1993). These ideas have been implemented in PET (Turkheimer et al., 1998) for intractible analysis problems. The algorithm for the residual bootstrap is given in Appendix A.2, and is used in chapter 6.

Chapter 4

Partial Volume Correction

This chapter is concerned with theory and methodology for the correction of partial volume effects. This is a spatially defined problem which results from the intrinsic spatial resolution of the scanner. This can lead to under or over estimation of local signal depending on its spatial distribution.

Methods will be presented here which aim not only to correct the data, but to estimate the errors on these corrections. Previous methods have facilitated estimation of the signal, but have not taken into account the noise structure of the data, nor attempted to estimate the variance on the resulting correction. A mathematical framework is developed to accommodate both the signal and the noise and to facilitate the development of new partial volume correction (PVC) algorithms. The convergence of these rapid iterative algorithms for general noise structures is considered. The algorithms may be applied to either raw dynamic data, or parametric image settings.

In this chapter, the partial volume problem will concentrate on the estimation of signal and errors from PET radioligands. A similar application of theory and methodology could be used to look at the equivalent partial volume problem in other modalities, although the individual spatial distributions and errors on the signal would of course need to be considered.

4.1 Partial Volume

The partial volume problem in PET concerns two properties arising from the limited resolution of the tomograph. It is useful to separate these from both an explanatory and mathematical standpoint, although they are both present due to limited resolution. The

two properties can result in incorrect estimation of the true local tissue concentration of radioactivity:

- "Tissue Fraction Effect" referring to underlying sub-resolution heterogeneity, for example grey and white matter in brain tissue. In general, correction for this effect requires additional prior knowledge, for example from an adjunct MRI scan with intrinsically higher resolution enabling determination of the appropriate tissue fractions.

- "Point Spread Effect" or spillover between regions, again reflecting the limited resolution of the tomograph (Hoffman et al., 1979; Mazziotta et al., 1981; Leahy and Qi, 2000). Typically the PSF is well approximated by a 3-dimensional Gaussian distribution with FWHM of the order of a few millimetres. This effect can, in principle, be corrected from the PET data alone, assuming that the point spread function of the scanner has been characterised.

It is convenient to distinguish these effects, firstly because the resolution of the tissue fraction effect will require data in addition to the PET measurements, and secondly because it will be seen to have statistical consequences in our analysis.

Recovery of the true concentrations of radioactivity in otherwise homogeneous regions thus requires a combination of tissue classification techniques with corrections for spillover between adjacent regions. The consequences of these effects on the signal have been investigated previously (Karp et al., 1991; Rousset et al., 1993; Iida et al., 2000), and a variety of correction methods, of differing complexities, have been proposed and applied to attempt accurate recovery of the signal in situations where regions are either defined by anatomy, by tissue type, or both (Meltzer et al., 1990; Muller-Gartner et al., 1992; Labbé et al., 1996; Labbé et al., 1998; Rousset et al., 1998). In PET the correction is usually applied on a regional level to the reconstructed images and includes regional homogeneity assumptions, which makes the problem more tractable than at the voxel level. Such corrections can have significant impact on the quantitative analysis of PET studies (Labbé et al., 1996; Meltzer et al., 2000; Law et al., 2000), particularly when it is necessary to take into account the effects of pathological or structural changes. Upwards of 300% increases in estimates of cerebral metabolism of $[^{18}F]$DOPA after PVC have been reported (Rousset et al., 2000). PVC has also being explored as a tool for recovery of the input function from PET images (Asselin et al., 2001). Indeed, in any study where true quantitative parameter estimates are required, the implementation of PVC is essential.

There are however, differences in the published methods, particularly as regards the implicit assumptions that are made about the underlying noise models. It will be seen in the present work that the assumed noise model has a direct impact on the appropriate algorithm to use for PVC.

The theoretical framework introduced here for the general PVC problem presents new and improved algorithms for the application of PVC techniques to static and dynamic PET images. Both the tissue fraction effect and the point spread effect are accommodated within this analysis. Previous methods are discussed within this theoretical framework. In addition, methods for error estimation are presented and regional inhomogeneity testing is investigated. The general theory for estimation of regional radioactivity concentrations, associated error estimation and inhomogeneity tests are presented in a weighted least squares framework. Regional inhomogeneity testing allows for the statistical assessment of the method's assumption that all regions are homogeneous in concentration.

4.2 Spatially Correlated Noise

Partial volume correction in PET will be considered with reference to both the distribution of the signal and the underlying noise model. The formulation of algorithms for the solution of the PVC problem is dependent on both of these factors. Noise needs to be considered in terms of both its distribution and its structure. Several noise distributions have been proposed in the past for simulation of the problem; Poisson, Gaussian and Poisson + Gaussian (Slifstein et al., 2001). This is extended here, not only to consider the noise distributions but also to investigate inclusion of the correlation structure of the noise and algorithms formulated for these differing structures.

4.2.1 Noise Models

The measurement of PET data is an inherently noisy process. Radioactive decay is itself a random process with a Poisson distribution, and other distributions of noise enter the system at many stages of data collection and reconstruction. In the present paper, two structures are considered. First, if the noise is inherent in the signal, before any reconstruction has taken place, then it is considered that this noise will be subject to blurring due to the PSF and will result in spatially correlated noise in the reconstructed image. Second, noise occurring across the reconstructed image on a random basis will be modelled with an additive term with no spatial correlation.

- **Uncorrelated Noise Models.** This noise model assumes that there is additive Gaussian noise across the reconstructed image and corresponds to high spatial frequency noise. Previous methods (Labbé et al., 1996; Labbé et al., 1998; Rousset et al., 1998) are implicitly based on this model although slightly different weights are applied to obtain the solution (see 4.3.1).

- **Correlated Noise Models.** There will be a component in the noise that is correlated by the point spread function. This could arise from the signal itself, or other noisy processes that become blurred by the PSF. An uncorrelated component will also be included in the model to allow for any high spatial frequency noise, which would cause an ill-conditioned solution if inappropriately accounted for. The limit of this model is a purely PSF correlated noise model, but as has been previously seen (Leahy and Qi, 2000), this does not adequately describe the true noise in the data.

For the algorithms, whether the noise is homogeneous across the image, or whether heterogeneous is of little interest. There is evidence that the variance is homogeneous across image (Pajevic et al., 1998). Previous work has detailed methods for the approximation of ROI and voxelwise variance (Carson et al., 1993). In fact this specifies the correlation function between voxels and as such can be used as the correlation function in the algorithms themselves. This specification needs to be made prior to the analysis, but the analysis itself will proceed in the same way. For the data presented later, the noise models will assume either homogeneous or hetergeneous variances across the image but include a homogeneous uncorrelated variance component.

4.3 Signal and Variance Estimation

The problem is first formulated in 1 dimension for simplicity. It will be seen that given a separable point spread function the problem generalises simply to 3 dimensions. The correlation function has been assumed, for simplicity, to be accurately characterised by the PSF, but any separable correlation function can be easily accommodated in this framework. Let P be an $n \times n$ matrix, where n is the number of voxels, whose operation on a vector corresponds to the blurring introduced by the PSF. For a symmetric spatially invariant PSF this is a Toeplitz matrix, although other more general PSF distributions can be accommodated. Let R be an $n \times r$ matrix defining r anatomical regions ($R \in [0, 1]$).

Let T be an $n \times t$ matrix denoting the t different tissue classifications, ($T \in [0, 1]$). Let b be an $n \times 1$ vector containing the measured tracer concentration. Consequently x is an $r\,t \times 1$ vector denoting the true radioactivity concentrations in the different classified regions. As constructed, P accounts for the "Point Spread Effect", $R \odot T$ account for the "Tissue Fraction Effect", where $\odot$ is the Khatri-Rao row product (see Appendix A.1). The tracer concentration is assumed to be homogeneous within each classified region. A simple example is presented in Figure 4.1a which illustrates how the measured tracer concentrations may be an under- or over-estimation of the true concentration.

The partial volume problem can then be constructed as a matrix equation, (Figure 4.1b),

$$P(R \odot T)x = b, \tag{4.1}$$

and the introduction of noise components gives,

$$P((R \odot T)x + \eta_c) = b + \eta_u, \tag{4.2}$$

where η_c and η_u are correlated (after application of the PSF) and uncorrelated noise vectors respectively (see 4.2.1). This equation can be rearranged in terms of the recovered signal and noise components[1],

$$(R \odot T)x = P^{-1}b + (P^{-1}\eta_u + \eta_c), \tag{4.3}$$

and is a linear equation of the form $Ax = b + \epsilon$.

The weighted linear least squares solution, x, is determined by minimising the objective function,

$$\min_x \quad (W^{\frac{1}{2}}((R \odot T)x - P^{-1}b))^T(W^{\frac{1}{2}}((R \odot T)x - P^{-1}b)), \tag{4.4}$$

where the weighting matrix W is the inverse of the covariance matrix of the compound error $(P^{-1}\eta_u + \eta_c)$ and the solution is given by,

$$\hat{x} = ((R \odot T)^T W (R \odot T))^{-1}(R \odot T)^T W P^{-1} b. \tag{4.5}$$

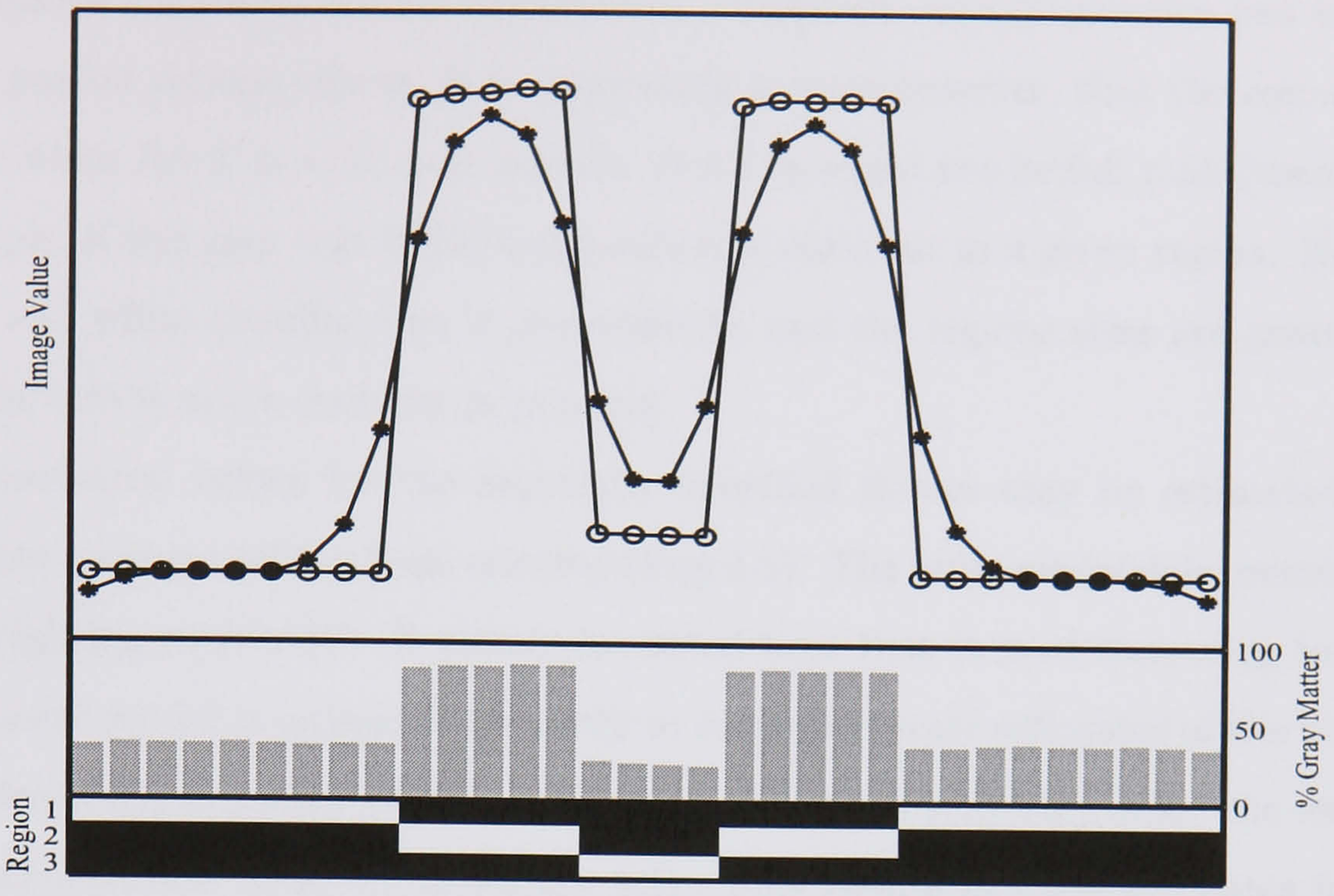
It follows that the variance on the estimates is given by,

$$var(\hat{x}) = \frac{((R \odot T)^T W (R \odot T))^{-1}((R \odot T)x - P^{-1}b)^T W((R \odot T)x - P^{-1}b)}{n - rt}, \tag{4.6}$$

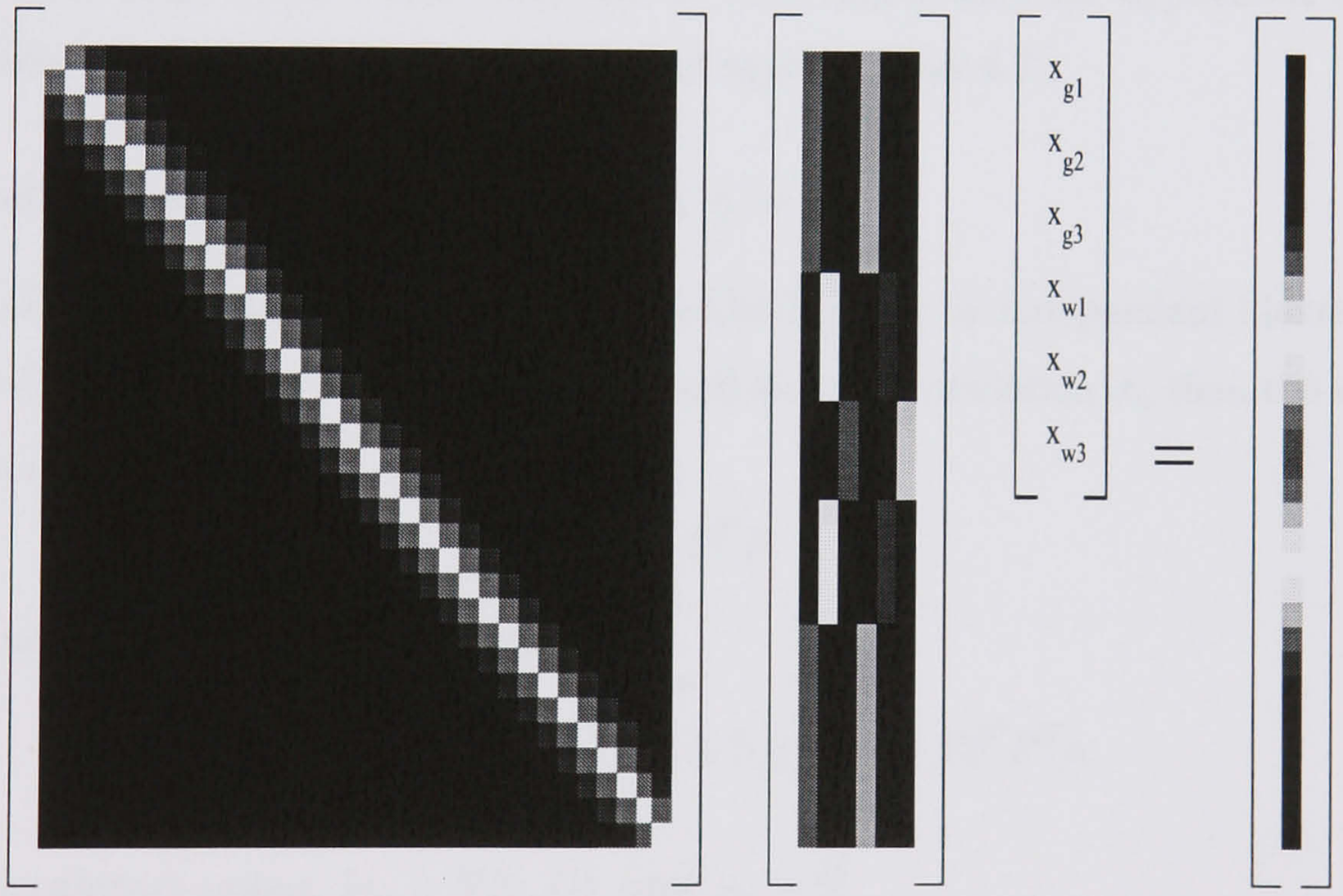
and the sum of squares accounted for by each ROI is given by,

$$SSQ_{ROI} = ((R \odot T)x - P^{-1}b)^T W^{\frac{1}{2}} \Lambda(R_{ROI}) W^{\frac{1}{2}}((R \odot T)x - P^{-1}b) \tag{4.7}$$

[1] η_u or η_c represent the noise processes and hence the signs are unimportant here



(a)



(b)

Figure 4.1: 1D PVC Example: (a) (top) Tissue Radioactivity with (*) and without (o) application of PSF, (middle) Tissue Classification (Grey and White only), (bottom) Region Definitions (b) Matrix construction of the recovery problem, where x_{gi} and x_{wi} are the recovered grey and white matter values respectively for region i.

where $\Lambda()$ is the diagonal matrix operator, and ROI is the index of the region to be tested.

The above equations are all theoretically consistent, and in practice can be used to evaluate partial volume effects. It is interesting to note however, that the equations only hold true when $R \odot T$ is a full rank matrix. $R \odot T$ is might not be full rank (theoretically), for example, if the grey and white composition is constant in a given region. However as the grey and white classification is probabilistic, and the regions sizes are greater than a few voxels, this is not a problem in practice.

The recovered values for the regionally classified tissues may be estimated once an appropriate noise model has been selected (Eqn 4.5). The noise model determines the form of the weighting matrix W. It should be noted here that it is of increasing importance that the noise model is estimated correctly to ensure accurate estimates of the parameters above. Hence the accuracy of the weighting is of limited importance for the estimate of tracer concentration (Eqn 4.5 & Figure 4.2). This results in good estimates from both Labbé and Rousset's methods. However, it is more important for estimation of the error on this value (Eqn 4.6 & Figure 4.2) and of vital importance for hypothesis testing of homogeneity derived from the residual sum of squares (Eqn 4.7).

Uncorrelated noise: $[\eta_u \sim N(0, \sigma_u^2 I)$ **and** $\eta_c = 0]$

If the noise on the measured image is characterised purely by independent identically distributed Gaussian processes with zero mean and standard deviation σ_u then the weighting matrix is given by,

$$W = P^T P, \tag{4.8}$$

and the weighted least squares solution is,

$$\hat{x} = ((R \odot T)^T P^T P (R \odot T))^{-1} (R \odot T)^T P^T b. \tag{4.9}$$

Pure correlated noise: $[\eta_c \sim N(0, D)$ **and** $\eta_u = 0]$

If the noise post reconstruction has no uncorrelated component then

$$W = D^{-1} \tag{4.10}$$

where D is a diagonal matrix representing variances at each voxel (can be homogeneous or inhomogeneous).

The weighted least squares solution is,

$$\hat{x} = ((R \odot T)^T D^{-1} (R \odot T))^{-1} (R \odot T)^T D^{-1} P^{-1} b. \tag{4.11}$$

Correlated noise: $[\eta_c \sim N(0, D)$ **and** $\eta_u \sim N(0, \sigma_u^2 I)]$

If the noise on the image is characterised by both independent identically distributed Gaussian processes then the weighting matrix is given by,

$$W = (D + \sigma_u^2 P^{-1}(P^{-1})^T)^{-1}, \tag{4.12}$$

and the weighted least squares solution is,

$$\hat{x} = ((R \odot T)^T (D + \sigma_u^2 (P^{-1}P^{-1})^T)^{-1} (R \odot T))^{-1} \tag{4.13}$$
$$(R \odot T)^T (D + \sigma_u^2 P^{-1}(P^{-1})^T)^{-1} P^{-1} b.$$

If any part of the noise structure is signal dependent, then the recovered signal needs to be known. These equations assume that the value for this signal is known. As this will not be the case in heterogeneous signal-dependent noise such as poisson noise, the solution requires an iterative solution using updates of the estimates, known as Fisher Scoring (McCullagh and Nelder, 1989). This is easily incorporated into the algorithms described.

4.3.1 The Methods of Labbé and Rousset

The methods of both Labbé (Labbé et al., 1996) and Rousset (Rousset et al., 1998) and their solutions to the general partial volume correction problem,

$$P(R \odot T)x = b, \tag{4.14}$$

can be characterised by their implicit weighting matrices, W, in the weighted least squares framework (Eqn 4.4 & 4.5).

Rousset's Method

The solution given by Rousset is,

$$x = ((R \odot T)^T P (R \odot T))^{-1} (R \odot T)^T b, \tag{4.15}$$

which is equivalent to a weighted least squares solution in which,

$$W = P. \tag{4.16}$$

Labbé's Method

The solution given by Labbé is,

$$x = ((R \odot T)^T P^T P (R \odot T))^{-1} (R \odot T)^T P^T b \tag{4.17}$$

which is equivalent to a weighted least squares solution in which,

$$W = P^T P, \tag{4.18}$$

and can be interpreted as the ordinary least squares solution to the problem.

4.3.2 1-D Simulations

The one dimensional simulations presented here are primarily to demonstrate the problems that can occur if the wrong noise model is assumed when fitting the data, in terms of the estimation of the mean and variance. Although the noise model here is a proportional model, where the noise is proportional to the signal, the underlying problems will also be evident with other noise models.

Simulations were carried out using the example signal representation above. This was done in order that there would be regions where the signal was both over and under estimated. Noise was added which had both a homogeneous uncorrelated component, and a heterogeneous (proportional to the signal) correlated component. The data sets were then simulated with 25000 repetitions to build up accurate distributions from each of the estimators.

As can be seen in the figure (Figure 4.2) if the noise model is incorrect, the estimates of the variance of the signal estimate are not correct. The histograms represent the true distribution of the estimate of the value whilst the solid lines represent the estimated distribution. As can be seen, the variance of true distributions are either under or over estimated by the Rousset and Labbé algorithms, and different regions have different over / under estimation. This is due to the implicit assumptions of the model. The Labbé algorithm assumes uncorrelated noise, and as such the background as the largest region dominates this noise resulting in a good estimate of the background noise, but under-estimation in regions of higher noise. The Rousset algorithm has the assumption that the noise is inversely correlated from smoothing, and as such over-estimates the variance in regions with low noise and under-estimates the variance in regions with higher noise. However the estimates of the signal itself is unbiased for the differing estimators.

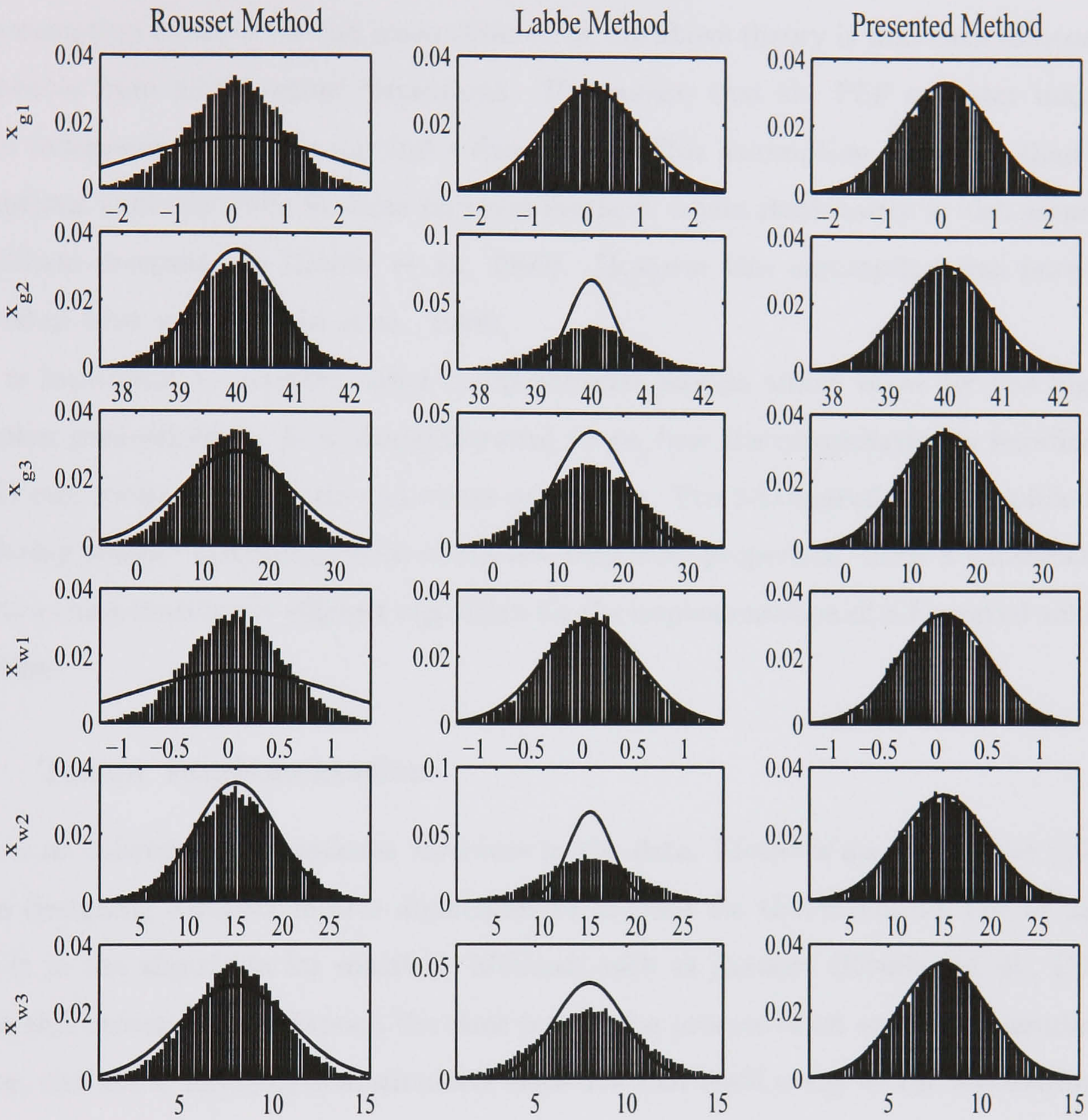


Figure 4.2: 1D PVC Example: Noise Distribution. Histogram: Estimated values, Solid Line: Expected Theoretical Parameter Distribution. X-axis: estimated parameter values, Y-axis: probability. This data is simulated using a heterogeneous correlated and homogeneous uncorrelated noise model. The presented method uses this noise structure, whilst the methods of Labbé and Rousset have implicit assumptions about the noise. This figure is intended as a graphical representation of the performance of the differing methods in differing noise situations.

4.4 Algorithms for 3-D Solution

The theory above has been presented in terms of the 1-Dimensional case. A consideration of the assumptions which allows the theory to be generalised to 3-Dimensions follows. The only assumption to allow the full generalisation of the above theory is that each dimension is separable from all the other dimensions. This means that the PSF operator may be applied independently in the x,y and z dimensions. This assumption is weaker than the assumptions that are made in some previous methods where stationarity is also assumed to facilitate computation (Labbé et al., 1996). However this assumption was partially removed in later work (Labbé et al., 1998).

It is important to consider other computational aspects which allow for the higher dimension generalisation. It is straightforward to see how the computation is handled in the 1-D case with simple matrix and vector operations. The 3-D equivalent is simplified by considering tensor[2] operations with restrictive separable properties. Such a construction leads to a computationally efficient algorithm for the implementation of 3-D partial volume correction.

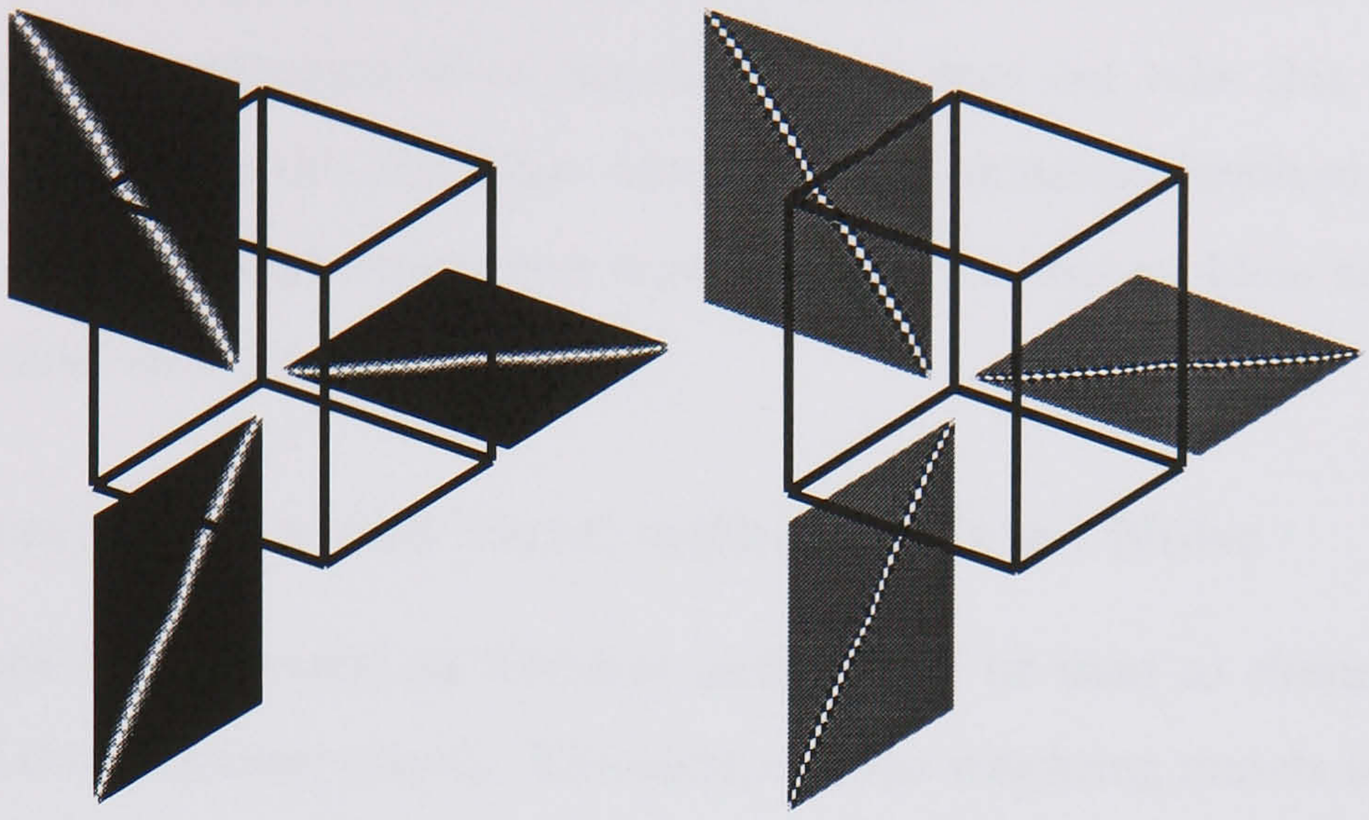
4.4.1 Tensor Implementation

There is an inherent 3-dimensional structure in the data. Methods such as Labbé (1996) , while designing complex matrix algorithms to account for this structure, fail to make use of it in the algorithm for solution. Methods such as Rousset (Rousset et al., 1998), did use this structure but through the time consuming process of an analytical simulator. Further, the use of an analytical simulator does not lend itself easily to the calculation of errors.

The algorithm proposed here will allow easy specification of a spatially variant PSF, with the assumption of separability in the 3 cartesian axes. This is the equivalent assumption to Labbé, but with the added advantage of allowing for a spatially variant PSF.

A tensor can be thought of as a multi-dimensional matrix. The PSF specification is then classed as a 6-D tensor taking ((x,y,z),(x',y'z')) co-ordinate structures so that any point is related to the space that the point is blurred to. The condition of separability allows the 6-D tensor to be written as a product of three 2-D tensors relating (x,x'), (y,y') and (z,z') (see Figure 4.3). Thus the tensor product becomes a series of matrix multiplications, which are fast and simple to compute. This process is also applicable

[2]Tensors are merely generalisations of vectors (1D) and matrices (2D) in higher dimensions



(a) Tensor PSF Operator (b) Tensor Recover Operator

Figure 4.3: Tensor Operators for Problem and Solution in Three Dimensions

to the weighting matrix for the purely uncorrelated and purely correlated cases. For the more complex correlated noise model other methods are required and developed below (see 4.4.2).

The algorithm applies the PSF to the native 3-D volume without requiring vectorisation of the image. All operations are thought of as multi-dimensional operations as opposed to the uni (vector) or bi (matrix) dimensional operations of other methods. Thus the solution may be written in tensor notation as,

$$x_{r_1} = (R_{r_1 z_1 y_1 x_1} W_{x_1 y_1 z_1 z_2 y_2 x_2} R_{x_2 y_2 z_2 r_2})^{-1} \ldots$$
$$R_{r_2 z_3 y_3 x_3} W_{x_3 y_3 z_3 z_2 y_4 x_4} P_{x_4 y_4 z_4 z_5 y_5 x_5} b_{x_5 y_5 z_5}, \tag{4.19}$$

using the summation notation convention. The inverse, in Eqn 4.19, is simply a 2D matrix inverse.

For the different noise models these equations lead to slightly different algorithms. In the purely uncorrelated and purely correlated (no uncorrelated component) cases this equation can be used to estimate both the signal ($\hat{x}$) and errors ($var(\hat{x})$) since P and W are separable. However, the correlated noise case requires an extra algorithm because although P is well specified in a separable tensor notation, W is not (even though W^{-1} can be specified in a separable tensor notation). This algorithm could be described in

terms of a constrained noise algorithm, where the uncorrelated component of the noise acts as a regularisation parameter. A very small component of uncorrelated noise causes large variance in the estimates of an algorithm that does not take this possibility into account. This is due to the condition number of the matrices involved. However the addition of the uncorrelated component term accounts for this problem and as such acts as a regularisation term for the algorithm.

4.4.2 Estimation of x and var(x) with Correlated Noise

For the correlated noise model an iterative method can be used to circumvent the non-separability of the weighting matrix. The inverse of the weighting matrix is separable and this lends itself to the iterative solution of $Z = WR$. Estimates of Z are updated via a suitable scheme until $W^{-1}Z = R$.

Iterative Method

A first-order stationary iterative scheme was chosen which converges in all cases and has a suitably bounded convergence parameter (see below). The algorithm for the correlated noise model is,

$$Z_{n+1} = (1 - \tau)Z_n + \tau \frac{1}{\sigma_u^2} P^T P(R - \Lambda(Rx)Z_n) \tag{4.20}$$

where τ is a relaxation parameter which is calculated at the beginning of the algorithm to ensure convergence.

The solution Z is then incorporated into the weighted least squares solution as,

$$\hat{x} = (Z^T R)^{-1} Z P^{-1} b, \tag{4.21}$$

and for the variance estimate as,

$$var(\hat{x}) = \frac{(Z^T R)^{-1} Z^* (Rx - P^{-1}b)}{N_{Vox} - N_{ROI}}, \tag{4.22}$$

where $Z^* = (Rx - P^{-1}b)^T W$ is solved using the same iterative procedure.

Proof of Convergence

Let $C = \sigma_u^2 P^{-1}(P^{-1})^T$ and $W = (D + \sigma_u^2 (P^{-1})^T P^{-1})^{-1}$ as above. Then the iterative scheme (Eqn 4.20) is given by,

$$Z_{n+1} = Z_n + \tau C^{-1}(R - W^{-1} Z_n) \tag{4.23}$$

If C^{-1} and W^{-1} are positive definite (which is elementary from their definitions) then the iterative scheme will converge for $0 \leq \tau \leq \frac{2}{\lambda_n}$ where λ_n is the maximal eigenvalue of $C^{-1}W^{-1}$ (Axelsson, 1994, Theorem 5.6).

Thus, to guarantee convergence, it remains to calculate an upper bound for the maximal eigenvalue of $C^{-1}W^{-1}$ which enables an appropriate selection of τ.

$$\begin{aligned} C^{-1}W^{-1} &= \frac{1}{\sigma_u^2} P^T P (D + \sigma_u^2 (P^{-1}P^{-1})^T) \\ &= \frac{1}{\sigma_u^2} P^T P D + I \end{aligned} \tag{4.24}$$

where I is the identity matrix. The eigenvalues of $C^{-1}W^{-1}$ are the eigenvalues of a product of a positive definite matrix $P^T P$ and a diagonal matrix plus the identity matrix. A corollary (Axelsson, 1994, Corollary 3.14) of the Courant-Fischer theorem (Axelsson, 1994, Lemma 3.13) gives an upper bound for the maximal eigenvalue in the case of a product of a positive definite matrix ($P^T P$) and a matrix with non-negative maximal eigenvalue (D). The addition of the identity matrix simply adds 1, giving,

$$\lambda_{max}(C^{-1}W^{-1}) \leq \frac{1}{\sigma_u^2} \; s_{max}(P)^2 \; \lambda_{max}(D) + 1 \tag{4.25}$$

where s_{max} is the maximum singular value and λ_{max} is the maximum eigenvalue. $\lambda_{max}(D)$ is the largest element of D and $s_{max}(P)$ is the product of the maximal singular values of each cartesian component of P.

A value for τ that guarantees convergence of the iterative scheme can then be chosen as

$$\tau = \frac{2\sigma_u^2}{s_{max}(P)^2 \; \lambda_{max}(D) + 1} \tag{4.26}$$

4.4.3 Application

The practical aspects of the application of the algorithms above need also to be considered. There are several differing types of data needed to allow the full implementation of these algorithms.

If differing tissue classifications are required, such as grey matter, white matter and cerebro-spinal fluid (CSF), then segmentation techniques using the MRI (Lemieux et al., 1999) are needed. These are based on using the differing intensities in the data corresponding to these differing tissue classifications (Lemieux et al., 1999). These represent the T variable in the equation.

The R variable is defined from regional definition. This is the definition of anatomical regions that are assumed to have homogeneous signal distribution within each classified

tissue type. There are two main types of definition; deterministic and probabilistic. Previous anatomical templates have tended to be single subject or averaged deterministic templates. Every voxel is associated with one and only one anatomical region. If this is the case, then this could be exploited later in homogeneity testing. The probabilistic templates have a probability associated with each voxel, which equates to the probability that a voxel belongs to a given region (often empirically zero). These are based on anatomical segmentation of a large number of data sets, and then the combination of results from these segmentations.

One problem with the use of these methods, is that the data does not tend to begin in the same spatial framework. The regional template is usually in some predefined space, whilst the segmented tissue classification, being in the subjects own space, is not necessarily the equivalent space to the subject's PET data. Thus spatial normalisation (Ashburner and Friston, 1999) and co-registration (Ashburner and Friston, 1997) between normalities is required. This is another potential source of error, which although not considered explicitly here, would result in extra variance in the output. However, co-registration can achieve sub-voxel accuracy (Studholme et al., 1997), and spatial normalisation is usually carried out using high resolution MRIs. When coregistered to the PET data, which itself has a much lower resolution, these should have small error associated with them.

The output from the partial volume will depend on the input data. If the initial data is in the form of dynamic images, then PVC will yield regionally corrected time activity curves, one for each defined tissue classified region. If the initial data is a static image, then a single corrected value for each tissue classified region is estimated.

4.5 Syringe Simulations / Measured

The Syringe Phantom data were simulated realisations of the measured data obtained from the ECAT ART scanner. The reported PSF characteristics (Bailey et al., 1997) for the ART scanner were used to specify the PSF as a Gaussian kernel, both in the construction of the data set and the subsequent fitting procedures of the algorithms. This allowed for perfect specification of the PSF. The syringe ROIs were generated as cylinders corresponding to the size and location of their counterparts in the physical phantom (Figure 4.4). Noise was added to the images to approximate the measured data. Homogeneous uncorrelated noise was introduced before applying the PSF and subsequently uncorrelated noise was added. The variance of the noise was based on the background noise in the ac-

tual measured images. The analysis was carried out using the presented algorithms, as well as Labbé and Rousset's algorithms, to recover the signal and the error estimates.

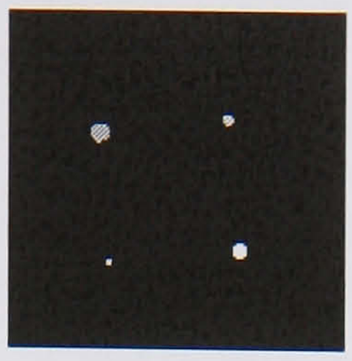


Figure 4.4: Definition of the 5 regions (including background) for the syringe data set represented by different grey levels (corresponding to R).

Four syringes of inner diameters 14.8+/-0.1mm, 11.9+/-0.1mm, 8.6+/-0.1mm and 4.7+/-0.1mm were filled with a C-11 solution (75 kBq/ml at the start of the first acquisition) and inserted into a 20-cm diameter 30-cm long cylinder filled with water. The phantom was scanned in an ECAT ART tomograph (CTI/Siemens, Knoxville, TN, USA) for 10s and 120s, four times, one half life (20 min) apart each time (Figure 4.5). The images were reconstructed using the reprojection algorithm (Kinahan and Rogers, 1989) with the ramp and Colscher filters set at Nyquist cut-off frequency. A calculated attenuation correction and a model-based scatter correction (Watson et al., 1996) were applied to the data during reconstruction. The reconstructed images consisted of 47 planes (of which only the centre seven were used in the analysis) having a transaxial spatial resolution of 6.7 mm (at 5 cm from the centre of the FOV where the syringes were located) and an axial spatial resolution of 6.8 mm (FWHM) (Bailey et al., 1997). The presented analysis was again used to calculate the recovery and errors and compared with the methods of Labbé and of Rousset.

The syringe simulations showed that good recovery of the true signal was achieved with all algorithms (Table 4.1). However, the estimates of the standard deviation in the Labbé and Rousset algorithms were too low, which would lead to the rejection of null hypotheses with the true mean in some cases. This did not occur with the presented algorithm.

The presented algorithm took approximately 10 mins per frame to run. This is dependent on the noise model, as can be seen in equation 4.26. The condition number of the matrices in the equations depends on the relative contributions of the noise. The Labbé and Rousset algorithms took approximately 10 secs per frame to run.

As can be seen (Table 4.2), the measured data sets were less well modelled by the noise characteristics, than the simulated data. This is not unexpected as the simulated data

	Time		14.8mm			11.9mm			8.6mm			4.7mm			Bgd		
Method	Start	Dur	NC	$\hat{x}$	$sd(\hat{x})$	NC	$\hat{x}$	$sd(\hat{x})$	NC	$\hat{x}$	$sd(\hat{x})$	NC	$\hat{x}$	$sd(\hat{x})$	NC	$\hat{x}$	$sd(\hat{x})$
Rousset	0	10	52.4	74.8	0.17	48.6	76.4	0.22	36.8	73.4	0.35	17.9	68.6	0.87	0.12	-0.023	0.007
Labbe	0	10	52.4	74.7	0.27	48.6	76.5	0.37	36.8	73.5	0.62	17.9	71.1	1.73	0.12	-0.023	0.011
Presented	0	10	52.4	74.8	0.77	48.6	76.3	0.98	36.8	73.1	1.47	17.9	69.7	3.48	0.12	-0.023	0.035
Rousset	10	120	52.7	75.1	0.09	48.0	75.4	0.12	37.9	75.5	0.20	19.5	74.5	0.49	0.15	0.010	0.004
Labbe	10	120	52.7	75.2	0.08	48.0	75.4	0.11	37.9	75.6	0.19	19.5	73.5	0.51	0.15	0.010	0.003
Presented	10	120	52.7	75.1	0.23	48.0	75.4	0.29	37.9	75.3	0.44	19.5	74.4	1.04	0.15	0.011	0.010
Rousset	1200	10	51.3	73.2	0.23	46.8	73.6	0.29	39.4	78.7	0.47	22.4	85.9	1.17	0.09	-0.052	0.009
Labbe	1200	10	51.3	73.1	0.39	46.8	73.5	0.53	39.4	79.9	0.89	22.4	83.9	2.47	0.09	-0.057	0.015
Presented	1200	10	51.3	73.2	1.11	46.8	73.6	1.40	39.4	78.3	2.10	22.4	86.1	4.98	0.09	-0.046	0.050
Rousset	1210	120	52.6	75.0	0.10	48.1	75.5	0.13	37.7	75.2	0.21	19.5	74.7	0.53	0.16	0.020	0.004
Labbe	1210	120	52.6	74.9	0.11	48.1	75.5	0.15	37.7	75.2	0.25	19.5	73.9	0.71	0.16	0.021	0.004
Presented	1210	120	52.6	75.1	0.32	48.1	75.5	0.40	37.7	75.2	0.60	19.5	74.7	1.42	0.16	0.020	0.014
Rousset	2400	10	53.0	75.5	0.31	49.1	77.1	0.40	40.5	80.7	0.64	20.3	77.6	1.60	0.23	0.085	0.013
Labbe	2400	10	53.0	75.5	0.55	49.1	77.2	0.74	40.5	80.6	1.25	20.3	75.0	3.47	0.23	0.084	0.021
Presented	2400	10	53.0	75.1	1.55	49.1	77.4	1.96	40.5	80.8	2.94	20.3	79.6	6.96	0.23	0.087	0.071
Rousset	2410	120	52.2	74.4	0.12	47.0	73.9	0.15	38.0	75.7	0.24	19.5	74.8	0.61	0.09	-0.052	0.005
Labbe	2410	120	52.2	74.3	0.16	47.0	73.8	0.21	38.0	75.5	0.36	19.5	76.2	0.99	0.09	-0.053	0.006
Presented	2410	120	52.2	74.5	0.44	47.0	74.1	0.56	38.0	75.8	0.84	19.5	75.3	2.00	0.09	-0.052	0.020
Rousset	3600	10	51.9	74.0	0.42	47.9	75.2	0.55	36.5	72.8	0.88	17.0	65.2	2.19	0.14	0.004	0.018
Labbe	3600	10	51.9	74.2	0.77	47.9	74.0	1.04	36.5	70.9	1.76	17.0	63.7	4.88	0.14	0.004	0.030
Presented	3600	10	51.9	74.0	2.18	47.9	75.8	2.76	36.5	73.7	4.14	17.0	65.4	9.82	0.14	0.007	0.099
Rousset	3610	120	52.7	75.2	0.14	47.4	74.5	0.19	38.0	75.8	0.30	18.9	72.4	0.75	0.16	0.020	0.006
Labbe	3610	120	52.7	75.4	0.22	47.4	74.5	0.29	38.0	75.5	0.50	18.9	73.8	1.38	0.16	0.020	0.008
Presented	3610	120	52.7	75.0	0.62	47.4	74.4	0.78	38.0	75.8	1.17	18.9	71.9	2.78	0.16	0.020	0.028

Table 4.1: Results from partial volume correction of simulated syringe data (Syringe diameters 14.8, 11.9, 8.6 and 4.7mm) from Rousset, Labbé and Presented method: value with no correction (NC) value after correction ($\hat{x}$) and estimated standard deviation of value ($sd(\hat{x})$).

	Time		14.8mm			11.9mm			8.6mm			4.7mm			Bgd		
Method	Start	Dur	NC	$\hat{x}$	$sd(\hat{x})$	NC	$\hat{x}$	$sd(\hat{x})$	NC	$\hat{x}$	$sd(\hat{x})$	NC	$\hat{x}$	$sd(\hat{x})$	NC	$\hat{x}$	$sd(\hat{x})$
Rousset	0	10	51.4	73.2	0.16	50.5	79.4	0.20	39.7	79.2	0.32	20.1	76.7	0.81	0.19	0.045	0.007
Labbe	0	10	51.4	74.0	0.28	50.5	80.0	0.37	39.7	80.3	0.63	20.1	83.7	1.73	0.19	0.040	0.011
Presented	0	10	51.4	72.7	0.80	50.5	78.2	1.01	39.7	78.5	1.52	20.1	75.1	3.59	0.19	0.049	0.036
Rousset	10	120	52.8	75.3	0.10	50.5	79.3	0.13	39.9	79.4	0.21	19.5	74.7	0.53	0.17	0.023	0.004
Labbe	10	120	52.8	75.7	0.09	50.5	79.8	0.12	39.9	81.0	0.21	19.5	77.6	0.59	0.17	0.019	0.004
Presented	10	120	52.8	74.8	0.24	50.5	78.7	0.30	39.9	78.3	0.46	19.5	73.4	1.08	0.17	0.025	0.011
Rousset	1200	10	52.8	75.3	0.20	52.5	82.4	0.26	40.9	81.6	0.41	19.9	76.1	1.03	0.20	0.048	0.008
Labbe	1200	10	52.8	75.3	0.38	52.5	82.9	0.51	40.9	81.7	0.87	19.9	80.2	2.41	0.20	0.047	0.015
Presented	1200	10	52.8	75.2	1.12	52.5	82.5	1.41	40.9	81.8	2.12	19.9	73.7	5.02	0.20	0.048	0.051
Rousset	1210	120	52.3	74.6	0.11	50.7	79.7	0.14	39.8	79.3	0.23	20.0	76.6	0.56	0.18	0.037	0.005
Labbe	1210	120	52.3	75.3	0.12	50.7	80.5	0.16	39.8	80.3	0.28	20.0	78.1	0.77	0.18	0.034	0.005
Presented	1210	120	52.3	74.0	0.33	50.7	79.1	0.42	39.8	78.4	0.63	20.0	76.7	1.50	0.18	0.040	0.015
Rousset	2400	10	53.8	76.7	0.26	52.6	82.6	0.34	37.5	74.8	0.55	16.8	64.0	1.37	0.22	0.072	0.011
Labbe	2400	10	53.8	76.5	0.54	52.6	82.8	0.72	37.5	75.4	1.22	16.8	73.0	3.38	0.22	0.070	0.021
Presented	2400	10	53.8	77.0	1.56	52.6	81.7	1.97	37.5	74.7	2.96	16.8	62.0	7.02	0.22	0.072	0.071
Rousset	2410	120	52.8	75.3	0.12	50.8	79.8	0.16	40.1	79.9	0.25	18.8	72.1	0.62	0.18	0.036	0.005
Labbe	2410	120	52.8	75.8	0.16	50.8	80.5	0.22	40.1	81.0	0.37	18.8	74.7	1.03	0.18	0.033	0.006
Presented	2410	120	52.8	74.9	0.45	50.8	79.1	0.57	40.1	79.5	0.86	18.8	71.9	2.05	0.18	0.038	0.021
Rousset	3600	10	56.5	80.5	0.35	50.1	78.7	0.46	35.5	70.8	0.73	16.8	64.1	1.84	0.21	0.064	0.015
Labbe	3600	10	56.5	80.8	0.75	50.1	80.4	1.00	35.5	74.2	1.70	16.8	72.4	4.71	0.21	0.057	0.029
Presented	3600	10	56.5	80.3	2.18	50.1	77.2	2.76	35.5	70.0	4.14	16.8	61.9	9.81	0.21	0.067	0.099
Rousset	3610	120	52.6	74.9	0.14	49.4	77.7	0.18	41.8	83.2	0.29	19.8	75.7	0.71	0.19	0.048	0.006
Labbe	3610	120	52.6	75.4	0.22	49.4	78.3	0.30	41.8	83.2	0.51	19.8	81.2	1.40	0.19	0.045	0.009
Presented	3610	120	52.6	74.5	0.64	49.4	77.2	0.80	41.8	83.8	1.21	19.8	74.1	2.86	0.19	0.050	0.029

Table 4.2: Results from partial volume correction of measured syringe data (Syringe diameters 14.8, 11.9, 8.6 and 4.7mm) from Rousset, Labbé and Presented method: value with no correction (NC) value after correction ($\hat{x}$) and estimated standard deviation of value ($sd(\hat{x})$).

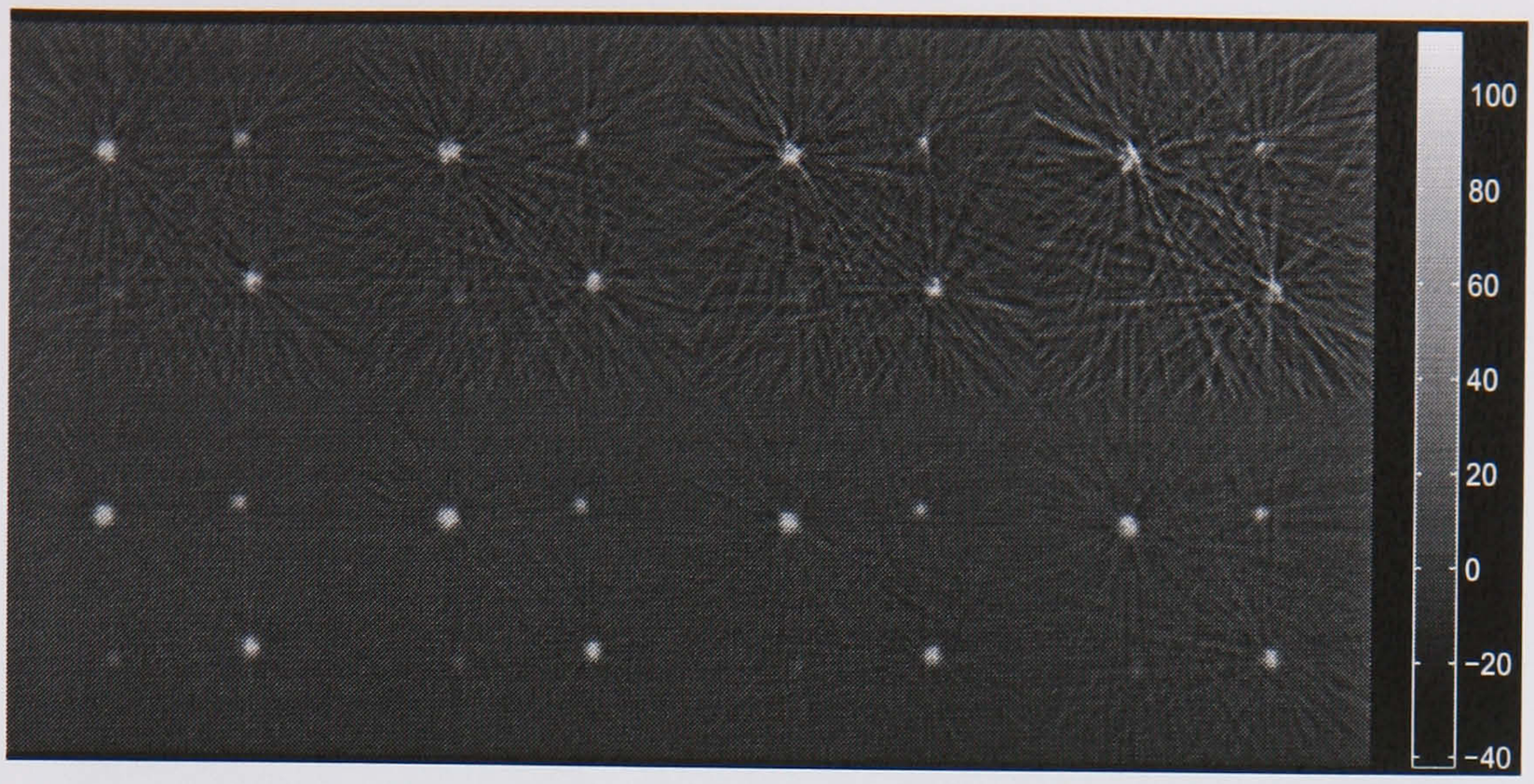


Figure 4.5: Measured Syringe Data: (top) 10s acquisitions (one half life apart), (bottom) 120s acquisitions (one half life apart).

had perfect noise specification. However, the new method gives apparently more plausible estimates for the error of the estimate, given the true value, especially in the higher noise frames.

4.6 Flum Simulations / Measured

The flumazenil simulation was generated using the measured flumazenil data set analysed below. The data was simulated using the region definitions (R) combined with the tissue classifications (T) (Figure 4.6) . The simulated V_D values were taken from the measured results. It was then smoothed with the assumed PSF. The noise added was also taken from the noise estimate of the real data (± 0.43). The presented analysis was again used, in a similar way to the syringe data. The estimated noise characteristics of the real model were used to describe the noise in the simulations.

An [^{11}C]Flumazenil data set was obtained from an ongoing clinical study and acquired according to a protocol described previously (Koepp et al., 1996; Richardson et al., 1996). Briefly, the scan was performed in 3D mode on a 953 B Siemens/CTI PET camera with a reconstructed image resolution of approximately 4.8x4.8x5.2 mm at FWHM (Bailey, 1992) for 31 simultaneously acquired planes with reconstructed voxel sizes of 2.09x2.09x3.42 mm. A convolution subtraction method was used to correct for scatter (Bailey and Meikle, 1994) and axial scaling with the inverse of the scanner's axial profile was applied to obtain uniform efficiency throughout the field of view (Grootoonk, 1995). Voxel-by voxel parametric images of [^{11}C]flumazenil volume-of-distribution (V_D) were then produced from the brain

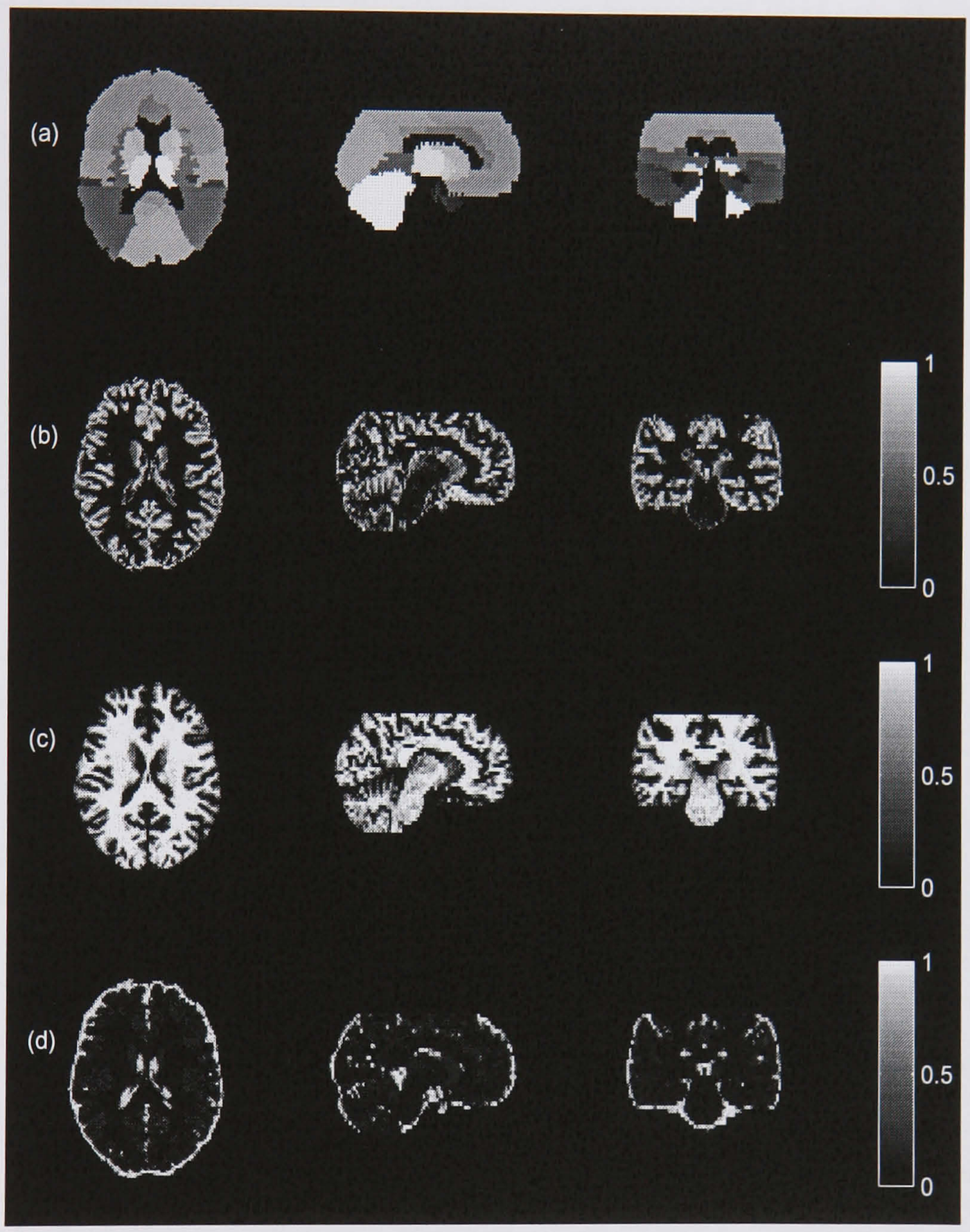


Figure 4.6: Flumazenil Data Set : (a) Definition of the 43 regions for the flumazenil data set represented by different grey levels (corresponding to R). (b) grey (c) white and (d) CSF tissue classification probabilities (corresponding to T).

uptake and arterial metabolite-corrected plasma input functions using a single compartmental tracer kinetic model and estimates of the variance of the parameters calculated (Aston et al., 2000). The methods of estimation of these parameters are derived and discussed in greater detail in chapter 5. A region template containing 43 regions was used which was derived from the MRI of a single brain (Holmes et al., 1998) which has been widely used as a reference brain. To subdivide the flumazenil data set, the region template was spatially warped to fit the individual's MRI data set. This was performed using linear and nonlinear transformations (Ashburner and Friston, 1999) with parameters derived from the MRI data set associated with the template (Hammers et al., 2002). The individuals own MRI was also segmented (Lemieux et al., 1999) into grey matter, white matter and CSF. The transformed region template and the MRI data sets were then coregistered with the PET data set (Ashburner and Friston, 1997). PVC to recover the corrected V_D values was applied using weights derived from the variance map calculated as part of the analysis.

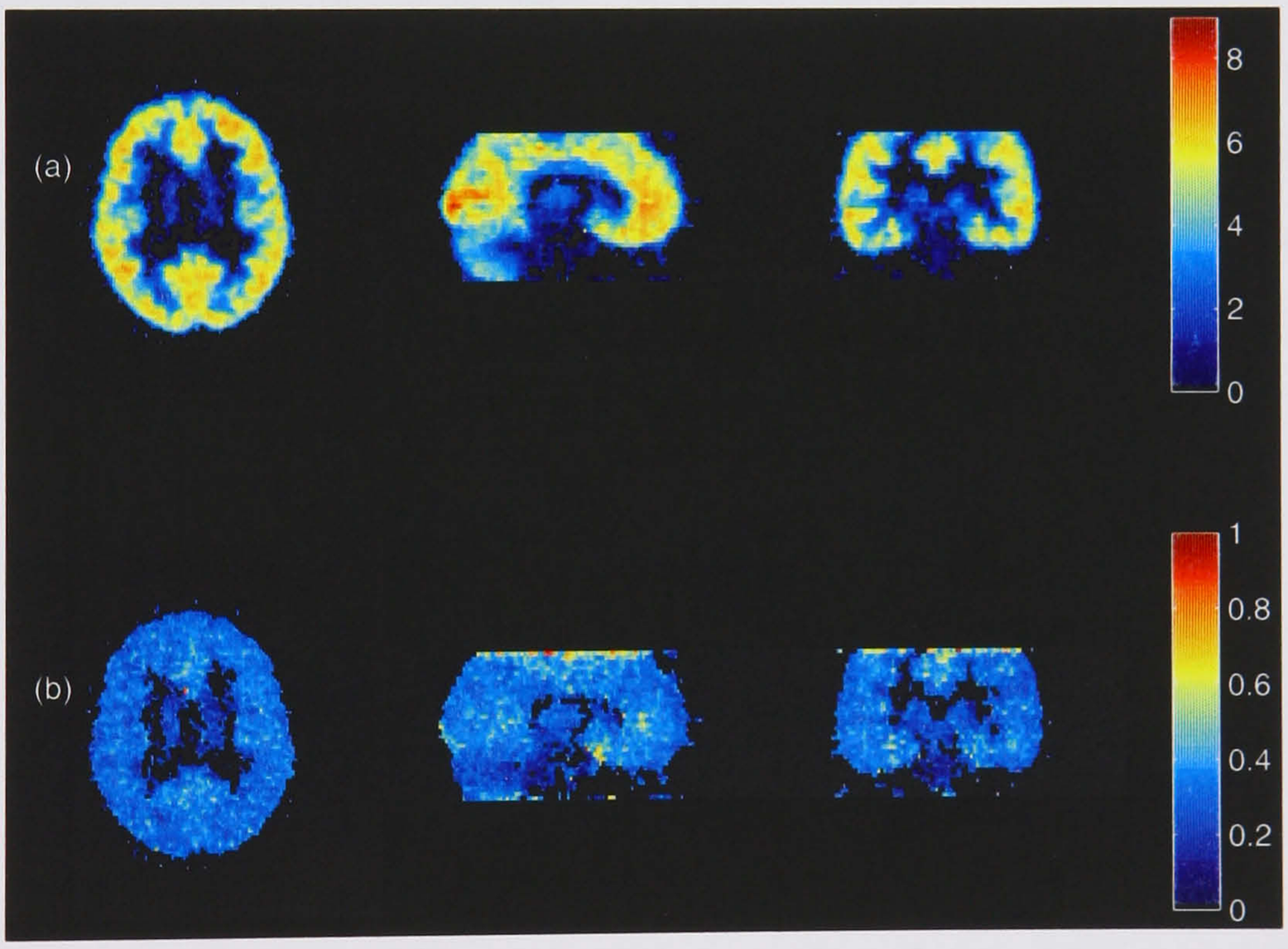


Figure 4.7: Flumazenil (a) Volume of Distribution and (b) standard deviation data prior to correction.

The recovered image from the simulation is shown in Figure 4.8. There was a good correlation between the recovered values and the simulated values (R=0.98) in the grey and white regions (Table 4.3), although CSF regions were not well recovered. This is due to the low probability of the CSF in some regions, and the consequent difficulty in estimation. The actual values for the CSF, however, are not usually of interest, but it is

Region	GM True	GM Rec	GM Sd	WM True	WM Rec	WM Sd
R Amygdala	7.21	5.32	0.35	0.48	1.25	0.33
L Amygdala	5.83	4.28	0.35	0.37	0.65	0.27
R Mid Inf Temp Gyrus	8.32	7.70	0.17	1.80	1.94	0.03
L Mid Inf Temp Gyrus	10.83	10.86	0.08	2.49	2.67	0.03
R Frontal Lobe	9.23	9.03	0.03	2.31	2.45	0.01
L Frontal Lobe	8.81	8.63	0.03	2.96	3.14	0.01
R Parietal Lobe	10.38	10.25	0.04	1.81	2.02	0.01
L Parietal Lobe	10.51	10.53	0.04	2.02	2.25	0.01
R Occipital Lobe	7.51	7.36	0.06	4.19	4.31	0.02
L Occipital Lobe	6.73	6.53	0.06	4.46	4.64	0.02
R Thalamus	4.76	5.09	0.18	1.81	1.88	0.03
L Thalamus	5.32	5.21	0.16	1.10	1.20	0.03
R Cerebellum	6.26	6.24	0.03	2.31	2.44	0.01
L Cerebellum	6.61	6.54	0.03	2.12	2.25	0.01

Table 4.3: Results from simulated [^{11}C]flumazenil data set: Grey Matter (GM) and White Matter (WM) V_D values recovered by partial volume correction (Rec) for a representative set of anatomical regions.

important to include them in the model.

The algorithms speed is related directly to the number of regions and tissue classifications defined (rt). The time increases linearly (assuming the algorithm does not have to be split for memory purposes), with an addition of approximately 10-15 secs per extra classified region.

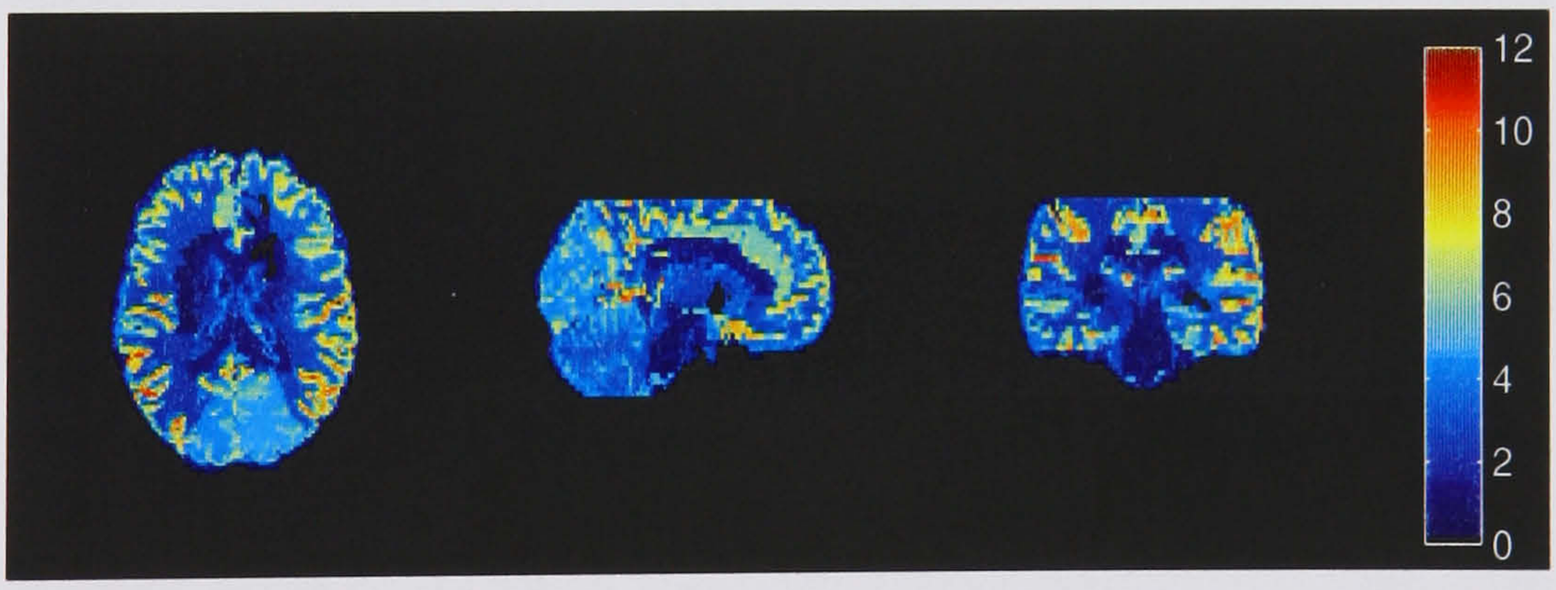


Figure 4.8: Simulated Flumazenil data projected onto MRI template.

The flumazenil data was well recovered in the measured data (Figure 4.9, Table 4.4), except in the few regions where the grey/white border is less well defined (eg Occipital Lobe), giving the impression that the binding was taking place in the white matter. Again the CSF was highly variable and as such is not included in Table 4.4.

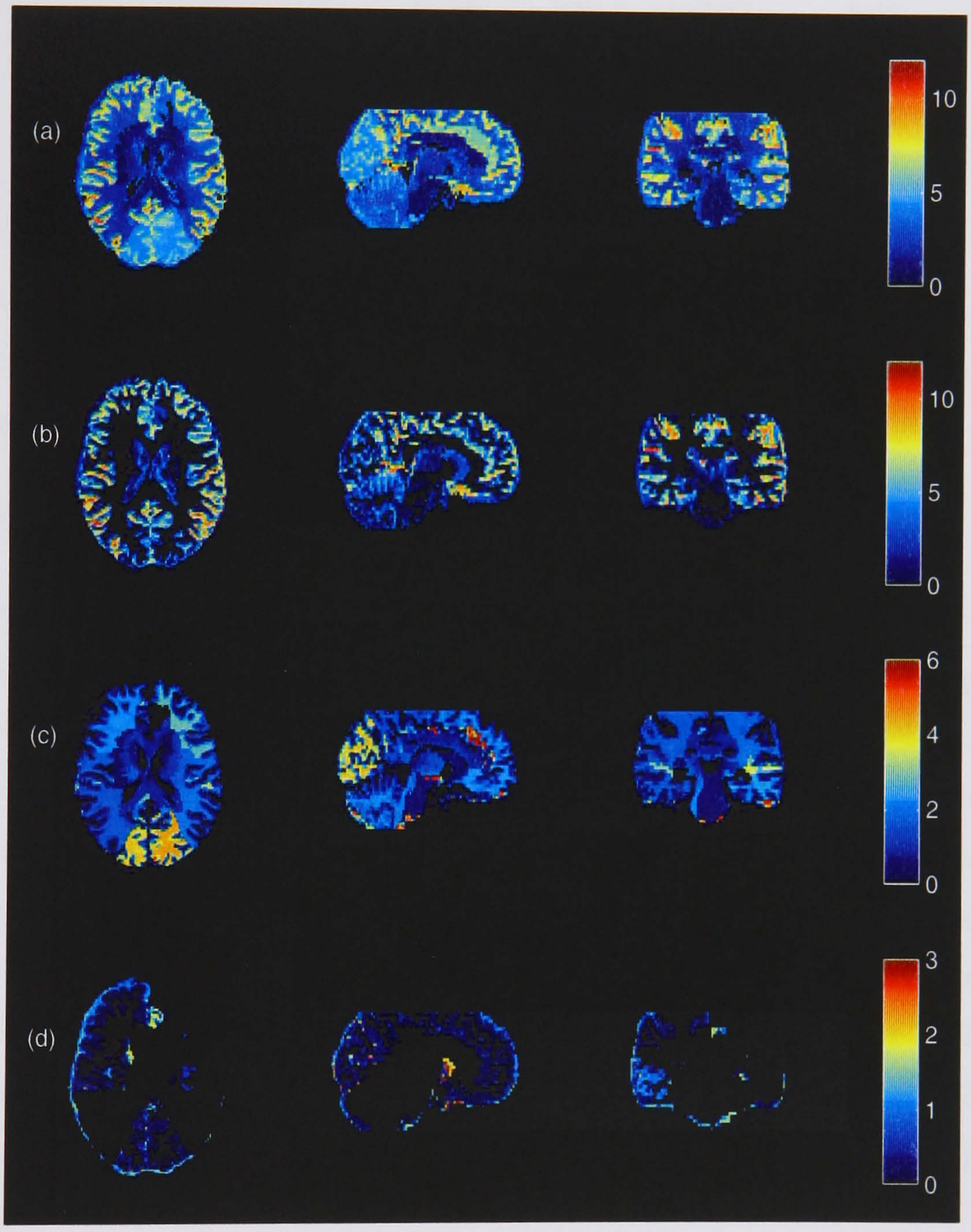


Figure 4.9: Measured Flumazenil data projected onto segmented MRI template; (a) Total (b) Grey Matter (c) White Matter (d) CSF.

Region	GM Pre	GM Rec	GM Sd	WM Pre	WM Rec	WM Sd
R Amygdala	3.30	7.21	0.39	2.78	0.48	0.38
L Amygdala	4.01	5.83	0.40	2.68	0.37	0.31
R Mid Inf Temp Gyrus	5.51	8.32	0.20	3.56	1.80	0.04
L Mid Inf Temp Gyrus	5.90	10.83	0.09	3.91	2.49	0.04
R Frontal Lobe	5.78	9.23	0.03	3.55	2.31	0.01
L Frontal Lobe	5.35	8.81	0.03	3.91	2.96	0.01
R Parietal Lobe	5.85	10.38	0.05	2.98	1.81	0.01
L Parietal Lobe	5.74	10.51	0.05	3.07	2.02	0.02
R Occipital Lobe	5.47	7.51	0.07	4.86	4.19	0.03
L Occipital Lobe	5.42	6.73	0.06	4.77	4.46	0.03
R Thalamus	2.10	4.76	0.20	1.55	1.81	0.04
L Thalamus	3.06	5.32	0.19	1.13	1.10	0.03
R Cerebellum	4.29	6.26	0.03	2.88	2.31	0.01
L Cerebellum	4.49	6.61	0.03	3.03	2.12	0.01

Table 4.4: Results from measured [^{11}C]flumazenil data set: Grey Matter (GM) and White Matter (WM) V_D values recovered by partial volume correction (Rec) for a representative set of anatomical regions.

4.7 Inhomogeneity Testing

The above algorithms (see 4.4.1) allow estimates of the signal and its associated error. However, they do not facilitate the estimation of the regional SSQ, which is required for inhomogeneity testing. However, there are approximational methods that will in principle converge to the correct value of the regional SSQ allowing the possibility of inhomogeneity testing. However this is highly dependent on the correct specification of the noise model.

If the ROI is defined in a deterministic sense in contrast to a probabilistic sense, then in principle inhomogeneity testing is possible. The ROIs represented in the R matrix can each be associated with a sum of squares error, independently of the other ROIs due to their orthogonal nature (by definition if they are not probabilistically defined). However, implementation requires knowledge of the correctly weighted residuals for each of the orthogonal ROIs which depends on the weighting matrix.

Krylov subspace methods are adept at estimating the square root of symmetric matrices (where the square root is defined to also be symmetric allowing it to be uniquely defined). These methods have previously been rigorously analysed for deconvolution (Schneider and Willsky, 2001), but not for inhomogeneity testing. Whilst a rigorous analysis will not be provided here, it will be demonstrated that these methods work in principle, certainly on well specified noise models.

The major advantages of using a Krylov algorithm is that the matrix that a square

root is required for is not altered by the algorithm (Golub and Van Loan, 1983), so only a method of applying the matrix to vectors is needed and hence Tensor structures already defined can be used to perform the computation in 4.4.1.

In order to evaluate the square root matrix equation, the Lanczos Algorithm (Golub and Van Loan, 1983) is used and its extensions to matrix square roots (Allen et al., 2000). The results from the algorithm allow estimation of the regional sum of squares

$$SSQ_{ROI} = (Rx - P^{-1}b)^T W^{\frac{1}{2}} R_{ROI}^T R_{ROI} W^{\frac{1}{2}} (Rx - P^{-1}b) \tag{4.27}$$

It is known that if the noise model is correctly specified including the underlying value of σ_g^2 then the total sum of squares error will be distributed χ^2 with degrees of freedom equal to the number of data points. This is also true on a subset of the regions if they are independent from the other regions. Thus if it is desired to test the homogeneity of a region, the regional sum of squares error is tested against the size of the region, assuming the correctly specified noise model.

$$SSQ_{ROI} \sim \chi^2(\|ROI\|_0) \tag{4.28}$$

4.7.1 Simulations / Measured

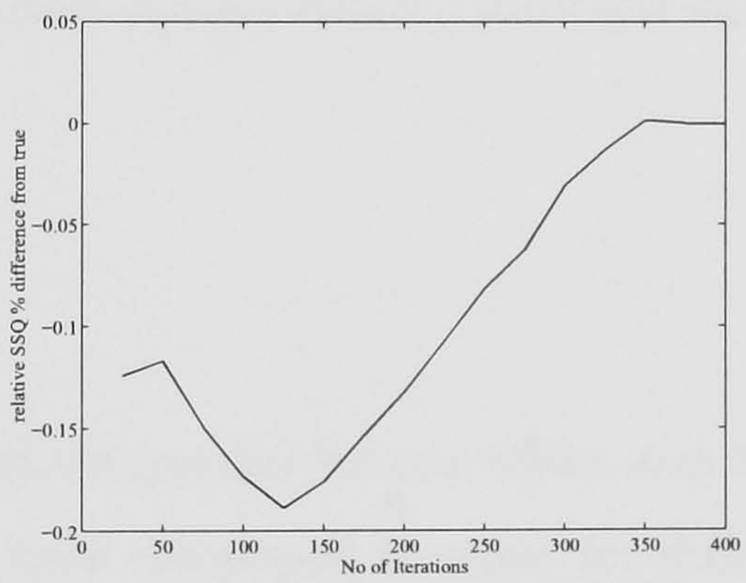


Figure 4.10: Typical Krylov iterations for simulated syringe.

Whilst the overall SSQ for the entire data set was consistent with the noise model, the Krylov subspace approximation was not able to accurately distinguish between the different regional SSQs for a small number of iterations. In principle, however, with a large enough amount of memory the algorithm would become increasingly more accurate. The Krylov subspace algorithms gave a good approximation to the SSQ for a single ROI. As the number of iterations was increased, so was the accuracy of the approximation (Figure 4.10). However, the increase in the number of iterations also required an increase

in memory, and so would not allow the approximation necessarily to be used in practice on larger data sets.

As might have been expected, the Krylov algorithm did not allow for hypothesis testing of homogeneity. This was almost certainly due to inadequate specification of the noise model. The total SSQ was not as expected if the noise model had been correctly specified, and the SSQ of the single syringe was also affected this way. The noise model is of increasing importance from estimation of signal, errors through to hypothesis testing. In the case of hypothesis testing, the noise model must be assumed to be fully characterised, including a known variance. However with more accurate specification of the noise model, the possibility of hypothesis testing remains.

4.8 Future Work

The work presented above allows for the inclusion of noise models into the estimation process. Here, the noise model itself has not been investigated, other than to suggest that it may contain a correlated component due to the PSF, and an uncorrelated component to account for other noise entering the process. Further work could include estimating the noise distributions resulting from different scanners, reconstruction algorithms and corrections. This would facilitate inhomogeneity testing if suitably accurate noise models could be found.

4.9 Summary

This chapter has investigated the partial volume effect and algorithms for its correction. A statistical framework has been developed to allow for different noise models, and previous signal based solutions constructed in this framework. This gives insight into the assumptions that the previous methods implicitly make about the noise structure. A novel algorithm for the inclusion on different noise models into the estimation process have been presented, and shown to converge. The algorithms have also been validated using simulated and measured data. The possibility of extending the work to include inhomogeneity testing has been discussed, and shown to be theoretically possible, whilst needing more accurate specification of the noise model to work in practice. The algorithms and theory developed here, will allow PVC to be routinely implemented in all studies where quantitative analysis of PET data sets is required.

Chapter 5

Non-Linear Compartmental Regression

The ability to acquire a sequence of 3D image volumes over time enables the estimation of biological parameters through parametric modelling. This approach is employed with dynamic PET and fMRI neuroimaging data. The temporal dimension consists of a set of sequential observations of a particular time course either dependent on a set of stimuli (fMRI) or dependent on the kinetics of a particular tracer (PET).

This chapter is concerned with the modelling of PET radiotracer kinetics using a compartmental description of the tracers fate in vivo. While, the methods that are developed are general, they are applied here to the analysis of neuroreceptor imaging data. In particular, methods are developed here to allow for the statistical assessment of changes in neurotransmitter concentrations, which currently is a major PET research area for studies into synaptic neurotransmission (Laruelle, 2000).

Research in PET modelling has concentrated mainly on the estimation of parameter values themselves from compartmental models (Cunningham and Lammertsma, 1994). Typically the data is analysed on a region of interest basis and statistical differences in parameter values are inferred by simple t-tests. The goal of this chapter is not only to estimate the parameter values, but also to obtain information on their certainty and use this more comprehensive description to develop a new method for statistically assessing differences in the biological parameters. Furthermore, the method is applied voxelwise which maintains the full resolution of the neuroimaging data, generating statistical parametric maps.

5.1 PET Compartmental Models

Compartmental models are the fundamental underlying model structures used in PET tracer kinetic modelling. They are a-priori chosen based on biological knowledge of the underlying system. These include simple one tissue compartmental blood flow models (Kety and Schmidt, 1948), through irreversible metabolism models (Sokoloff et al., 1977), to more complex compartmental models describing free, non-specific and specific binding parameters for neuroreceptors systems. The quantification process requires an input function which can be derived either from blood or (if available) a suitable reference tissue. Reference tissue models have been developed recently to avoid the need for arterial blood sampling and have led to another range of compartmental structures (Gunn et al., 2001b). The complexity of the model is determined by both the data itself, the signal to noise ratio, and the underlying biology.

Compartmental models can describe how a tracers changes state or location. Tracers are molecules which are assumed to mimic properties of the system, but whose presence does not alter the system itself. The compartmental models used are simplifications of the true states of the tracer but give a representation that allows reproducible modelling whilst being sensitive enough to detect changes in the underlying system. All these models have an associated set of assumptions and the simpler they are, the more assumptions they tend to have. The increased assumptions increase the robustness of the parameter estimation process at the possible cost of an increased bias. There are certain assumptions that are common to all PET compartmental systems e.g. each compartment represents a homogeneous concentration of the tracer (the compartment is well mixed). Typically models with two or three compartments are the most complex models that can be supported by the data. Using the Law of Mass Action it is possible to deduce a set of differential equations that describe the rate of change of concentration of the tracer in each of the compartments. A more detailed description of compartmental modelling in PET (Huang and Phelps, 1986) has been given previously along with the associated parameter estimation process (Carson, 1986).

Recently, compartmental analysis in PET and the mathematical framework underlying these models has been rigorously investigated using linear systems theory (Gunn et al., 2001b). PET compartmental model systems are characterised by the use of first order tracer kinetics, implying that the system is time-invariant in the parameters, and can be

defined using linear system theory as follows

$$\begin{aligned} \dot{x}(t) &= Ax(t) + Bu(t) \\ y(t) &= Cx(t) + Du(t) \\ x(0) &= x_0 \end{aligned} \tag{5.1}$$

where $x(t)$ is a p-vector of state variables, $y(t)$ is a n-vector of the observed data, $u(t)$ is an r-vector of the inputs to the system, $A = \{a_{ij}\}$ is the $(p \times p)$ transition matrix from state to state, $B = \{b_{ij}\}$ is the $(p \times r)$ input to state matrix, $C = \{c_{ij}\}$ $(n \times p)$ is the observation matrix, $D = \{d_{ij}\}$ $(n \times r)$ is the seen input matrix, and x_0 is a p-vector of the initial conditions of the system states (Gunn et al., 2001b).

In practice, all commonly used PET compartmental systems are acyclic which implies that the matrix A is negative semidefinite (Schmidt, 1999). The level of complexity of the matrices above depends on the a-priori model selection. The entries of the matrices are linear functions of the "biological" rate constants $\{k_i\}$ while also being functions (not necessarily linear) of other biological parameters of interest, which are themselves functions of the rate constants.

The general solution of the impulse response functions for an m compartment system, given by Gunn (Gunn et al., 2001b), is as follows:

$$\mathrm{IRF}(t) = \phi_0 \delta(t) + \sum_{i=1}^{m} \phi_i e^{-\theta_i t} \tag{5.2}$$

where ϕ_i and θ_i are functions of the $\{k_i\}$ (often non-linear functions), and where ϕ_0 is 0 for plasma input models, ϕ_m is 0 for reference tissue models. For irreversible models, θ_m is 0 for plasma input functions, and θ_{m-1} is 0 for reference tissue models. The form of the operational equation however differs depending on the type of model used, namely plasma or reference tissue.

$$\begin{aligned} \text{Plasma} \quad C_T(t) &= \mathrm{IRF}(t) \otimes C_P(t) \\ \text{Reference} \quad C_T(t) &= \mathrm{IRF}(t) \otimes C_R(t) \end{aligned} \tag{5.3}$$

where C_T, C_R and C_P are the concentrations of tracer in the target tissue, reference tissue and plasma input respectively. Although these are very general equations, if specific assumptions are made, then these equations can be reformulated in explicit terms for the specific compartmental structure.

5.2 Neuroreceptor Studies

5.2.1 Receptor Compartmental Models

The observed time series of PET images of neuroreceptor ligands can be modelled using classical compartmental approaches (Mintun et al., 1984). For most ligands, a two-tissue compartment model is sufficient to account for the observed activity as a function of time. This model is derived from a three tissue compartment description which has compartments for free, non-specifically bound and specifically bound tracer. Typically, the rate of exchange of radiotracer between free and non-specific compartments is greater than that between free and specific compartments, and as such the free and non-specific compartments may be approximated by a single compartment. For some radioligands, the rate of exchange between all tissue compartments may be sufficiently rapid that the model can be approximated by a single tissue compartment (Figure 5.1 shows the assumptions). Using these models it is possible to obtain parameters such as the volume of distribution or binding potential. These macro-system parameters are proportional to the rate constant representing transfer from the free to specifically bound compartment (typically denoted k_3). k_3 is a pseudo first order rate constant that is proportional to the concentration of available receptor sites.

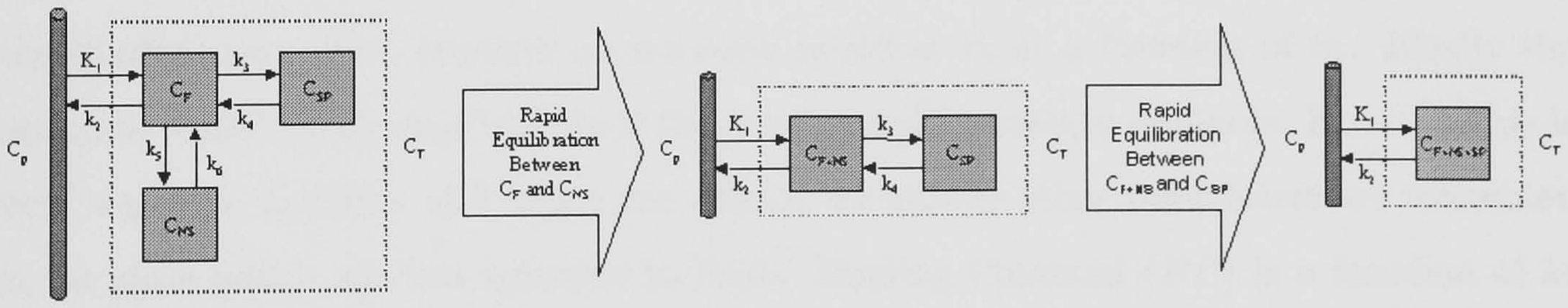


Figure 5.1: The assumptions allowing the full model to be characterised by a single compartmental structure. These assumptions can be made in both the reference and plasma input function cases, and is here demonstrated for the plasma input case.

Expanding the definitions of the rate constant in the two tissue compartment model (Mintun et al., 1984) gives a more intelligible view of what these parameters actually reflect biologically.

$$\begin{aligned} K_1 &= = f(1 - e^{-\frac{PS_1}{f}}) \\ k2 &= \frac{PS_2}{PS_1} f(1 - e^{-\frac{PS_1}{f}}) \\ k_3 &= \frac{f_2 k_{\text{on}} B_{\text{max}}}{1 + \sum_i \frac{F_i}{K_{D_i}}} \\ k_4 &= k_{\text{off}} \end{aligned} \tag{5.4}$$

where K_1 $(mlg^{-1}min{-}1)$ is the plasma to brain transport constant, k_2 (min^{-1}) is the brain to plasma efflux constant, f $(mlg^{-1}min{-}1)$ is the blood flow per gram of tissue, PS_1 and PS_2 $(mlg^{-1}min{-}1)$ are the capillary permeability surface area products for blood to brain and brain to blood respectively, B_{max} $(pmolml^{-1})$ is the total concentration of receptor sites, f_2 is the "free fraction" of unbound radioligand in the tissue, F_i $(pmolml^{-1})$ and K_{D_i} $(pmolml^{-1})$ are the concentration and equilibrium disassociation constants of i competing endogenous ligands and k_{on} $(mlpmol^{-1}min{-}1)$ and k_{off} (min^{-1}) are the bimolecular association and dissociation constants between radio-ligand and binding site. Steady state is assumed during the scan.

It is possible to estimate various differing parameters from the data. The parameter to be estimated, is dependent on the data itself, and the amount of specificity required in the analysis. Most studies are concerned with specific binding of the radioligand to the binding site. This requires an estimate of either k_3 or a function of k_3. Ideally the estimate would be k_3 itself as this is the most specific estimate available. However this is very sensitive to noise, and hence not robust, so usually other parameters are estimated in its place which are less sensitive to noise. Binding Potential (BP) is a function of k_3 and k_4, and is more stable in the presence of noise. VD is even more robust, but this is even less specific than BP in that it is a function of all the rate constants, and hence a change in K_1, k_2 or k_4 would lead to a change in VD. If the parameter of interest is k_3, then this could lead to difficulty in assessing changes.

$[^{11}C]$SCH23390 : D1 receptor ligand

The chapter considers the tracer SCH23390 for validation and simulation studies. SCH23390 is a D1 receptor ligand. There are D1 receptors located in the cortex, but the highest concentration is in the basal ganglia (Figure 5.2).

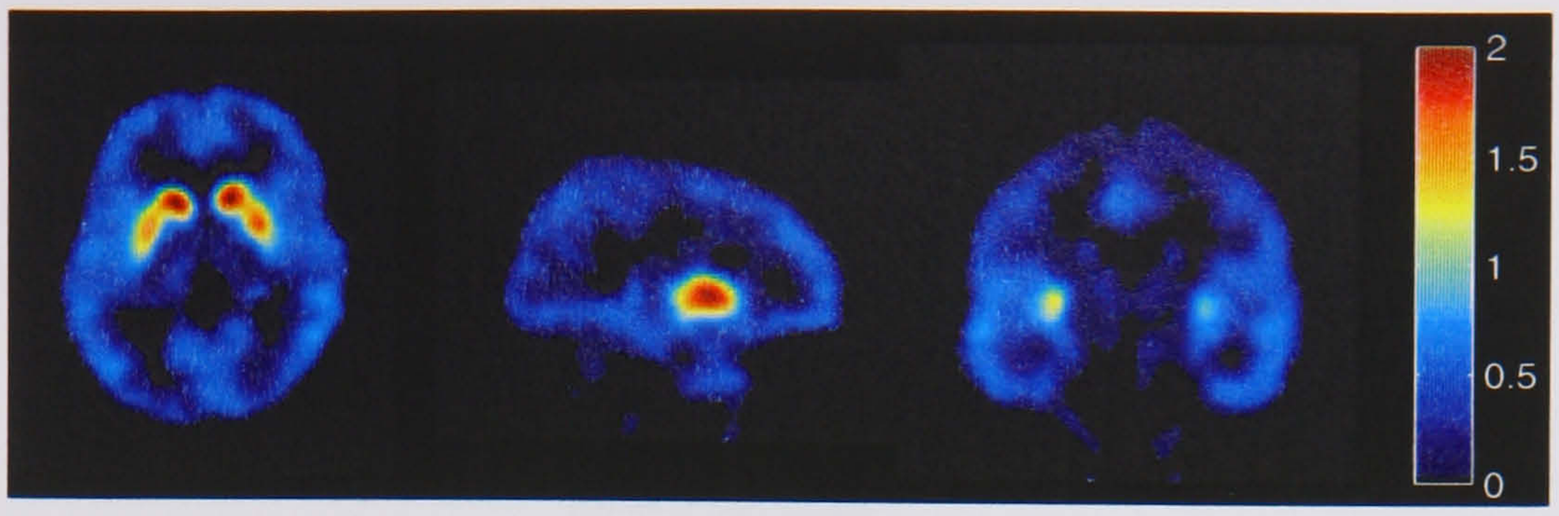


Figure 5.2: A typical binding potential parametric map for $[^{11}C]$SCH23390.

5.2.2 Synaptic Neurotransmission

Neurons in the brain initiate response through electrical and chemical processes. The connections between neurons are known as synapses. Electrical signals travel down the axons until they reach the end of the synapse where they cause the release of chemicals (neurotransmitters) into the synaptic cleft. These neurotransmitters diffuse across the cleft to postsynaptic receptors, where the neurotransmitter binds, opening up gated ion channels into the neuron and causing the build up of an electrical signal in this neuron.

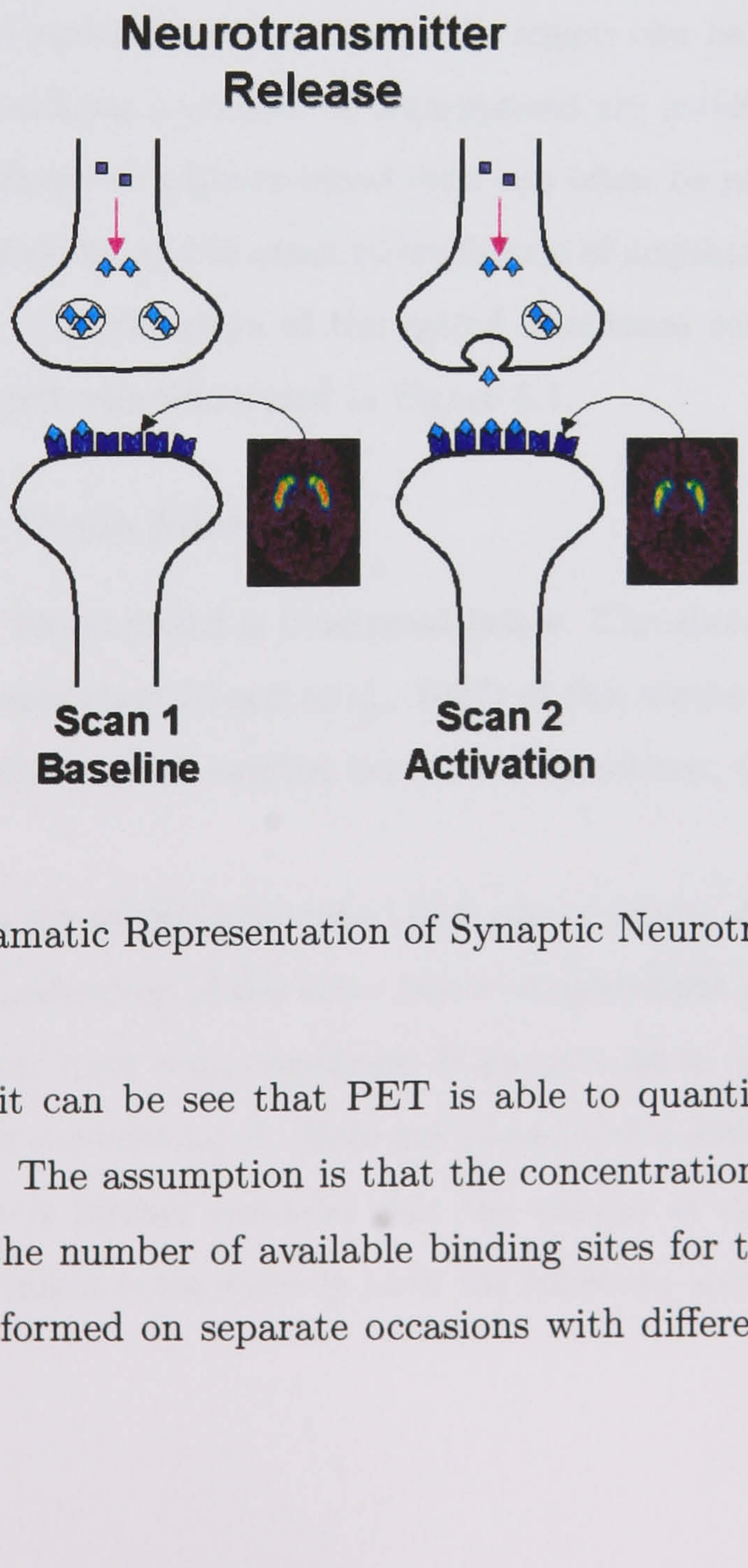


Figure 5.3: Diagramatic Representation of Synaptic Neurotransmitter Release

From equation 5.4 it can be see that PET is able to quantify the concentration of available receptor sites. The assumption is that the concentration of extracellular neurotransmitter influences the number of available binding sites for the radioligand. Thus if two PET scans are performed on separate occasions with different levels of neurotrans-

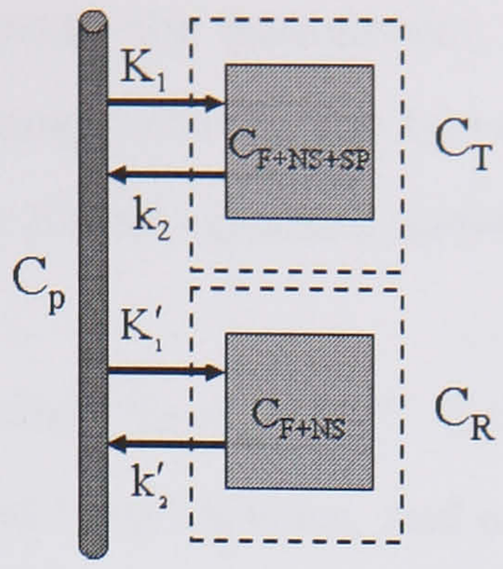


Figure 5.4: The Simplified Reference Tissue Model.

mitter present, it is possible to measure the process of synaptic neurotransmission in man in vivo (Figure 5.3). This has great potential for the study of neurological diseases such as Schizophrenia, Parkinsons, depression and drug addiction.

5.2.3 Reference Tissue Models

The two tissue compartment model is reliant on an input function for solution. If there exists a region devoid of specific receptor sites, this region can be used as a substitute to the input function providing a number of assumptions are satisfied. This is of major advantage as the requirement of adjunct blood data can often be prohibitive both in the case of recruitment of subjects, and in cases where failure of acquisition of the blood data occurs during the scan. Simplification of the model structures can be made in similar fashion to the plasma input case illustrated in Figure 5.1.

Simplified Reference Tissue Model

The simplified reference tissue model is illustrated below. The theory (Lammertsma and Hume, 1996) and implementation (Gunn et al., 1997) of this model is already well established, however it is useful to again outline here the assumptions, theory and implementation.

In this representation the model is described by 6 rate constant, K_1, k_2, k_3, k_4, K_1', and k_2'. This is already a simplification of the three tissue compartment model, as the free and non-specific compartments have been combined. If an attempt is made to solve the simplified system without an external input, there are 5 identifiable parameters $R_1 = K_1/K_1'$, k_2, k_3, k_4, and k_2'. If it is further assumed that the volume of distribution of the free and non-specific compartment is the same in both the reference and the target tissue, the

model can be reduced to incorporate the parameters, R_1, k_2, k_3 and k_4. The final assumption that there is rapid exchange between the two compartments in the target tissue, allows for the simplification to the model equation stated below (Eqn 5.19), involving only R_1, k_2 and $BP = k_3/k_4$.

This could be equivalently worked "backwards". If the model description has only one compartment in both reference and target tissues, and assuming the solution is in terms of the reference, the solution will be in terms of the 3 parameters R_1, k_2' and k_2^*. The further assumptions that the target is actually two rapidly exchanging compartments, and that the volume of distribution is equal in the first compartments, allows the formulation of the model as above, with $k_2^* = k_2/(1 + BP)$.

5.3 Non-Linear Regression

Regression is the process of estimation of parameters and their errors from data, based on the relationship between the data and the parameters, and assumptions about the errors on the data.

Non-Linear Regression is a generalised version of its linear counterpart, and allows for asymptotic functional relationships to be determined between estimated parameters and their errors. To aid the understanding of non-linear regression, linear regression will firstly be reviewed, and comparisons drawn with its non-linear counterpart.

5.3.1 Linear Regression

Throughout this chapter, indeed the entire thesis, linear and non-linear regression will be formulated in terms of matrix equations. The general linear regression problem is to solve the following:

$$y = X\beta + \epsilon \tag{5.5}$$

where y is the data ($n \times 1$ vector), X is the model ($n \times p$ matrix) with linear parameters β ($p \times 1$ vector), and ϵ, is the noise ($n \times 1$ vector). The model can be fitted to the data in a least squares sense by minimising the L_2 distance between the data and model, and provides an unbiased estimate for the parameters (β). If the data has independent normally distributed homogeneous errors, then this estimate is also the best linear unbiased estimate (BLUE) in the sense that it has minimum variance (Gauss-Markov Theorem (Anderson, 1971)).

The least squares solution is found by minimising the following

$$\min_\beta\{S\} = \min_\beta\{(y - X\beta)'(y - X\beta)\}. \tag{5.6}$$

The minimum is determined by differentiating the equation with respect to the parameters (β) and setting this equation to zero,

$$\frac{dS}{d\beta} = -2X'y + 2X'X\beta = 0 \tag{5.7}$$

This is a minimum as $X'X$ is positive definite. Rearranging yields the following least squares solution,

$$\beta = (X'X)^{-1}X'y. \tag{5.8}$$

It can be further shown that the variance on the parameters in this model, when the noise is normally distributed (zero mean, $\sigma^2 I$ variance) is,

$$\mathrm{Var}(\hat{\beta}) = (X'X)^{-1}\hat{\sigma}^2. \tag{5.9}$$

The above estimates are only valid in case of data with normally distributed independent homogeneous errors. In the case of inhomogeneous errors, the estimates can be weighted in order to achieve the BLUE and is known as weighted least squares (Gauss-Markov Theorem).

5.3.2 Non-Linear Regression

Non-Linear regression concerns the fitting of models with the form

$$y = f(\beta) + \epsilon \tag{5.10}$$

where f is a non-linear function in at least one of the parameters β.

Linear regression allows for the solution of some non-linear problems via a suitable reparameterisation. For example,

$$y = \alpha e^{\beta x} \tag{5.11}$$

is a non-linear equation in the parameter β and so technically cannot be solved directly in terms of linear regression. However, if the data is transformed with a logarithmic transform, it can then be solved in terms of a linear model.

$$\begin{aligned} \log(y) &= \log(\alpha) + \beta x, \\ z &= \gamma + \beta x. \end{aligned} \tag{5.12}$$

This can be solved in terms of the new parameters γ and β using linear regression. These methods are of course dependent on the noise structure, and if the original data has normally distributed errors, then this must be considered when making any transform.

However, many non-linear problems cannot be transformed to allow linear regression techniques to be used. The varied methods for finding the solutions to non-linear least squares problems are discussed below.

The general non-linear regression problem is concerned with minimising the following objective function,

$$\min_\beta\{(y - f(\beta))'(y - f(\beta))\}. \tag{5.13}$$

Again, if the errors are inhomogeneous, weighted least squares is more appropriate. With suitable assumptions concerning regularity, it can be shown that the estimates are consistent and asymptotically normal (Seber and Wild, 1989).

There are also asymptotic results concerning the variance of the estimates (Seber and Wild, 1989),

$$\mathrm{Var}(\hat{\beta}) = \left[\left(\frac{\partial f(\hat{\beta})}{\partial \beta}\right)'\left(\frac{\partial f(\hat{\beta})}{\partial \beta}\right)\right]^{-1}\sigma^2. \tag{5.14}$$

Using this result an estimate of the errors on the parameters can be deduced. This is an analogous result to the one obtained with the linear regression variance formula. However, whilst the linear result holds in all cases, the result above is only an asymptotic result for the majority of models.

Non-Linear Least Squares

There are many algorithms for the solution of non-linear least squares (NLLS) problems. Some can be considered in terms of optimization problems, whilst others are specifically designed to exploit the sum of squares properties (Seber and Wild, 1989). The most commonly used algorithms are the Gauss-Newton algorithm, the Levenberg-Marquardt algorithm and the Nelder-Mead Simplex algorithm. A full explanation of these algorithms is not included here, but a complete derivation is provided in Seber (1989) . These algorithms can be used in most NLLS problems, and can be used to calculate estimates in the problems below. However these algorithms are slow, and can be subject to convergence problems especially when there is a low signal to noise ratio. Both of these are important issues to avoid for large and noisy neuroimaging data sets.

5.4 Non-Linear Compartmental Regression

Non-linear compartmental regression analysis aims to combine the models above with the non-linear regression theory to allow for temporal information to be used to estimate variances on parameters, the first level of inference and estimation (Figure 5.5).

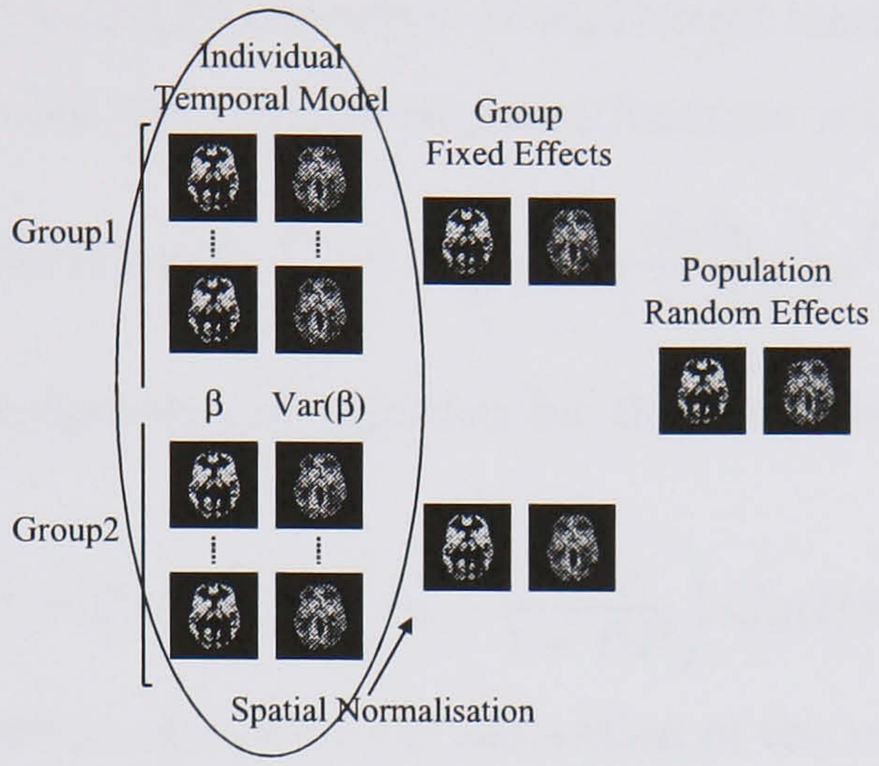


Figure 5.5: Temporal Variance Model

As shown previously, PET compartmental models can be formulated in terms of non-linear functions, and as such non-linear regression is needed to estimate the parameters and their associated errors. Specifically, the parameter variance can be determined in terms of the model equation and the system error σ^2,

$$\mathrm{Var}(\hat{\beta}(k_i)) = V = \left(\left[\frac{\partial C_T(\hat{\beta}; t)}{\partial \beta(k_i)} \right]' \left[\frac{\partial C_T(\hat{\beta}; t)}{\partial \beta(k_i)} \right] \right)^{-1} \sigma^2 \tag{5.15}$$

where

$$\hat{\sigma}^2 = \frac{\sum_{i=1}^{k} (Y(t) - C_T(\hat{\beta}; t))^2}{k - p} \tag{5.16}$$

and p is the number of parameters in the model.

5.4.1 Simplified Reference Tissue Model

The remainder of the chapter concerns the application of these general techniques to the simplified reference tissue model (Lammertsma and Hume, 1996). The simplified reference tissue model allows for the quantification of certain neuroreceptor ligands in terms of the binding potential.

In the notation of the above sections, the state equations for the simplified reference

tissue model (Gunn et al., 2001b) are

$$A = \begin{bmatrix} -k_2^* & 0 \\ 0 & -k_2' \end{bmatrix} \quad B = \begin{bmatrix} K_1 \\ K_1' \end{bmatrix} \tag{5.17}$$

where $k_2^* = k_2/(1+BP)$. Assuming that $K_1/k_2 = K_1'/k_2'$ (equal volumes of distribution for free and non-specific binding in the reference and target tissues) and defining $R_1 = K_1/K_1'$, the following solution for the impulse response function is obtained,

$$IRF(t) = R_1 \left(\delta(t) + \left(k_2 - \frac{R_1 k_2}{1+BP} \right) e^{\left(\frac{-k_2}{1+BP} + \lambda \right) t} \right) \tag{5.18}$$

This implies that the operational equation for the simplified reference tissue model is as follows

$$C_T(t) = R_1 C_R(t) + \left(k_2 - \frac{R_1 k_2}{1+BP} \right) C_R(t) \otimes e^{-\left(\frac{k_2}{1+BP} + \lambda \right) t} \tag{5.19}$$

This operational equation allows for the derivation of the partial derivatives of the model with respect to the parameters and as such the definition of the asymptotic Fisher information matrix.

Let $E(t) = exp\left\{ -\left(\frac{k_2}{1+BP} + \lambda \right) t \right\}$ then

$$\begin{aligned} \frac{\partial C_T(t)}{\partial R_1} &= C_R(t) - \frac{k2}{1+BP} C_R(t) \otimes E(t) \\ \frac{\partial C_T(t)}{\partial k_2} &= \left(1 - \frac{R_1}{1+BP} \right) C_R(t) \otimes E(t) - \left(k_2 - \frac{R_1 k_2}{(1+BP)} \right) C_R(t) \otimes \left[\frac{t}{1+BP} E(t) \right] \\ \frac{\partial C_T(t)}{\partial BP} &= \frac{R_1 k_2}{(1+BP)^2} C_R(t) \otimes E(t) + \left(k_2 - \frac{R_1 k_2}{(1+BP)} \right) C_R(t) \otimes \left[\frac{k_2 t}{(1+BP)^2} E(t) \right] \end{aligned} \tag{5.20}$$

The degrees of freedom for this model are $df = (k-3)$, where k is the number of temporal frames in the dynamic PET acquisition.

5.4.2 Separable Least Squares

Separable Least Squares (Seber and Wild, 1989) problems are a subset of least squares problems, which can be solved using more efficient algorithms than standard Non-Linear Least Squares algorithms (see 5.3.2). These have the common functional form (Seber and Wild, 1989)

$$y = X(\beta)\alpha + \epsilon \tag{5.21}$$

where β is a non-linear parameter, whilst α are linear parameters for fixed β which can be estimated using linear regression if β are assumed known. In the case of the simplified reference tissue model, with a reparameterisation of the problem, the model can be

expressed in the following way

$$C_T(t) = \alpha_1 C_R(t) + \alpha_2 C_R(t) \otimes e^{-\beta t} \tag{5.22}$$

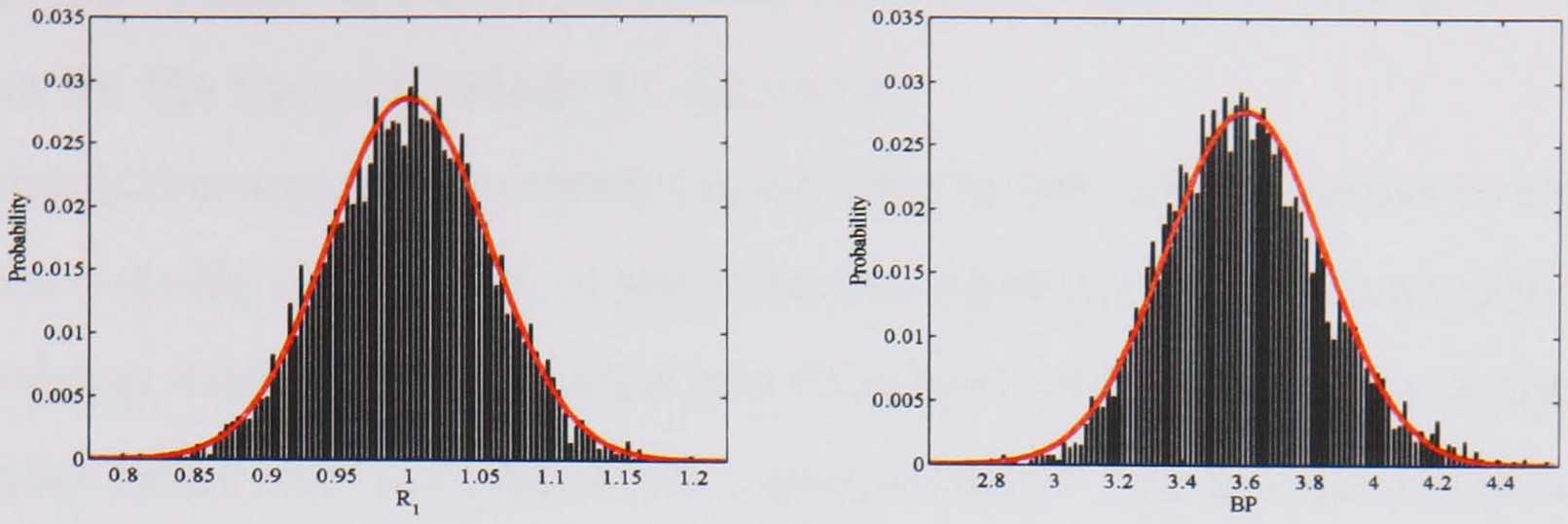
where $\alpha_1 = R_1, \alpha_2 = \left(k_2 - \frac{R_1 k_2}{1+BP}\right)$, and $\beta = \left(\frac{k_2}{1+BP} + \lambda\right)$. This is now in a separable form amenable for solution by separable least squares methods. The implementation (Gunn et al., 1997) of the simplified reference tissue model, is performed using basis function techniques, a method of solution for separable least squares problems. These techniques allow for the fast voxel by voxel computation of the parameters in the model. A selection of basis functions in the physiologically appropriate range of parameter values for β are set up prior to the analysis. The sum of squares of the best linear fit to each of the basis functions is then assessed, and the basis function which minimises this sum of squares chosen. This has the added advantage of constraining the parameters to physiologically sensible ranges. However in order to use non-linear regression theory for subsequent error estimation and inference, the basis function method is required to well approximate the solutions obtained from NLLS algorithms. It has already been shown (Gunn et al., 1997) that these methods do however well approximate NLLS and are more stable in the presence of noise.

5.4.3 Asymptotic Evaluation

A simulation was performed to compare the true sd of the relevant parameters under appropriate noise conditions to the estimated sd from the non-linear regression model. This was done to assess whether the number of data points was sufficient for convergence to the asymptotic results discussed above.

A measured reference tissue TAC and the SRTM model were used to simulate a noiseless target TAC (34 time frames) for a set of typical parameter values ($R_1 = 1$, $k_2 = 0.37 min^{-1}$ and $BP = 3.57$). Multiple noisy realisations (5000) were then generated and the parameter distributions of R_1 and BP determined. These were then compared to the expected distributions (Eqn 5.15) using the mean sds of the parameters generated from the realisations

The plots (Figure 5.6) show that the model and its derivatives provide good asymptotic properties even with relatively few (34) data points. This suggests that the variance estimates will be appropriate to allow hypothesis testing of the parameter estimates.



(a) R_1 Distribution (b) BP Distribution

Figure 5.6: Simulated Parameter Distributions (derived from 5000 noisy realisations) and their theoretical estimated distributions (derived from Eqn 5.19) for the simplified reference tissue model.

5.4.4 Stability Analysis

Given that the simplified reference tissue is a simplification of the processes under study, the following simulations were constructed to assess whether the model could accurately determine changes in receptor availability and that it would be insensitive to changes in blood flow between scans.

Single TACs were generated from a two tissue compartmental model using a plasma input function and parameter values representative of the tracer [11C]SCH23390. These parameter values were varied for a range of concurrent changes in both flow related parameters K_1 (0.0905 $mlg^{-1}min^{-1}$ +20% to -20% in 1% decrements) and $k_2 = K_1/0.3362$ min^{-1} (K_1/k_2 was therefore fixed), and receptor related parameters k_3 (0.135 min^{-1} +0% to -20%, in 1% decrements)and $k_4 = 0.1\ min^{-1}$. The 861 TACs were computed by solving the following differential equations describing a two tissue compartment model for a reversible neuroreceptor ligand using the Runge-Kutta method,

$$\begin{aligned} \frac{dC_f(t)}{dt} &= K_1 C_{pl}(t) - (k_2 + k_3 + \lambda)C_f(t) + k_4 C_b(t) \\ \frac{dC_b(t)}{dt} &= k_3 C_f(t) - (k_4 + \lambda)C_b(t) \end{aligned} \tag{5.23}$$

where $C_{pl}(t)$ is the plasma concentration of radio-ligand, and $C_f(t)$ and $C_b(t)$ the free and bound tracer concentrations in brain. A real measured arterial plasma radioactivity curve was used as the input function (C_{pl}). Normal noise proportional to the signal was then added and 1000 realisations were generated for each of the 861 TACs. The values of BP and its sd were then estimated using the reference tissue model and averaged over the set

of simulations. These recovered parameter estimates were then compared to the initial parameters for the range of values for K_1 and k_3.

This simulation was used to assess the stability of not only the model to changes in the parameters, but also the stability of the estimates when the model is a simplification of the true underlying model. Here the data was simulated with the two tissue compartmental model, whilst fitted with the SRTM i.e. 1 compartment. The asymptotic simulations (see 5.4.3) only accounted for error due to noise in the data, whilst here in addition, there is a model error component as well.

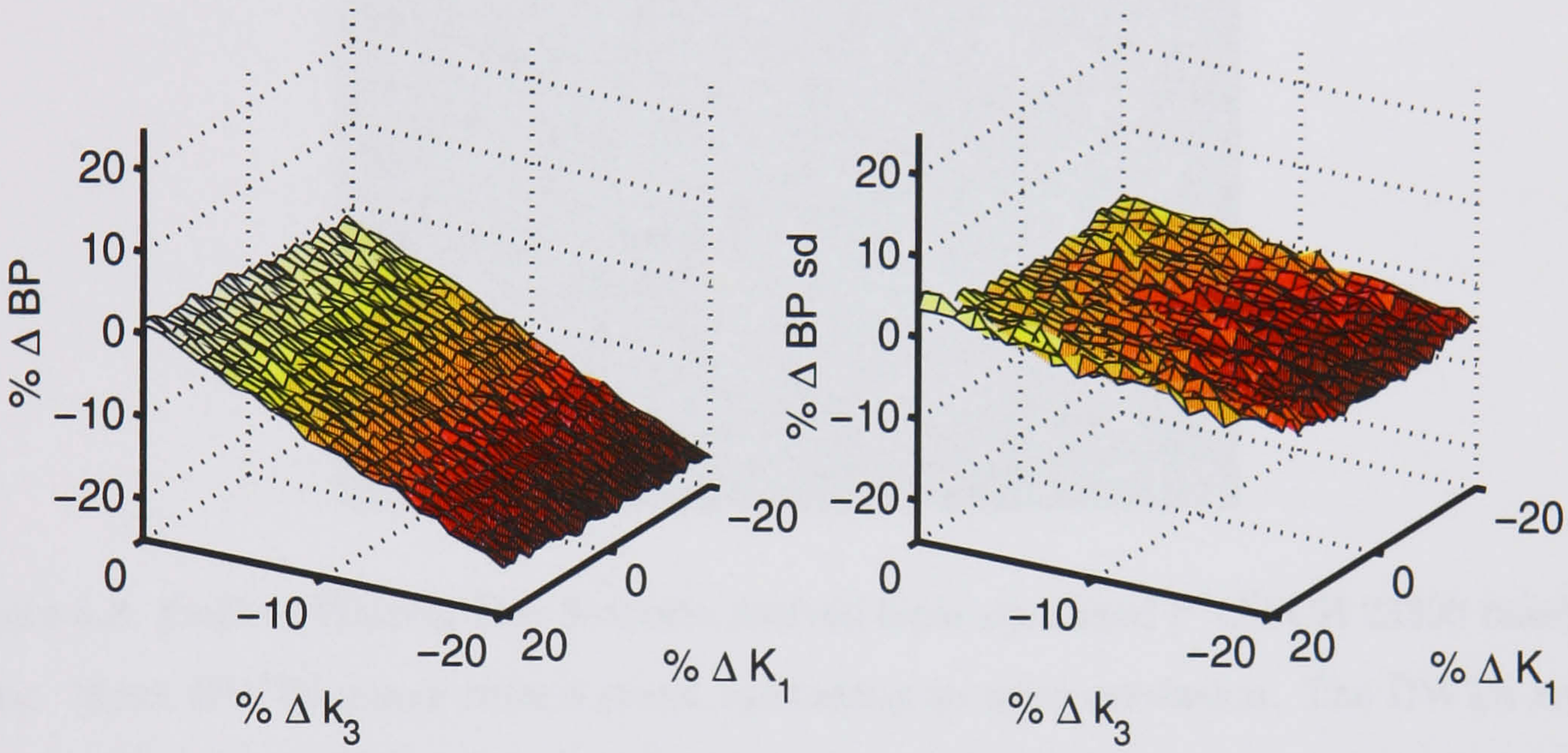


Figure 5.7: ΔK_1 - Δk_3 surface plots for 1000 simulated TACs showing the effects of simulated changes in K_1 and k_3 on the estimated BP. (i) ΔBP (ii) ΔBP sd

The single TAC simulations showed that changes in K_1 had at most a minimal effect on the estimate of BP. A change in K_1 of 20%, which is expected to be the upper limit of the biologically plausible range, caused only a 2% error in the BP estimate (Figure 5.7). The sd remained constant over the different values of K_1 (Figure 5.7). This suggests the method is stable to small deviations from the assumptions that there is only one rapidly exchanging compartment in the tissue in the model.

5.4.5 Autocorrelation

The human [11C]SCH23390 studies described below (see 5.5.2) were used to evaluate the assumption of no temporal autocorrelation in the residuals. The Durbin-Watson test statistic (DWTS) (Durbin and Watson, 1950; Durbin and Watson, 1951; Durbin and

Watson, 1971) can be used to test for autocorrelation between residuals.

$$DW = \frac{\sum_{i=2}^{k}(Z_i - Z_{i-1})^2}{\sum_{i=1}^{k} Z_i^2} \tag{5.24}$$

where Z_i is the i^{th} residual and k is the number of temporal frames. If there is no evidence that the residuals are autocorrelated, then they will be bounded by the upper and lower DW limits (Durbin and Watson, 1950).

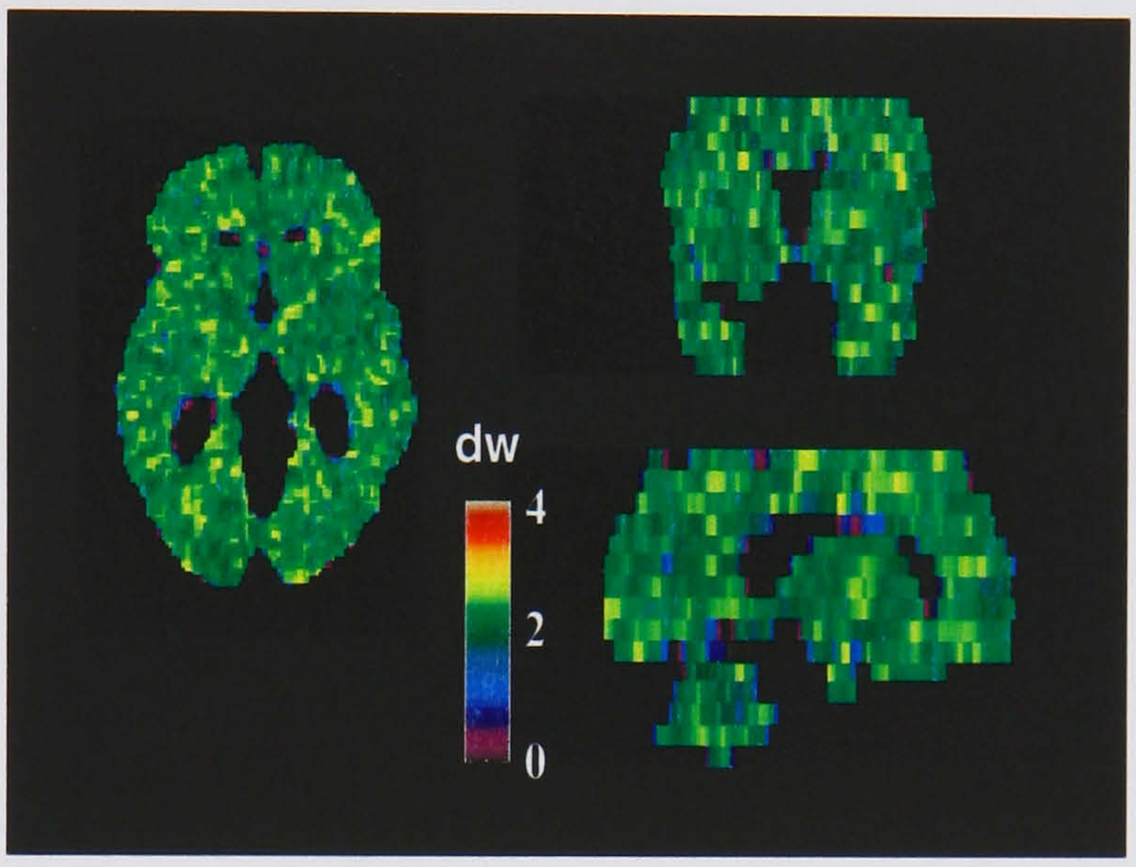


Figure 5.8: Durbin-Watson Test Statistic derived from simulated $[^{11}C]$SCH 23390 baseline scans. Mean DWTS image from 6 scans, indicating no autocorrelation. The DWTS has a value in the interval [0,4], where 0 and 4 equate to positive and negative correlation, while 2 indicates no correlation.

The parametric map from the DWTS (Eqn 5.24) is shown in Figure 5.8. It is without significant anatomical structure. Moreover, taking into account there are multiple observations and hence a larger spectrum of values are anticipated, it is highly unlikely that there is autocorrelation present in the data. Recently developed methods in Gaussian random field theory may, in the future, allow for a more complete analysis of a Durbin-Watson field (Taylor, 2001).

5.4.6 Hypothesis Testing

Having established the non-linear regression formulae (Eqn 5.15), it is necessary to combine these in order to carry out hypothesis testing. Hypothesis testing in this situation, is usually concerned with testing whether there is a difference between either two differing states of the subjects or two differing groups (Figure 5.9). The hypothesis tests below are primarily useful in the former, as there is no accounting for random effects in the data

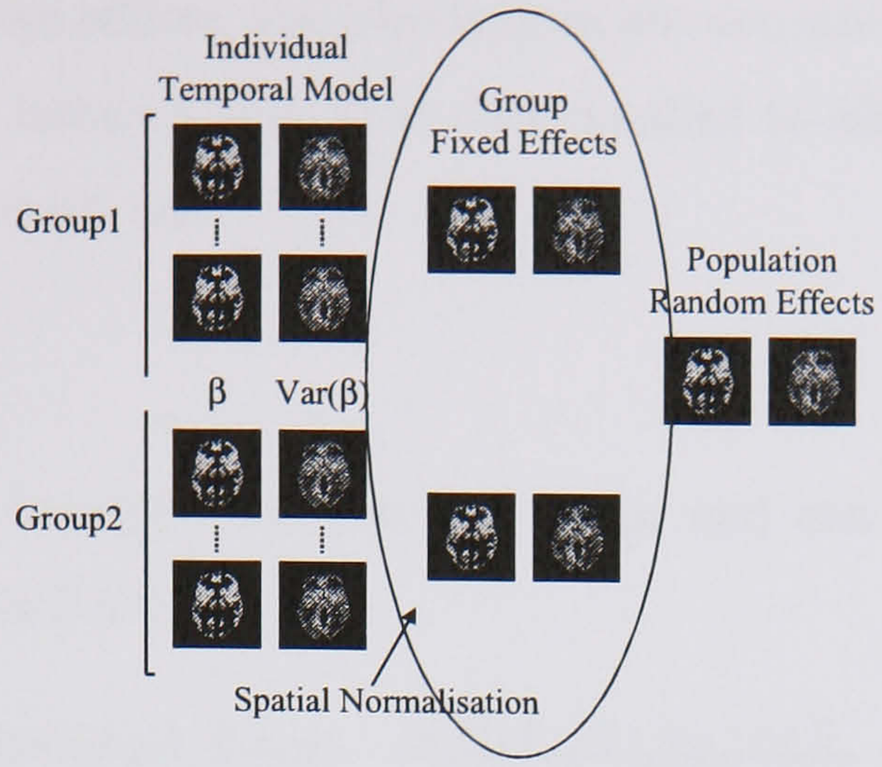


Figure 5.9: Group Level Inference

here. These are considered further in a later chapter 8. The tests (Rice, 1995) below are described in terms of a hypothesis that is concerned with testing for a difference between a baseline and an activation state across subjects.

Paired or Standard T-test

Let $\bar{X} = 1/N \sum_{j=1}^{N} X_j$ and $s_x^2 = 1/(N-1) \sum_{j=1}^{N} (X_j - \bar{X})$ where s_x^2 is an unbiased estimator of σ_x^2, X represents the parameter of interest (eg BP), and N the number of subjects in the study. Let D be the difference between the parameter of interest in the baseline scan (B) and in the activation scan (A), giving $D_j = A_j - B_j$ in the jth subject. If it is assumed that D is normally distributed with mean μ_D and sd σ_D then null hypothesis can be tested using

$$\text{Paired T-test} \quad \frac{\sqrt{N}(\bar{D}-\mu_D)}{s_D} \sim t_{N-1} \tag{5.25}$$

The Paired T-Test can be seen as a generalisation to the population due to the fact that the subject effects are accounted for and D includes the variability across the subjects.

Two-Sample or Pooled Among Groups T-test

If the further assumption is now made that the parameters derived from the two scans themselves are independent and have equal variance ($A \sim N(\mu_A, \sigma^2)$ and $B \sim N(\mu_B, \sigma^2)$), it can be tested whether $\mu_A = \mu_B$ using:

$$\text{Two-Sample T-test} \quad \frac{\sqrt{N}((\bar{A}-\bar{B})-(\mu_A-\mu_B))}{\sqrt{s_A^2+s_B^2}} \sim t_{2(N-1)} \tag{5.26}$$

The two-sample t-test relies on the assumption of independent samples with equal variance. This test cannot be seen as a generalisation to the population as firstly it does

not incorporate subject effects, and also it does not account for subject variability. In fact although this test is detailed here, it is only detailed to allow comparison, as in practice it will not be justified for use.

Residual T-test

The null hypothesis is again whether $\mu_A = \mu_B$ and can be tested using the variance description above (see 5.15)

$$\text{Residual T-test} \quad \frac{\sqrt{N}((\bar{A}-\bar{B})-(\mu_A-\mu_B))}{\sqrt{\sum_{i=1}^{N} \text{Var}(A_i)+\text{Var}(B_i)}} \sim t_{2N(k-p)} \tag{5.27}$$

This test again is not an immediate generalisation to the population and as such has to be seen as a case study. This test is generalised to the population in chapter 8, and this may well be the most appropriate setting for its use. However subject effects are implicitly accounted for, as a separate effect is specified for both the activation and baseline conditions. In the linear model specification (it must be remembered that this is truly a non-linear parameter model, and as such this is a descriptive model as opposed to a real statistical model for the above problem) this model can be specified as

$$E(Y_{ijk}) = \mu_{ij} \tag{5.28}$$

where i is the subject, j is the condition (activation / baseline) and k is the repeat (frame in this case). It should be noted that this in no way accounts for random effects within the scans or subjects. However the differencing within the test does account for the fixed subject effects (it is assumed that the baseline BP is fixed for a given subject) but the hypothesis no longer tests as to whether there is a difference between baseline and activation, rather as to whether the average difference amongst the group between baseline and activation is non-zero in relation to the assumed constant measurement error amongst the group. Careful consideration must be given as to whether it is appropriate to use this test for data especially in light of the fact that measurement error is the only source of variance considered. Again it is assumed that the error sources are independent, but if the only source of error is measurement error, this is likely to be the case (one scan's measurement error is likely to be independent from the next scan). Whilst this model can be considered in the case of different conditions in the same subject, it is highly unlikely that the model would be justified in the case of different subjects for different conditions, such as patient group vs normal group. In this case a random effects analysis would be required.

However there is a new type of test that can be considered in terms of the residual test, that has not previously been possible to consider. This is to test the difference within a single subject i.e.$N = 1$. Previous tests would have not been defined in this situation, but now it is possible to consider whether a single subject has a difference between the two scans. This may be of interest in certain situations where an intrisic value of the parameter is known a-priori in normal subjects such as with the ligand $[^1 1C]$PK-11195, a ligand that binds to glia cells. This is known to have a very low residual binding in healthy brain, whilst having much greater binding in diseased or atrophied brain. The methods above may allow testing of whether the binding is greater than 0 in a single subject with $k - p$ degrees of freedom.

5.5 Validation Studies

Both simulated and measured 3-D data sets were used to evaluate the performance of the new method. The simulations were used to answer specific questions as to the performance of the method in a variety of conditions. Full dynamic PET data were generated using a PET simulator to test the method's sensitivity and accuracy. The measured human data was used to validate the methods in respect to a situation where no positive result was expected. This is important given the field's preoccupation with prevention of false positive results.

5.5.1 Simulation Studies

Simulated dynamic PET data were generated using PETSim, a dynamic PET simulator (Ma and Evans, 1997; Ma et al., 1993). This program takes a segmented MRI image volume (28 regions here), each of which is assigned an activity value, and generates a simulated PET volume (Figure 5.10). The resolution and noise characteristics can be specified. The simulated data used the characteristics of the ECAT HR+ PET camera (CTI, Knoxville, TN) in 3D mode with a resolution of 4 x 4 x 4.2 mm FWHM at the centre of the field of view and images reconstructed using a 6 mm FWHM Hanning filter. For each simulated data set, 34 time frames were generated by calculating time activity curves for $[^{11}C]$SCH 23390 as described above (5.23). A measured real plasma input function was used and the two-tissue compartmental model solved for each region using rate constants for different brain regions taken from human PET data, K_1 (0.08 - 0.13 $ml g^{-1} min^{-1}$), k_2 (0.24 - 0.37 min^{-1}), k_3 (0 - 0.14 min^{-1}), k_4 (0.1 min^{-1}).

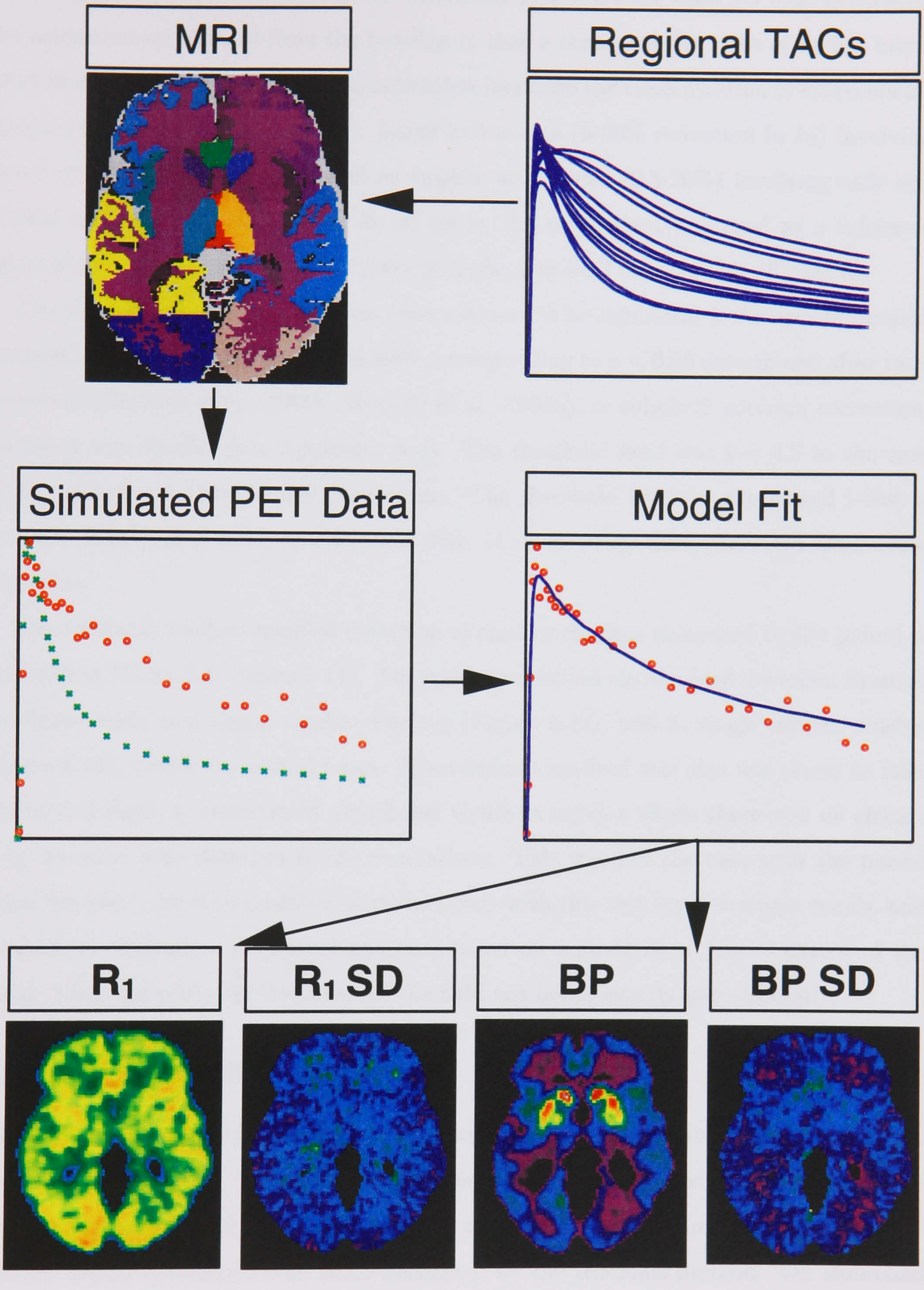


Figure 5.10: Scheme for generation and analysis of simulated data. Characteristic TACs are assigned to each region of a segmented MRI. This enables generation of the dynamic PET data, which are subsequently fitted with the reference tissue model to generate images of model parameters and their SDs

For each subject, a baseline and an activation dynamic PET data set were generated. The activation set differed from the baseline in that a change in the value of k_3 was introduced in certain brain regions. If the activation increases the concentration of extracellular dopamine, then k_3 should decrease. Large activations (5-20% reduction in k_3) involving frontal cortex and striatum, as well as smaller activations (2.5-20%) involving only one caudate nucleus, were simulated. In all cases, the cerebellum was used as a reference region with a value of $k_3 = 0$. The ratio of K_1/k_2 was held constant for all regions.

The simulated subtraction studies were assumed to be significant if the area of interest contained voxels above the threshold level corresponding to $p < 0.05$ determined after resel correction (Worsley et al., 1996b; Worsley et al., 1996a), or simple Bonferroni correction, whichever was smaller (see Appendix A.4). The threshold level was $t = 4.7$ in the case of the residuals statistic in the simulations. The threshold level for the paired t-test is $t = 23.4$ with 5 df (N=6), and $t = 8.8$ with 11 df (N=12), using standard Bonferroni correction.

The residuals method enabled detection of smaller changes compared to the paired t-test method (Table 5.1, Figure 5.11). The residuals method also enabled detection in small structures, such as a single caudate nucleus (Figure 5.12), and in single subject studies (Figure 5.13), unlike the paired t-test. The residuals method was also less prone to false positives, defined as statistically significant voxels in regions where there was no change in k_3, as none were detected in the simulations. This was not the case with the paired t-test; however, the false positives that did occur with this test were at single voxels, and so could be discounted in normal analysis, based on arguments of spatial extent of the signal. They are probably the result of the field not being exactly t-distributed.

Computing sd from Residuals

The t-values generated by pooling among groups and by the residuals method were highly correlated (Figure 5.14). Whilst the two-sample t-test cannot be used because the assumption of independence with no subject effect is not met, it should nonetheless yield images that are highly correlated with those generated by the residuals method. On simulated control data, the voxel-wise correlation of the two statistical maps from the pooled and residuals methods was high ($R2 = 0.966$), with slope and intercept coefficients equal to 1.16 and 0.00284 respectively (Figure 5.14). This test was carried out on approximately 40000 voxels in the image. This confirms that the assumptions in the residuals method

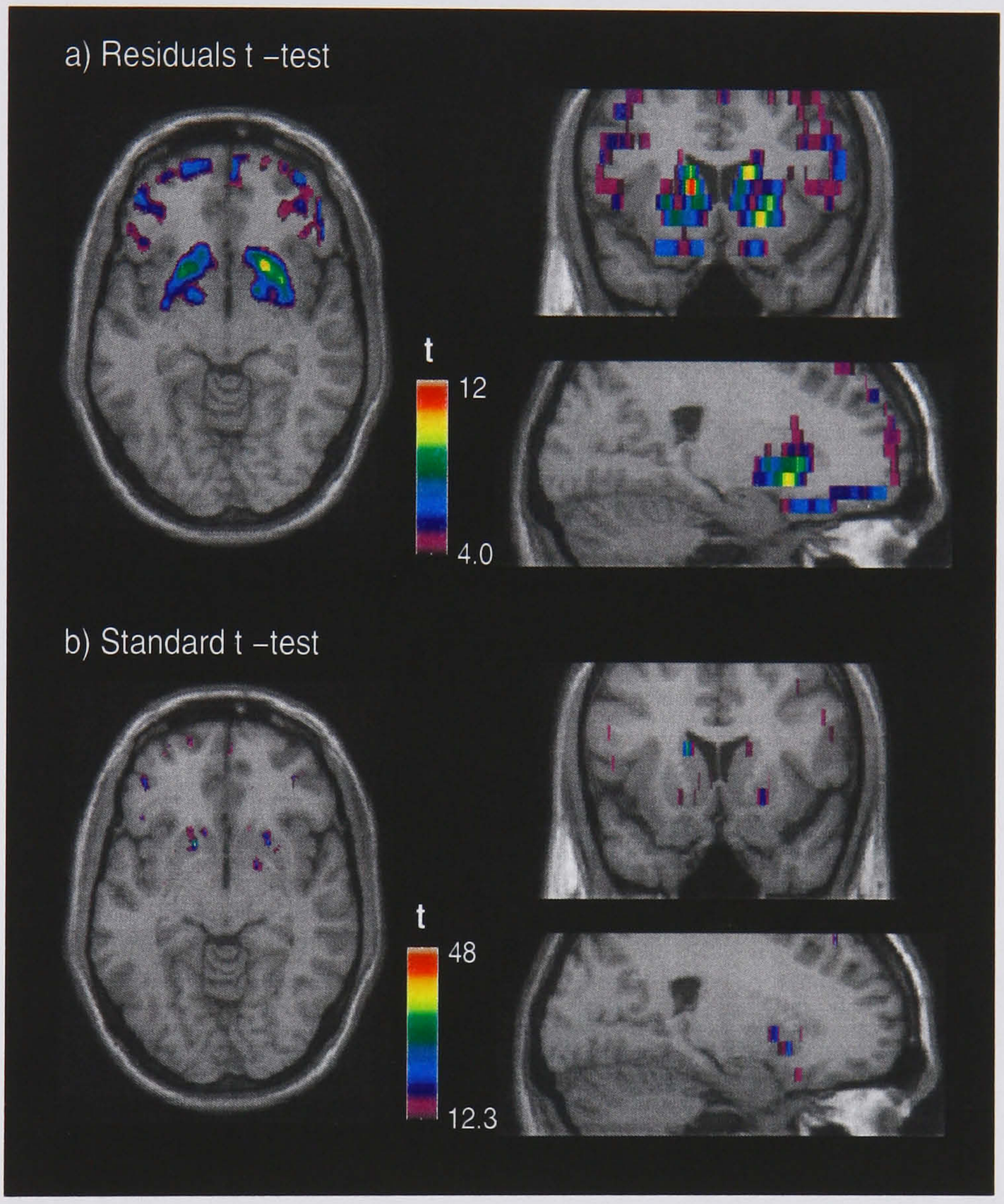


Figure 5.11: Simulated $[^{11}C]$SCH 23390 study with six subjects, each having a baseline and activation scan. In the activation scan there is a 20 % reduction in k_3 in the striatum and frontal cortex for the duration of the scan (90 min). Statistical map of the change in BP; (a) Residuals t test ($t > 4.7$, $P < 0.05$ corrected); (b) Standard t test ($t > 23.4$, $P < 0.05$)

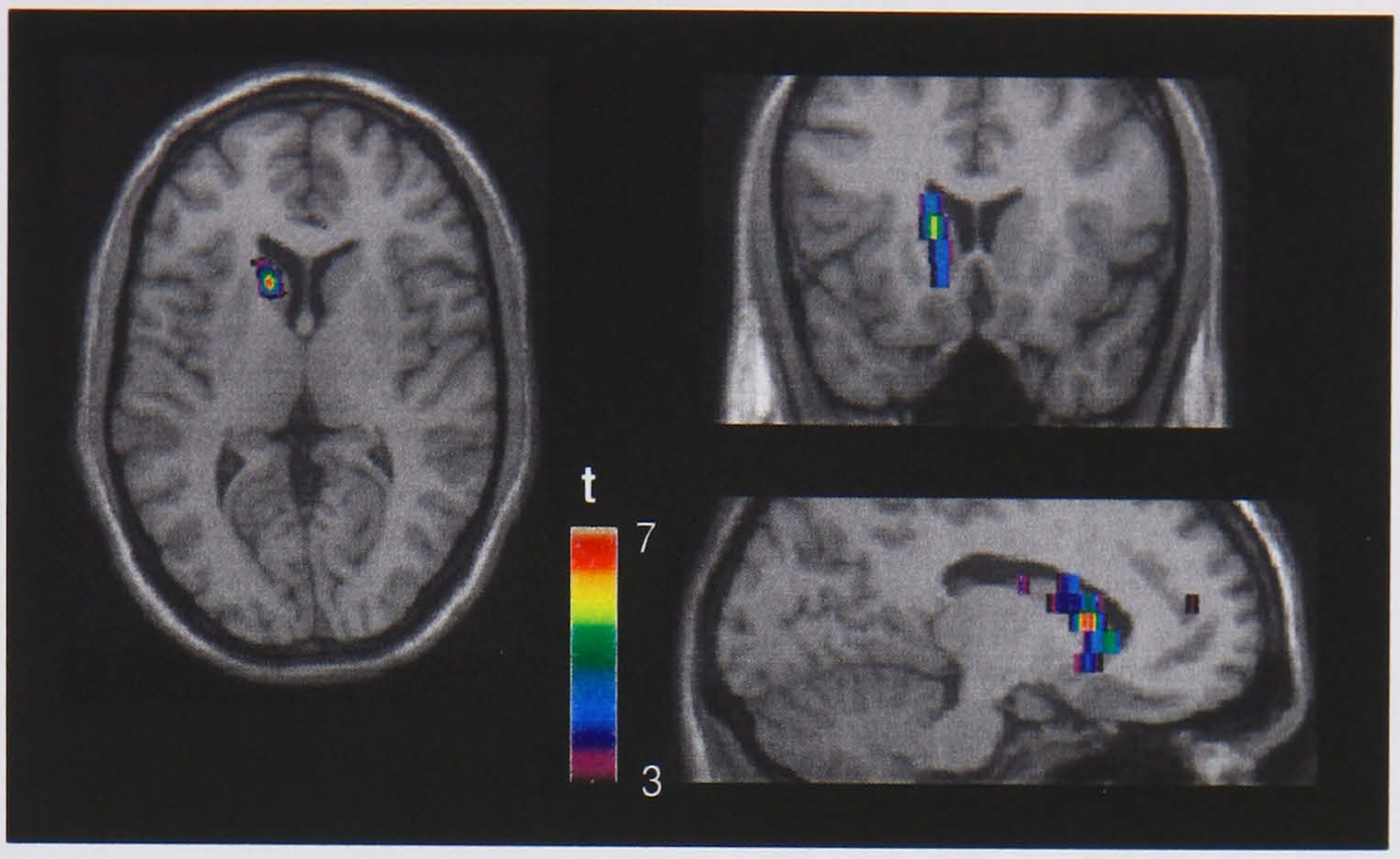


Figure 5.12: Simulated $[^{11}C]$SCH 23390 study with six subjects, each having a baseline and activation scan. In the activation scan there is a 10 % reduction in k_3 in the left caudate for the duration of the scan (90 min). Statistical map of the change in BP with the residuals t test ($t > 4.7$, $P < 0.05$ corrected).

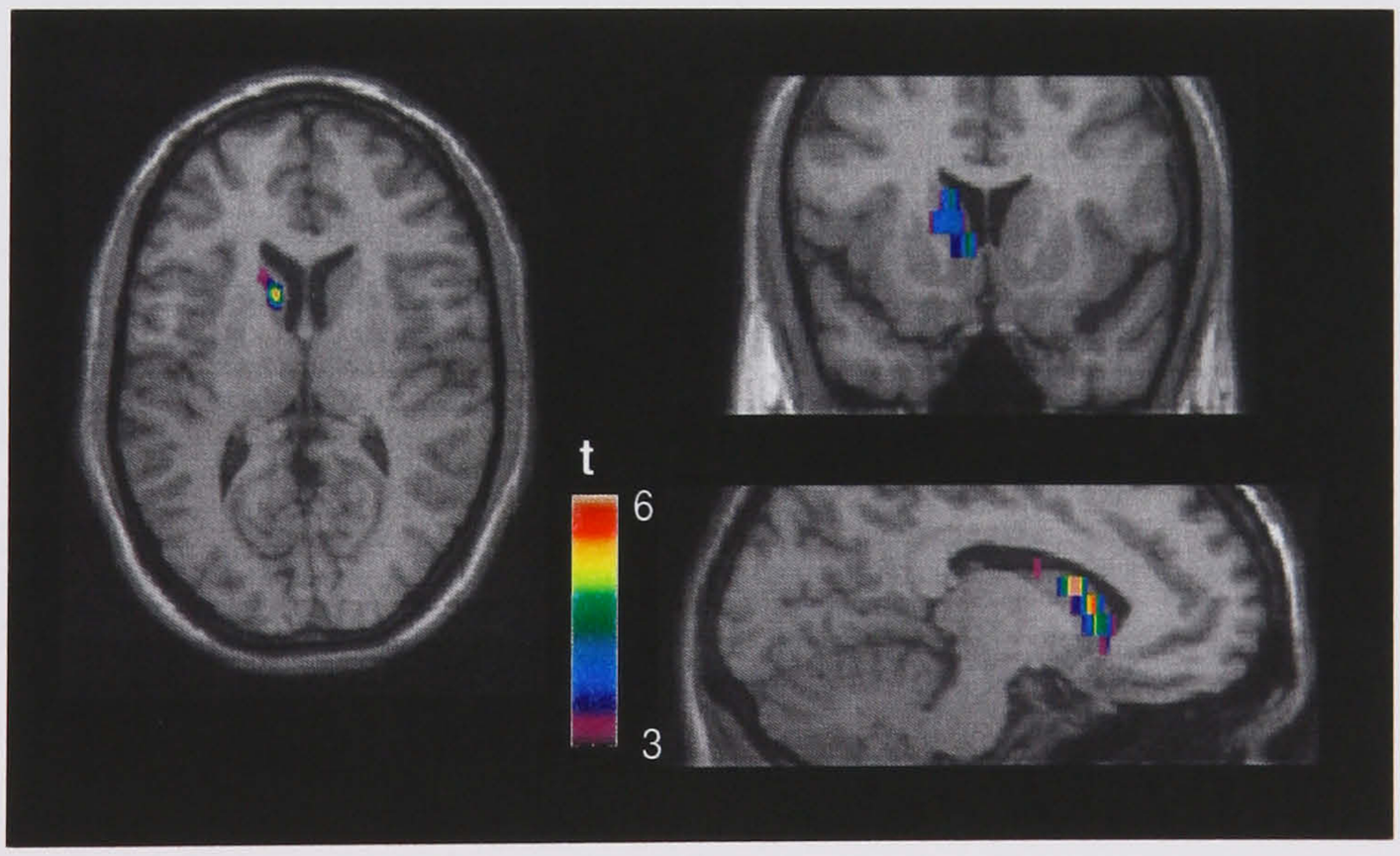


Figure 5.13: Single subject: simulated $[^{11}C]$SCH 23390 study with a baseline and activation scan. In the activation scan there is a 20 % reduction in k_3 in the left caudate for the duration of the scan (90 min). Statistical map of the change in BP with the residuals t test ($t > 4.7$, $P < 0.05$ corrected).

Region	Activation ΔBP (%)	N	Standard t test Max t (p corr)	Vox	Pooled t-test	Residual t test Max t (p corr)	Vox
			Simulated Data				
FC + BG	20	6	48.0(**1.4e-3**)	31	16.7	12.1(**0**)	3398
FC + BG	10	6	24.8(**3.78e-2**)	2	9.57	6.81(**1.85e-7**)	251
FC + BG	5	6	15.6	0	8.22	4.71(**4.71e-2**)	1
L Cau	20	6	32.1(**1.05e-2**)	1	10.9	11.0(**0**)	206
L Cau	10	6	11.7	0	5.89	7.01(**4.53e-8**)	15
L Cau	5	6	6.55	0	3.90	3.93	0
L Cau	5	12	7.72	0	3.57	4.29	0
L Cau	2.5	12	7.09†	0	2.99	3.13	0
FC + BG	5	6	–	–	–	8.88(**0**)	117
L Cau	20	6	–	–	–	11.0(**8.36e-7**)	23
Test-Retest	0	12	7.46	0	4.17	4.37	0
			Human Data				
Test-Retest	0	10	8.15	0	2.7	4.0	0

Table 5.1: Simulated and Measured $[^{11}C]$SCH 23390 Data Set Results

are reasonable.

5.5.2 Measured Data Sets

In addition, to test for false positives, test-retest data from human volunteers scanned with $[^{11}C]$SCH 23390 were used. Ten healthy volunteers (mean age sd: 30 8) underwent dynamic PET studies on the ECAT HR + camera after bolus injection of 370 MBq $[^{11}C]$SCH 23390. The scanning period was 60 minutes, consisting of 26 time frames of progressively increasing durations. Each subject underwent two scans on separate days. High-resolution T1 MRI images were also obtained on all subjects for the purpose of anatomical localisation. These scans were transformed into stereotaxic space by first co-registering the summed PET radioactivity image to the MRI for each subject, and then using a linear transformation to transform the MRI image into standardised space (Collins et al., 1994).

The residuals method was then applied to the test-retest data to ensure that the method does not detect false positive differences when an appropriate statistical threshold is applied. There were no statistically significant differences in BP when comparing images from ten healthy subjects who underwent two test-retest scans with $[^{11}C]$SCH 23390, using the residuals method (Table 5.1). The threshold was t = 4.9 in the case of the test-retest $[^{11}C]$SCH 23390 data. The values differ between the measured and simulated data due to differences in the numbers of planes and time frames.

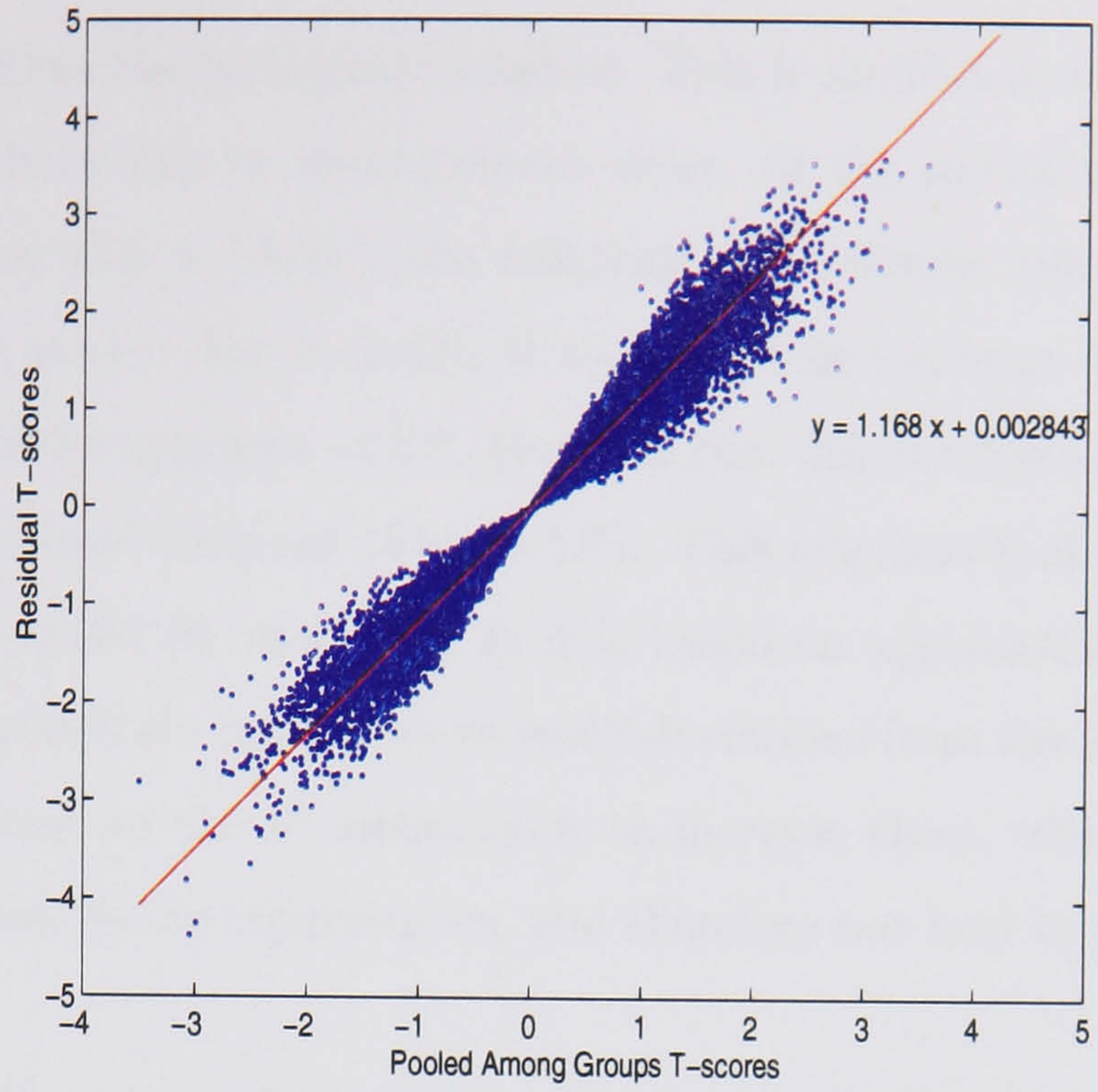


Figure 5.14: Voxel by voxel plot of t values obtained by the residuals method and by pooling over groups, for 12 simulated $[^{11}C]$SCH 23390 scans. The high correlation supports the assumptions made in the residual method.

5.5.3 Limitations

One could criticise the above simulations for the fact that inter-subject variability was not introduced in baseline BP, and that there was no attempt to simulate the effects of transformation to stereotaxic space. Both of these are potential sources of error. It is assumed that, while individuals may have different binding of the ligand at baseline, the change in BP with activation will be independent of baseline BP. A method for calculation of random effects is considered later in this thesis (see chapter 8). Spatial normalisation is a potential source of error in all studies that attempt to generate statistical maps from several individuals, however it was not our concern here to evaluate this problem. In any case the control data from human volunteers shows that these factors do not appear to produce false positives when the residuals method is applied (see Table 5.1).

The method makes the assumption of a noiseless input function or reference region, which limits its use to cases where there is a large reference area, or high-quality on-line blood sampling which essentially provide a noise-free input function. It may be possible to extend the residuals method to allow for noise in the input function using the approach of Huesman (Huesman, 1997).

Another potential problem in the method is the assumption that the compartmental

model perfectly describes the biological variables. This is implicit in the assumption that the residuals are entirely due to measurement error. If the model is not perfect (and in every practical case this is likely), the residuals also contain information about the goodness of fit of the model. For example, it was found that a large change in K1 could cause a small error in the estimate of BP. However this did not have an effect on the sd of the BP, which remained constant (Figure 5.7). This suggests that the method is not very sensitive to the model fit, and that, as it is based on approximations to the linear case, these approximations are insensitive to small deviations from the model. In any case, the effect of model error on the sd estimates is to increase them, which will lead to the resulting statistical tests being conservative, and therefore not lead to false positives.

5.6 Current Usage of the Methods and Future Ideas

These methods have been applied to neuroimaging studies involved in understanding the dopamine system with the tracers [^{11}C]raclopride (D2 receptor) and [^{11}C]SCH23390 (D1 receptor) in the several studies, independently of the work in thesis (Strafella et al., 2001; Dagher et al., 2001). This chapter has been rewritten as a paper and has been published (Aston et al., 2000) and cited by other several authors (Verhoeff, 2001; Hirvonen et al., 2001). Ongoing studies at the Montreal Neurological Institute are also making use of the methods developed here.

Nonlinear parameter estimation and associated variance techniques are continuously being updated, and novel ways of analysis discovered. Non-linear parameters tend to enter and affect systems in different ways to their linear counterparts. Whilst the methods here work both in theory and in practice, future methods may involve a fuller understanding of the nature of deviance or variance reduction when non-linear parameters are added to a model.

5.7 Summary

A new set of methods have been presented to facilitate parameter estimation in non-linear first-order tracer kinetic compartmental models. These methods utilise the full dynamic information of the data set in contrast to previous methods. It has been demonstrated that these methods allow for estimation of both the parameter and its associated error. The assumptions in the method have been formulated. These have been assessed for a

particular ligand, $[^{11}C]$SCH23390, and there is no indication that the validity of these assumptions are overly sensitive to the choice of ligand. The methods have also been assessed as to their sensitivity using simulated data, and assessed using test-retest data to check for false positives. The methods have already been used in clinical studies and helped to draw conclusions about clinical questions. Whilst, the application of these methods here has concentrated on the simplified reference tissue model, the methods are general and in theory applicable to all linear compartmental systems.

Chapter 6

Bayesian Spectral Analysis

In the previous chapter, temporal modelling with an a-priori chosen compartmental modelling structure was discussed. However, with a-priori modelling, a model structure needs to be chosen, and selection of an inappropriate model can cause bias in the estimated parameters. With voxel by voxel analysis, different voxels may be better analysed with differing models. In these cases it would be advantageous to allow the data to determine the model structure itself. In PET modelling there have been different attempts for solution of this problem, and it is still the subject of much ongoing research (Gunn et al., 2001b). One method currently in use for studies with plasma input functions is PET Spectral Analysis (Cunningham and Jones, 1993). Spectral Analysis fits an overcomplete basis to the data subject to non-negativity constraints on the basis functions. This is essentially a model selection procedure from a wide variety of PET compartmental structures (Schmidt, 1999) and allows estimation of parameters such as V_D and K_I. Non-negative least squares (NNLS) is a standard way to estimate the parameters, but does not have an analogous method to estimate the variance. This is due to the fact that the role of noise in the analysis is not well understood.

This chapter details methods using bayesian statistics to calculate distributions of parameters which are subject to non-negativity constraints. These methods are developed from bayesian theory (Geweke, 1996) and applied to PET Spectral Analysis. This is compared with current methods of estimating the distribution of spectral analysis in a non-parametric sense. These methods are applied to ROI data sets due to the computational nature of the algorithms.

6.1 PET Spectral Analysis - $SA_{Classic}$

PET Spectral Analysis (Cunningham and Jones, 1993) is a form of compartmental modelling analysis that requires no a-priori specification of the model. It is a basis function technique based again on first-order tracer kinetics, utilising a linear model with constrained maximum likelihood estimation. It requires a plasma input function to retain the non-negative constraints (Gunn et al., 2001b) and although the compartmental structures that can be modelled are restricted, in practice most models of interest are considered (Schmidt, 1999). The technique allows the data to be expressed in the following way

$$C_T(t) = \sum_{i=1}^{n} \alpha_i e^{-\beta_i t} \otimes C_P(t) \tag{6.1}$$

$$\text{s.t. } \alpha_i \geq 0 \tag{6.2}$$

where the tissue time-activity curve $C_T(t)$ is modelled as a convolution ($\otimes$) of the measured plasma/blood input function $C_P(t)$ with a sum of n exponential terms, the β_i's are usually predefined as a spectrum of logarithmically spaced values (an equiangular distribution of the basis vectors can alternatively be used (Cunningham et al., 1998)) between very rapid kinetics eg blood volume components and the slowest possible kinetics which corresponds to irreversible trapping of the tracer.

A unique solution is found by minimising the sum of squares fit to the data, subject to the conditions that the α_i are non-negative. This condition results from the assumption of first order time-invariant kinetics (Cunningham and Jones, 1993) and also ensures a unique solution, under mild assumptions (Gunn, 1996), for an over determined system of equations (Lawson and Hanson, 1974). Here, n is set to a large number, far greater than the number of data points available, and as such the problem is not uniquely determined by an unconstrained solution i.e it is ill-posed. This problem is solved using the NNLS algorithm (Lawson and Hanson, 1974), which provides the maximum likelihood solution subject to the constraints. In practice, most α_i are set to zero, and the number that are non-zero give a representation of the number of compartments in the underlying compartmental structure.

Parameters, such as the ones defined in the previous chapter, or others can then be defined in terms of the estimated solution to the problem. For example, K_I, the irreversible uptake constant, or V_D, the volume of distribution, can be defined, in terms of α_i and β_i as follows:

$$K_1 = \sum_{i=1}^{n} \alpha_i \tag{6.3}$$

$$K_I = \alpha_n \tag{6.4}$$

$$V_D = \sum_{i=1}^{n} \frac{\alpha_i}{\beta_i} \tag{6.5}$$

However, as the number of basis functions in the solution is large, traditional least squares methods of analysis cannot be used to determine the variance on the solution or on the parameters themselves. Even if this was not the case, the literature on constrained least squares estimates and their variance is limited, and empirical methods need to be employed in complex models such as Spectral Analysis.

6.1.1 PET Spectral Analysis Bootstrapped Error Estimation - SA_{Boot}

Previously, Turkheimer et al (1998) proposed a solution to the problem of error estimation given the constraints on the model. This work has involved the use of the bootstrap, a non-parametric empirical method. The method uses the residuals to the NNLS fit, and then bootstraps these residuals, using the appropriate weights for the assumed variance, to generate further data sets, that are then fitted using $SA_{Classic}$. Bootstrapping involves random sampling with replacement of the residuals to generate new data sets. This has been shown to well approximate the true distribution of the data (Efron and Tibshirani, 1993). This leads to estimates of the parameters empirical distribution regardless of how many basis functions are used, i.e. over or under parameterised cases. It makes no assumptions about the distribution of the noise on the residuals from the model. The algorithm is given in Appendix A.2.

The estimation procedure however is time consuming as separate randomizations need to be drawn for each voxel in the data set. Depending on how accurately the distribution is needed to be quantified, many bootstrap estimates may be needed, especially when the extremities of the distribution must be found accurately. This requires its use on ROI data in practical examples, rather than at the voxel level.

6.2 Bayesian Data Analysis

Bayesian Analysis is an alternative branch of Statistics which uses a differing philosophy to traditional classical analysis. In Bayesian methods, analysis takes the form of finding

posterior distributions of the parameters which are functions of the likelihood of the data, and the prior distribution of the estimates. This is neatly expressed in the form of Bayes Law which is the fundamental basis for all Bayesian analysis

$$\begin{aligned} p(\theta|y) &\propto l(y|\theta)p(\theta) \qquad (6.6) \\ \text{“posterior”} &\propto \text{“likelihood”} \times \text{“prior”} \end{aligned}$$

This states that the posterior probability of the parameters given the data is proportional to the likelihood of the parameters given the data multiplied by the prior probability of the parameters. This effectively means that the final distribution of the parameters is dependent on both the previous knowledge or prediction of the parameter distribution, and the data that arose. The essential difference between classical and bayesian approaches to data analysis, is that in classical analysis only the data is assumed to be random, and the parameters to be estimated are truly fixed, whilst in bayesian analysis both the data and the parameter are assumed to have a joint distribution. In the long run both of these will give rise to similar distributions for the parameters, as the prior distribution on the parameters becomes less and less important, but in small sample cases the results can be markedly different depending on the prior distribution.

The posterior distribution can rarely be calculated analytically in the case of complex data sets and prior distributions, so empirical methods are needed to estimate the posterior distribution (see 6.2.1). Bayesian inference can then be performed using the the posterior density estimates.

6.2.1 Gibbs Sampler

The Gibbs Sampler is a numerical algorithm which provides estimates of the posterior distribution of a parameter or a set of parameters, using updated estimates based on the current state of the parameters and a random component. It is useful when the conditional distribution of a parameter conditional on the values of all other parameters is known. Thus a distribution can be built up in the following way:

Gibbs Sampler (Geman and Geman, 1984; Bernardo and Smith, 1994)

If we require $p(\theta|y)$, and if $p(\theta_i|y, \theta_j(j \neq i))$ for all k parameters is known

then the following iterative procedure is used

$$\begin{aligned}
&\text{draw } \theta_1^{(1)} \text{ from } p(\theta_1|y, \theta_2^{(0)}, \ldots, \theta_k^{(0)}) \\
&\text{draw } \theta_2^{(1)} \text{ from } p(\theta_2|y, \theta_1^{(1)}, \theta_3^{(0)}, \ldots, \theta_k^{(0)}) \\
&\text{draw } \theta_3^{(1)} \text{ from } p(\theta_3|y, \theta_1^{(1)}, \theta_2^{(1)}, \theta_4^{(0)}, \ldots, \theta_k^{(0)}) \\
&\vdots \\
&\text{draw } \theta_2^{(1)} \text{ from } p(\theta_k|y, \theta_1^{(1)}, \ldots, \theta_{k-1}^{(1)}) \\
&\text{draw } \theta_1^{(2)} \text{ from } p(\theta_1|y, \theta_2^{(1)}, \ldots, \theta_k^{(1)}) \\
&\vdots
\end{aligned} \tag{6.7}$$

and so on

This algorithm has been shown to converge in distribution to the distribution of $p(\theta|x)$ (Bernardo and Smith, 1994). It is also known to be especially suitable in the cases where it is desired to make inferences about arbitrary functions of the parameters $\theta_1, \ldots, \theta_k$, (Bernardo and Smith, 1994), which is required for analysis of biological parameters such as V_D or K_I.

6.3 Bayesian Spectral Analysis - SA_{Bayes}

SA_{Bayes} is a method of estimating the distribution of the underlying parameters through the use of the Gibbs Sampler and constraints that allow the parameters to be constrained within the viable range.

6.3.1 Constrained Analysis

Equality and inequality constrained analysis is often very difficult to consider in a classical statistical sense (Judge and Takayama, 1966). Although attempts have been made to consider it in this way, for multiple variables in well-defined problems, it becomes overly complicated. Little progress has been made in the case of ill-posed problems where the constraints allow the problem to be solved.

Bayesian methods are ideally suited for the consideration of constraints due to the ability to define the posterior probability distributions in terms of the prior and through the use of sampling based methods to estimate these distributions. Inference is often classified into two areas; inference about the constraints themselves, and inference about the parameters subject to the constraints. In the case of PET data, the constraints are

known to hold from biological theory, and hence the main concentration here is on the second form of inference, on the parameters themselves.

Geweke (1996) has developed algorithms to calculate these posterior distributions subject to the constraints using the Gibbs Sampler (see 6.2.1). These algorithms can be subject to any contraints, but only non-negative constraints will be considered here.

This summary of the algorithm is given by Geweke (1996) .

Non-Negative Constrained Normal Gibbs Sampler (Geweke, 1996).

If the data is described by the linear model $y = X\beta + \epsilon$ and $\beta \geq 0$ then, if T is the degrees of freedom, and b is the ordinary least squares estimate, for a diffuse or flat prior

$$\begin{aligned} \{(y - X\beta)'(y - X\beta)/\sigma^2\} \,|\beta &\sim \chi^2(T) \\ \{\beta - b\} \,|\sigma &\sim N(0, \sigma^2 X'X) \text{ s.t. } 0 \leq \beta \end{aligned} \tag{6.8}$$

Let $z = \beta - b$. Then $z_j|(\sigma^2, z_i)$ is distributed truncated normal.

These algorithms allow assessment of the distribution in this framework (Figure 6.1). As can be seen, there is a need for positive degrees of freedom. Hence traditional Spectral Analysis cannot be used as the number of basis functions need to be less than the number of data points. Assessment of the importance of the number of basis functions is needed to determine as to whether this condition can be relaxed to allow the above algorithms to be used.

6.4 Simulation Studies

Simulated data were used to test the validity of SA_{Bayes} , and to compare it to $SA_{Classic}$ and SA_{Boot} . The simulated data included four PET tracers for neuroreceptor ligand or metabolism studies, used to assess the performance of the different methods. The radiotracers considered were $[^{11}C]$Raclopride (RAC) which is a tracer for the dopamine D_2 receptor, $[^{11}C]$Flumazenil (FMZ) a tracer for the benzodiazepine receptor, $[^{11}C]$Diprenorphine (DIP) a tracer for opiate receptors, and $[^{18}F]$FDG a tracer for the glucose metabolic rate. The compartmental models which were used to generate the data are shown in Figure 6.2.

The simulated data sets were generated by solving the compartmental model differential equations using the Runge-Kutta method implemented in Matlab (The Mathworks, Natick, MA.). Standard values for the rate constants were used for each tracer and are

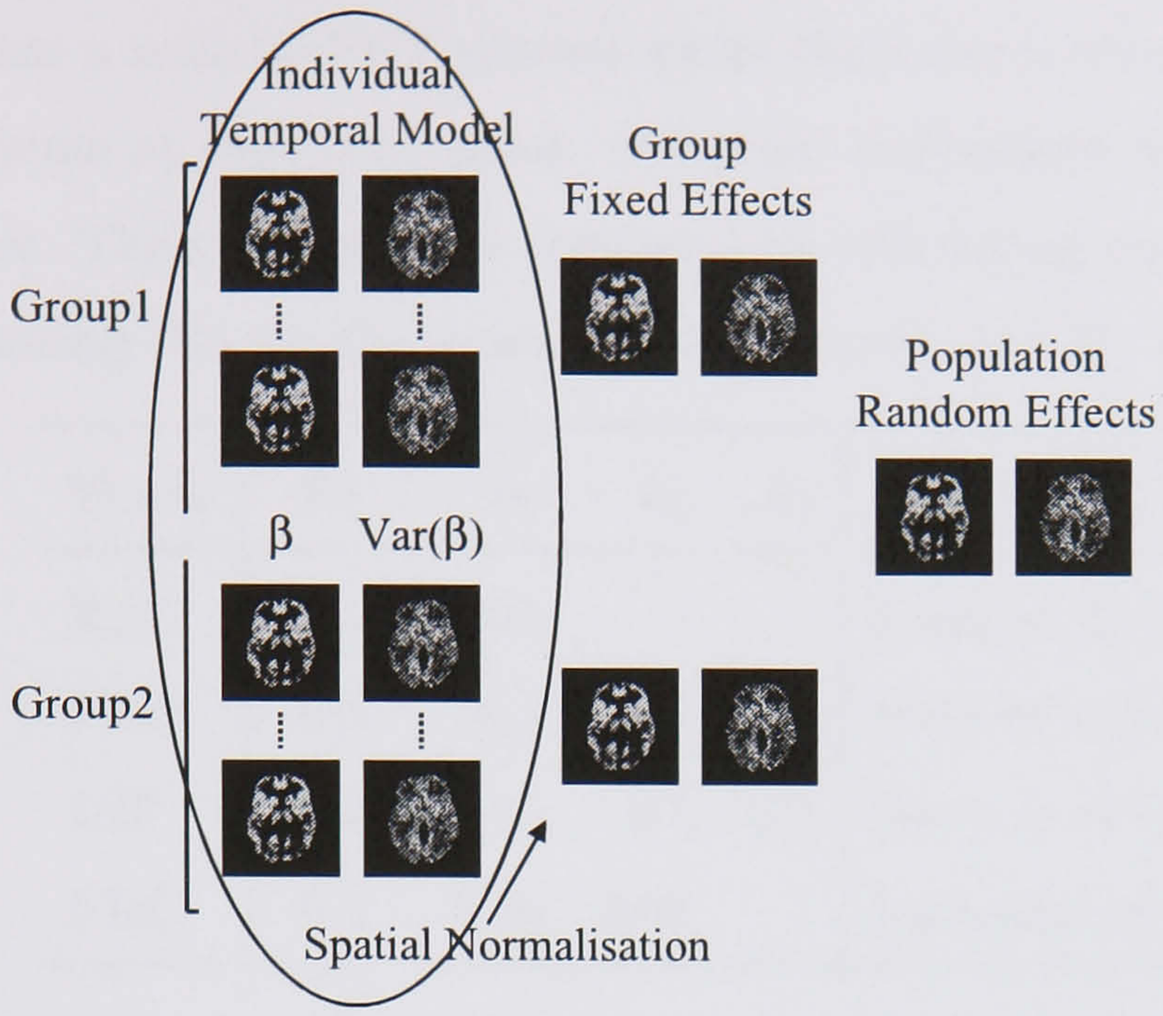
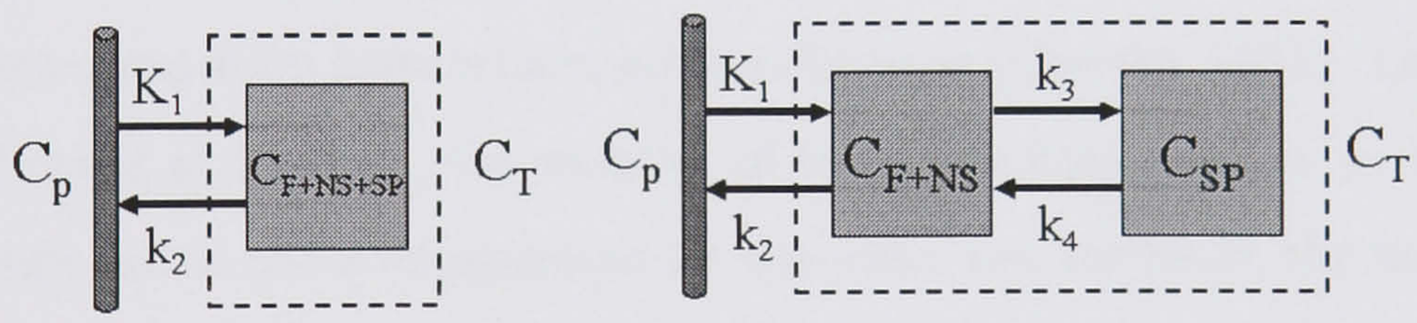
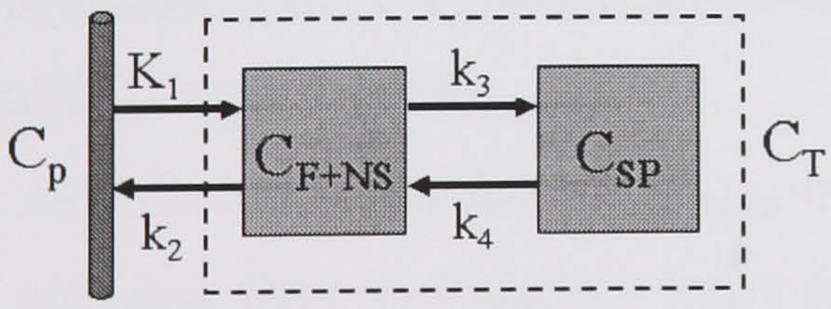


Figure 6.1: Subject Level Estimation and Inference

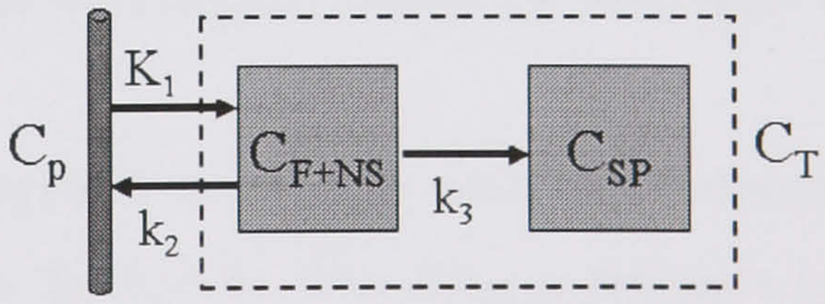


(a) ^{11}C-Raclopride

(b) ^{11}C-Flumazenil



(c) ^{11}C-Diprenorphine



(d) ^{18}F-FDG

Figure 6.2: Compartmental model structures for simulated data sets. Dotted boxes indicate simulated PET data.

given in Table 6.1. Normally distributed random noise was added to each data point in proportion (20 %) to the number of counts at that data point in the perfect model. This was to simulate a realistic PET process where the noise is assumed to be related to the number of counts at each data point. 500 noisy realisations with noise were generated for each tracer. The methods were compared by calculating various different parameters of interest, namely V_D for the neuroreceptor ligands, and K_I in the case of FDG. The

Tracer	K_1	k_2	k_3	k_4	Reference
RAC	0.15	0.075	-	-	Farde et al (1989)
FMZ	0.3	0.3	2.0	0.3	Price et al (1993)
DIP	0.3	0.15	0.5	0.1	Jones et al (1994)
FDG	0.1	0.16	0.04	-	Lucignani et al (1993)

Table 6.1: Rate constants used for the simulated tracer data sets (units are $ml_{plasma}(ml_{tissue})^{-1}min^{-1}$ for K_1 and min^{-1} for k_2, k_3 and k_4)

methods were implemented in Matlab, based on existing routines by Cunningham and Gunn ($SA_{Classic}$) and Turkheimer (SA_{Boot}). SA_{Bayes} was implemented using the Numerical Algorithms Group random number generation software, and the algorithms for random number generation from truncated distributions (Geweke, 1991). Due to the need for positive degrees of freedom, the number of basis functions was set to 10 in SA_{Bayes} but even though this is not a requirement for the other two methods, the number of basis function was also set to 10, to allow comparisons between the methods.

Table 6.2 presents the summary for the 4 tracer simulations. The three methods produced similar results. However, all methods were slightly biased ($< 8\%$), with the bias being slightly bigger in SA_{Bayes} .

The variance estimates from SA_{Bayes} compared well to the estimates obtained using SA_{Boot} although they were slightly larger (see Table 6.2). The SA_{Boot} estimate has been shown to produce a good approximation to the underlying variance of the Spectral Analysis estimates (Turkheimer et al., 1998).

In the case of FDG, SA_{Bayes} gave an excellent approximation to its own variance, which suggests that it could be used to look at studies where there is expected to be a change in the system between two experiments, while in the other cases for reversible radioligand binding, SA_{Bayes} was worse than the SA_{Boot} approximation, although the

Tracer	Parameter	RAC V_D	FMZ V_D	DIP V_D	FDG K_I
True Value	Mean	2.00	7.67	12.0	0.0200
$SA_{Classic}$	Mean	2.04	7.87	15.7	0.0196
SA_{Boot}	Mean	2.06	8.01	16.1	0.0197
SA_{Bayes}	Mean	2.14	8.31	16.5	0.0193
$SA_{Classic}$	sd	0.0302	0.177	0.465	4.73E-04
SA_{Boot}	sd	0.0518	0.303	0.555	3.11E-04
SA_{Bayes}	sd	0.0749	0.378	0.595	4.06E-04
SA_{Bayes}	Mean(sd)	0.0361	0.181	0.494	4.04E-04

Table 6.2: Summary of results for the 4 PET tracer simulations. The mean values are shown for the different tracers, and the standard deviations across the simulations are also shown. The mean estimated standard deviation from the SA_{Bayes} Method is also shown.

difference was small.

The results of the simulations to determine how the number of components in the basis affects the final solution revealed a limitation of SA_{Bayes} . Whilst it works for most compartmental systems, there are a class of systems, here represented by the $[^{11}C]$Diprenorphine (DIP) case, that are inadequately modelled by all three approaches without a substantial number of basis functions ($\sim$ 100). This problem might be addressed by changing the way the data is collected to obtain more data points, to allow SA_{Bayes} to be used with a greater n or to choose a different set of β's to define the basis. The problem results from the slowly reversible kinetics of the system. This is difficult to estimate precisely unless there are a sufficient number of components near the irreversible end of the spectrum. Changing the number of components (n) from 100 to 10 in the three other cases produced both unbiased and small (2% std) differences in the values of either V_D or K_I, whereas this became 26% biased $\pm$ 7% with DIP (there was a 31% bias with 10 basis functions while with 100 basis functions this bias is reduced to less than 4% from the true value).

$SA_{Classic}$ is currently used on an ROI or voxel-by-voxel level ($\sim 10^6$ voxels in a image volume) whilst SA_{Boot} is currently only used on an ROI level, although voxel-by-voxel implementation has been assessed, due to the time required to generate each estimate. It was hoped that SA_{Bayes} would be able to be used for voxel analysis, as only the mean and variance parameters are required. The convergence criteria for the new method was assessed empirically. This was done to assess the number of iterations needed to accurately estimate both the parameters of interest and their underlying distributions to the order of the second moment. The process requires initial starting values which may or may not be

close to the final solution, and therefore takes some iterations to settle down and remove the bias of the initial guesses from the solution. The first 3000 iterations were discarded (burn-off). The Gibbs Sampler also produces correlated estimates and by looking at a plot of autocorrelation for different lags, it was determined that at lag=100 the autocorrelation had died away (see Figure 6.3). However, due to the large computational time of each estimate, it was hoped that far fewer iterations could achieve acceptable results. Using a measured FDG curve, the possibility of using only every tenth iteration and producing 1000 10-iteration (10000 iterations in total) estimates was assessed. The mean value of such an approximation was very close (≤ 0.11 % difference) as was the calculated value of the standard deviation (≤ 0.65 % ± 5 % difference). The data set used to assess the differences was the same data with 2000 100-iteration (200000 iterations in total) estimates. Using the real data, the change in the standard deviation estimates was assessed as the number of iterations was increased. It was found that after approximately 9000 (including the burn off) iterations ($\sim$ 4 mins on a SGI O2), the standard deviation had stabilised. The method was also tested for the stability of the mean over repeated sampling and found to be very stable, with only a 1 % std on the mean value of the estimated parameter. This

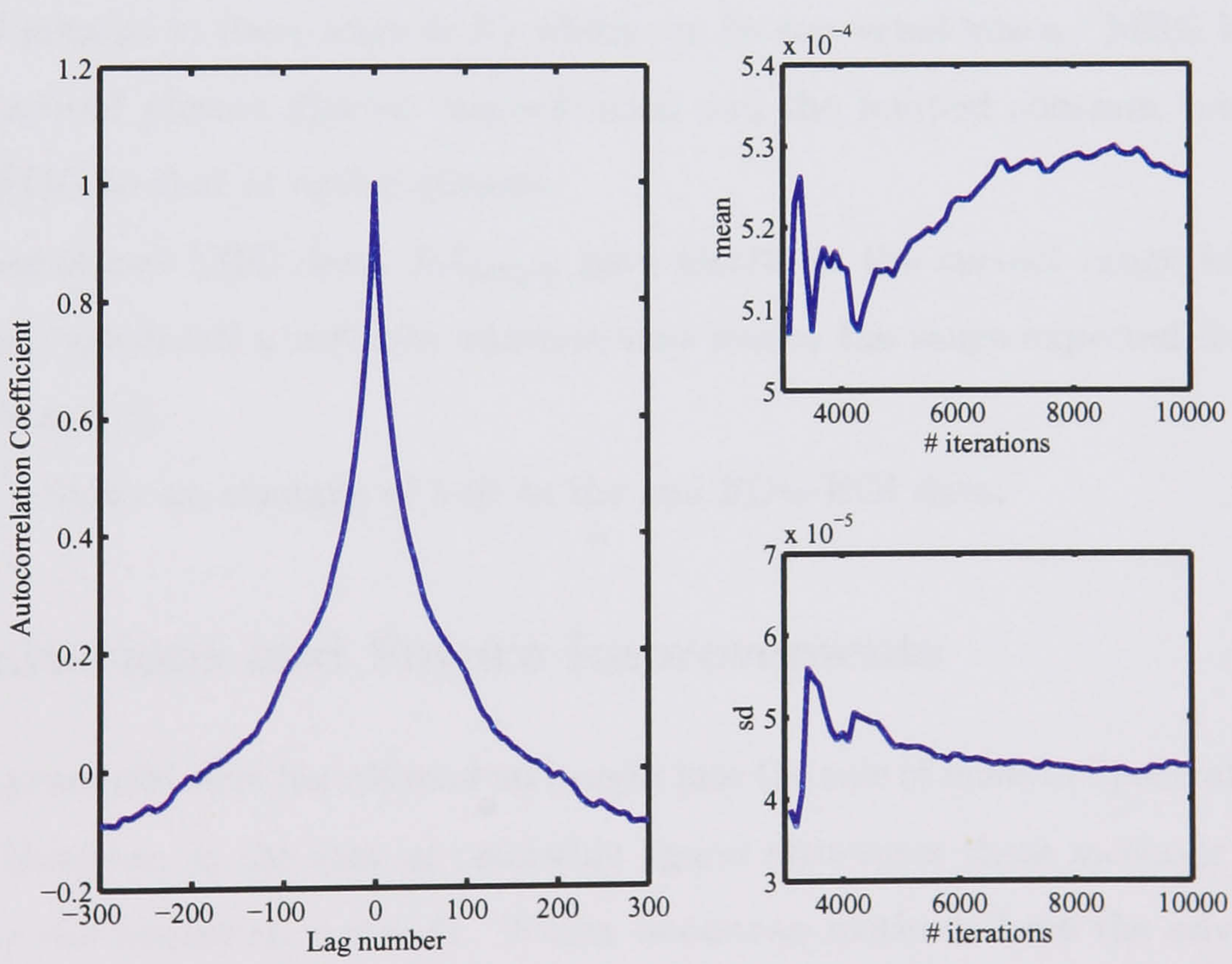


Figure 6.3: Convergence and Stability of Estimates of Mean and Std

is likely to imply that the method can also only be used on ROI data, due to the number of iterations required to get stable estimates of the mean and variance.

Tracer Algorithm	FDG Region	K_I	$sd(K_I)$
$SA_{Classic}$	ROI	0.0271	
$SA_{Classic}$	Voxel	0.0289	9.4E-03
SA_{Boot}	ROI	0.0305	3.8E-03
SA_{Bayes}	ROI	0.0309	3.14E-03

Table 6.3: Summary of results for the real FDG data

6.5 FDG Cortical Studies

Data was also taken from a measured FDG scan of a normal volunteer in an ongoing clinical study. This data was analysed on an ROI basis for both SA_{Boot} and SA_{Bayes} , and then compared to the parametric image analysis derived from $SA_{Classic}$. Regions in the cortex were defined, and the SA_{Boot} and SA_{Bayes} K_I parameter values from the average ROI curve were compared to the K_I parameter values calculated by applying the same ROI to the $SA_{Classic}$ parametric images. The estimates of the variance were then computed for the three methods either directly for SA_{Boot} and SA_{Bayes} or indirectly by assessing the variance within the ROI defined on the parametric image for $SA_{Classic}$. The parameter of interest in these scans is K_I which can be converted into a CMRG by scaling with the measured plasma glucose concentration and the lumped constant relating the behavior of FDG to that of native glucose.

For the measured FDG data, SA_{Bayes} gave results in the correct range for the K_I parameter, and produced a variance estimate that was in the range expected for an ROI curve (see Table 6.3).

Figure 6.4 shows an example of a fit to the real FDG ROI data.

6.6 Limitations and Future Improvements

The method presented here has allowed an insight into the role of noise in Spectral Analysis estimation. However, in the case of reversible ligand structures these methods were out performed by the bootstrap methods. Whilst bootstrap methods have the advantage of being non-parametric in structure, they have the disadvantage of requiring a large number of bootstrap estimates to find accurate estimates of the extremities of the distribution.

However, there may be ways to improve the estimates that come from the bayes method. As it is likely that not all components enter the solution, it may be possible to estimate prior probability distributions onto the basis functions as to whether or not

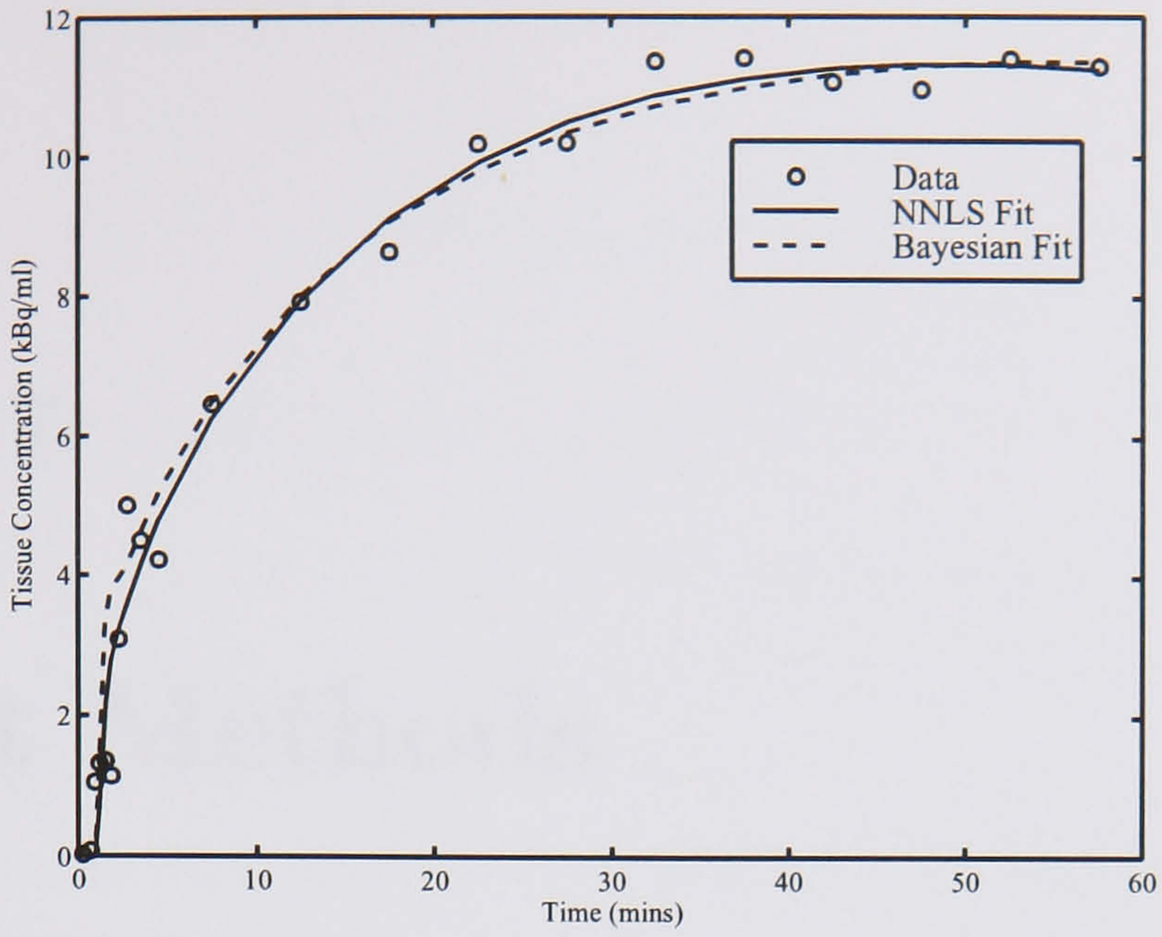


Figure 6.4: NNLS ($SA_{Classic}$; SA_{Boot}) and Bayesian (SA_{Bayes}) fits to the real FDG PET data

they enter the solution. This would ideally be estimated from previous studies using the same radioligand in the same subject type (patient / normal) and can the be used to constrain the basis functions entering the solution to be of a more realistic distribution. At present all basis functions enter the solution due to the noise in the data, but the use of a more sophisticated prior may allow this to change. It may also be necessary to use alternative sampling techniques where the dependence of the basis functions on one other becomes more complex. This is a possible idea for future investigation.

6.7 Summary

PET Spectral Analysis is a routinely used technique to investigate PET data sets. This chapter has investigated the noise properties of the estimates achieved though a form of reduced basis Spectral Analysis. This was achieved using bayesian techniques, with prior assumptions about the parameters associated with the basis functions. Estimates and errors on these estimates were found to give good approximations to real estimates, especially in the case of irreversible ligands such as FDG. Previously little was known about the noise structure of Spectral Analysis, or how noise influenced the estimates achieved by Spectral Analysis. Procedures to estimate noise distributions of the parameters have been developed, and have allowed further insight into the role of noise in Spectral Analysis.

Chapter 7

Wavelet Methods

A recent development in Signal Processing has been the introduction of wavelet methods (Daubechies, 1992). These methods can be traced back over a long history, from ideas as far back as fourier methods, but it is only recently that the methods from several disciplines, including engineering and mathematics, have been shown to be formally equivalent, and in so doing have sparked great interest in their use.

Wavelet methods are primarily a tool for signal estimation. This should be emphasised, as generally in neuroimaging and especially in activation studies, methods are primarily designed for hypothesis testing. The neuroimaging community is currently involved in debate as to whether simple yes or no answers are any longer the most useful questions that can be asked, or whether quantitative questions are now not only relevant to ask, but practical to answer (Turkheimer et al., 2002b). Wavelets are one method that are allowing these discussions to be debated if not resolved.

This chapter provides an overview of wavelet methods as they can be applied to neuroimaging data sets. Wavelets have many interesting properties that can be exploited from both statistical and image processing perspectives. Indeed there has already been much work done in neuroimaging using wavelet methods. The wavelet methods are generally split into two different types; spatial wavelet methods and temporal wavelet methods.

A formal expression for the variance of images from the variance of wavelet parameters will be constructed. This will allow equivalent analysis as is available in other linear analysis methods. Methods will also be developed here for fMRI data sets in a spatio-temporal sense. This will not involve spatio-temporal wavelets, as will be discussed later (see section 7.5), but rather spatial wavelet modelling followed by temporal linear modelling. These modelling paradigms have been rigorously developed for PET (Turkheimer

et al., 1999; Turkheimer et al., 2000a; Turkheimer et al., 2000b) and will here also be applied to fMRI data. fMRI has differing characteristics from PET both in terms of the data sets themselves and the modelling that is carried out on the data.

7.1 Spatial-Temporal Modelling

True, informed, spatio-temporal modelling could be seen as the holy grail for neuroimaging analysis. The data sets which are now derived in many modalities are of a full spatio-temporal nature, and as such, full use of the information available should involve a spatio-temporal component. It is expected that the brain itself is a spatio-temporal system, with components acting together in spatial relationships, in a temporal sequence. This can be surmised from the physical connections between brain regions in the form of neural pathways. True understanding of the brain can only be achieved with an understanding of these spatio-temporal systems. However, modelling of these billions of connections is not (yet) possible, and the data sets from current techniques not of sufficient quality in both spatial and temporal dimensions.

However, this does not mean that spatio-temporal modelling as a technique should be disregarded as impractical. In fact implicit spatio-temporal modelling has been and is continuously used in neuroimaging models. A simple example from PET is the use of ROI analysis. This can be considered as an anatomically informed spatial model (ROI definition and extraction of TACs for each ROI from the dynamic PET scan) followed by temporal modelling of these TACs, yielding spatio-temporal parameters. In fact any model that has both a spatial component and a temporal component can be considered as a spatio-temporal model, regardless of the complexities of these components.

7.2 Wavelets

Wavelet methods are transforms of the data from the original data basis to another more representative basis for the signal, in terms of number of components needed for representation.

In order to aid understanding of the following sections, an overview of wavelets is presented. There are many excellent texts now available on wavelets (Daubechies, 1992; Vidakovic, 1999), with much more detailed introductions to the field, from both statistical and non statistical points of view.

7.2.1 Wavelet Transformations

In neuroimaging, data is collected spatially, temporally or in both dimensions simultaneously. A discrete wavelet transform takes the data from the domain it was collected in, to a wavelet domain through a linear transform of the data. Thus temporally collected data would be transformed from the time domain to a wavelet domain. In practice, the wavelet transformations of the data are usually discrete wavelet transforms, as the data is of a discrete as opposed to a continuous nature. This is analogous to the use of fourier series for discrete data, as opposed to fourier integrals for continuous functions. Wavelets themselves possess many useful properties which make transformation into the wavelet domain of use. As with fourier series, wavelets are basis functions which span function spaces, and for certain classes of signal, certain wavelets provide sparse representations of these signals. This is a similar principle to that of fourier series where the signal is successively modelled using basis functions of higher frequencies. However, these transformations have a singular advantage over fourier methods. Fourier methods are not able to account for non-stationary signals, as the signal is assumed to be modelled by periodic functions. The wavelets are, by definition locally defined, both in time and space, and as such can model non-stationarity. This is of major importance in neuroimaging as the signals are usually if not always non-stationary.

Wavelets can be described in a variety of ways. Here it will be convenient to use the linear matrix description or the quadrature mirror filter expressions for wavelets. These filters can be seen as high pass (h) and low pass (g) filters and are more directly implementable for large signals than matrix multipliers. This is due to matrices becoming large at the rate of n^2 as a signal increases in length (n). The filters are applied using the cascade algorithm (Vidakovic, 1999) where if

$$(Ha)_k = \sum_n h_{n-2k} a_n \tag{7.1}$$

$$(Ga)_k = \sum_n g_{n-2k} a_n \tag{7.2}$$

then

$$y_W = (H^k y, GH^{k-1} y, \ldots, GHy, Gy) \tag{7.3}$$

where $1 \leq k \leq J$ where the length of y is 2^J.

Wavelet transforms are often orthogonal transformations of the data, ie transformations that are a rotation of the data, and preserve the energy (squared distance from the

origin) of the data (Vidakovic, 1999). There are many different 'families' of wavelets. Perhaps the most simple of these is the Haar family of wavelets

$$W_{\text{Haar}} = \begin{bmatrix} \frac{1}{2\sqrt{2}} & \frac{1}{2\sqrt{2}} & \frac{1}{2} & 0 & \frac{1}{\sqrt{2}} & 0 & 0 & 0 \\ \frac{1}{2\sqrt{2}} & \frac{1}{2\sqrt{2}} & \frac{1}{2} & 0 & -\frac{1}{\sqrt{2}} & 0 & 0 & 0 \\ \frac{1}{2\sqrt{2}} & \frac{1}{2\sqrt{2}} & -\frac{1}{2} & 0 & 0 & \frac{1}{\sqrt{2}} & 0 & 0 \\ \frac{1}{2\sqrt{2}} & \frac{1}{2\sqrt{2}} & -\frac{1}{2} & 0 & 0 & -\frac{1}{\sqrt{2}} & 0 & 0 \\ \frac{1}{2\sqrt{2}} & -\frac{1}{2\sqrt{2}} & 0 & \frac{1}{2} & 0 & 0 & \frac{1}{\sqrt{2}} & 0 \\ \frac{1}{2\sqrt{2}} & -\frac{1}{2\sqrt{2}} & 0 & \frac{1}{2} & 0 & 0 & -\frac{1}{\sqrt{2}} & 0 \\ \frac{1}{2\sqrt{2}} & -\frac{1}{2\sqrt{2}} & 0 & -\frac{1}{2} & 0 & 0 & 0 & \frac{1}{\sqrt{2}} \\ \frac{1}{2\sqrt{2}} & -\frac{1}{2\sqrt{2}} & 0 & -\frac{1}{2} & 0 & 0 & 0 & -\frac{1}{\sqrt{2}} \end{bmatrix} \tag{7.4}$$

which are essentially normalised averaging functions for different portions of the signal. Equation 7.4 gives the signal decomposition for the Haar wavelet transform of an 8 data point signal with equivalent filters

$$h = \{\frac{1}{\sqrt{2}}, \frac{1}{\sqrt{2}}\} \tag{7.5}$$

$$g = \{\frac{1}{\sqrt{2}}, -\frac{1}{\sqrt{2}}\} \tag{7.6}$$

The highest level averages (1st Column) the whole signal, whilst the lower levels average portions of the signal. The energy of the signal is preserved by the normalisation of the energy of each wavelet.

1-D Wavelets

In the one dimensional case, this process can be repeated for any signal length of 2^n by a shifting and dilation of the signal from the highest to the lowest levels. Depending on the properties of the original signal, a particular family of wavelets may better represent the signal. For example the Haar wavelet might be a good choice for block structured signals, but is unlikely to well represent smooth signals.

A simple one dimensional example of a wavelet transform is shown in Figure 7.1. The data set from Figure 4.1 (a) is used, and an example of it's wavelet transformation using the Battle-Lemarie wavelet basis (see 7.2.3) is given. The wavelets are all normalised to have power one, and as such it can be seen that the wavelet basis represents the signal in a small number of wavelet coefficients whilst the rest are essentially zero.

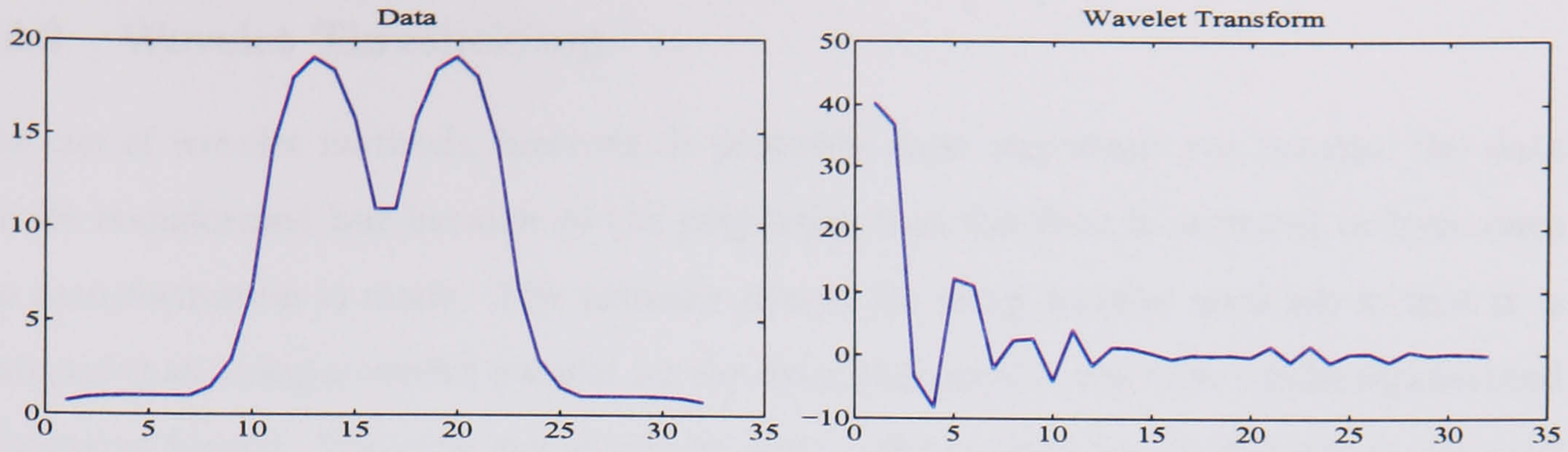


Figure 7.1: 1-D Signal and wavelet transform

Multidimensional Wavelets

In higher dimensions the wavelets are applied in a very similar fashion to the spatial smoothing involved in the Partial Volume Correction (see chapter 4). The transformation is firstly applied to one dimension of the data, and then to the next and so forth. This allows easy multidimensional analysis of the data. Again a simple example, here using the Shepp-Logan phantom, a tomographic phantom and the Battle-Lemarie wavelet basis is shown in Figure 7.2 .

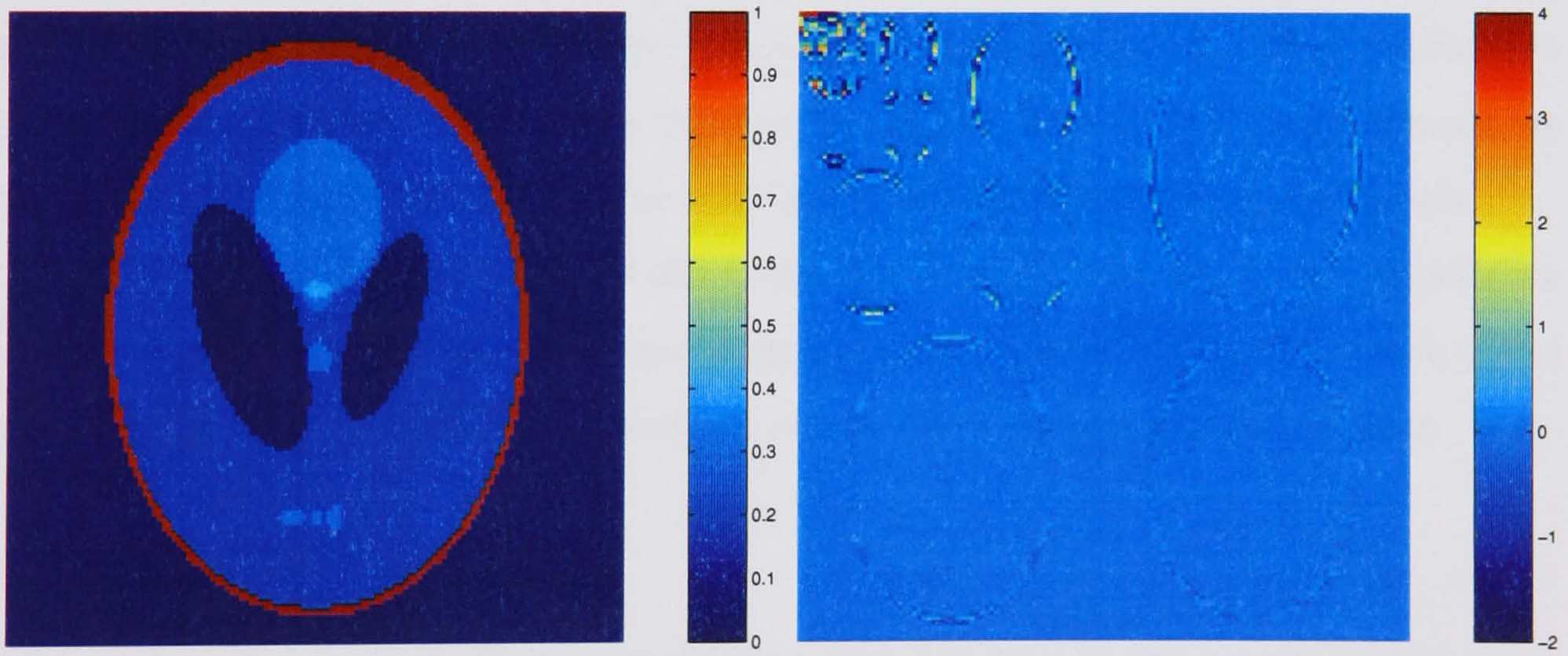


Figure 7.2: Tomographic 2-D Example Signal and Battle-Lemarie wavelet transform

As can be seen the wavelet transform is essentially a high and low pass filter of the data and a combination of the two in each level. The data is reduced in size each time using this analogy and then refiltered again at the new level. This can be seen in the way the data is 'repeated' in each quadrant.

7.2.2 Wavelet Thresholding

The use of wavelet methods, however, is probably most important not because the data can be transformed but because of the properties that the data is assumed to have once the transformation is made. The primary reason for using wavelet methods is that it is assumed that, using a correct wavelet for the data, the signal in the data can be represented in a sparse format. Thus the signal is only contained in a very few coefficients as opposed to the large number in the data set. This is useful in many different applications such as image compression and communications, but here its most important use will be in signal denoising.

Neuroimaging data sets are experimental data sets and as such subject to noise. If the data is well approximated by a small number of wavelet coefficients, and if the noise is independent across the signal, then as the wavelets are orthogonal, the noise will be spread throughout the components in the basis. For coloured or correlated noise, the transform of the noise is approximately uncorrelated within levels, by careful choice of wavelet. Thus by removing the components which only contain noise, i.e. thresholding, it is possible to denoise the signal from the data. Thresholding itself can be performed in any domain, but in the image domain, this would result in the loss of information at any voxel thresholded completely. In the wavelet domain, the thresholding of wavelet coefficients does not necessarily lead to complete thresholding of any voxel in the image domain, as any one voxel is represented by a linear combination of multiple wavelet coefficients.

There are many different methods of wavelet thresholding, and this is still the subject of much ongoing research. However depending on the application and the structure of the signal in the wavelet domain, some methods will be more appropriate than others.

Hard and Soft Thresholding

There are two types of non-linear thresholding that are used in most cases (other types do exist and are often combinations of these two cases), soft and hard thresholding. Hard thresholding is when a wavelet coefficient is either subject to a test which results in 'keep or kill', ie the wavelet coefficient is either set to zero or kept as it is. Soft thresholding is similar in that some wavelet coefficients are 'killed' whilst others are shrunk back towards zero. This is due to the properties of shrinkage estimators, which have been shown to be better estimators, in terms of mean squared error, of multivariate normal means than simple averages. The two types of threshold can be formulated mathematically as follows.

If w is a wavelet coefficient, and λ is the threshold value then

$$\begin{aligned} \text{Hard} \quad T(w,\lambda) &= w \cdot \mathbf{I}(|w| \geq \lambda) \\ \text{Soft} \quad T(w,\lambda) &= (w - \text{sgn}(w)\lambda) \cdot \mathbf{I}(|w| \geq \lambda) \end{aligned} \tag{7.7}$$

.

The thresholds themselves can be set either as thresholds across the entire data set or thresholds set level by level. Indeed if the noise structure of the data is correlated then a level by level approach thresholding has been shown to be better in terms of minimax estimation (Johnstone and Silverman, 1997).

Universal Threshold

The two types of thresholding above both depend on choosing a suitable value of λ. One of the first thresholds proposed was that of the Universal Threshold (Donoho and Johnstone, 1994). This provides a simple and easy to calculate threshold directly from the data. The derivation of the estimator comes from standard normal theory and results in the following value of λ,

$$\lambda_U = \sqrt{2 \log n}\hat{\sigma} \tag{7.8}$$

There are several possible ways to estimate $\hat{\sigma}$ of which two are the following (Vidakovic and Muller, 1999; Turkheimer et al., 1999). If K represents the set of indices of the lowest level wavelets (ie the ones which are most likely to contain noise as opposed to signal) then the $|K|$ is $N/2$ where N is the length of the signal. Then

$$\begin{aligned} \text{(i)} \quad \hat{\sigma}^2 &= 1/(N/2-1)\textstyle\sum_{k\in K}(w_k - \bar{w}_{(k\in K)}) \quad \text{(Vidakovic and Muller, 1999)} \\ \text{(ii)} \quad \hat{\sigma}^2 &= \text{MAD}(w_k | k \in K)/0.6745 \qquad\qquad \text{(Turkheimer et al., 1999)} \end{aligned} \tag{7.9}$$

where 0.6745 standardises the value for the normal distribution.

The universal threshold is useful as it is easy to calculate. However when the number of coefficients is large, or $\hat{\sigma}$ is over-estimated, the model tends to be underfit, ie the threshold is too high (Vidakovic and Muller, 1999).

SUREShrink

There is an alternative to the universal threshold that has been developed to be unbiased. The universal threshold is designed to minimise the probability of including noise in the reconstruction of the signal, but this will occur at the expense of removing part of the

signal. Donoho and Johnstone (1995) derived a threshold which would be unbiased with respect to the minimisation of the mean squared error.

$$\text{SURE}(w,\lambda) = N - 2\sum_{i=1}^{N}(\mathbf{I}(|w_i| < \lambda) + \sum_{i=1}^{N}(|w_i| \wedge \lambda) \tag{7.10}$$

where

$$(|w_i| \wedge \lambda) = \begin{cases} \lambda & \text{if } |w_i| \leq \lambda \\ |w_i| & \text{if } |w_i| > \lambda \end{cases} \tag{7.11}$$

The threshold is then chosen from the above such that

$$\lambda_{\text{SURE}} = \min_{0 \leq \lambda \leq \lambda_U}(\text{SURE}(w,\lambda)) \tag{7.12}$$

The SURE threshold is very efficient but not well suited to situations where the signal is very sparse. In this case the threshold (SUREShrink) can be chosen as the Universal threshold. A test (Vidakovic, 1999) is given by

$$\lambda_{\text{SUREShrink}} = \begin{cases} \lambda_{\text{SURE}} & \text{if } (\log_2(N^{3/2})N^{-1/2}) < (N^{-1}\sum_{i=1}^{N}(w_i^2 - 1)) \\ \lambda_U & \text{otherwise} \end{cases} \tag{7.13}$$

7.2.3 Wavelets Bases

Wavelets must be chosen carefully so that the wavelet basis chosen has good functional support for the type of data that is to be modelled using them. Different applications have different bases. The Haar basis is an good 'educational' basis for its simplicity but unlikely to be a good representational basis for smooth functions (Vidakovic, 1999). There are too numerous a choice of bases to list here, but the one chosen here represents a base which may have functional support in neuroimaging, and have been previously considered or used for neuroimaging applications.

Battle-Lemarie Wavelets

A wavelet used for neuroimaging by multiple authors (Ruttimann et al., 1998; Turkheimer et al., 1999) is that of the Battle-Lemarie wavelet, or orthogonal cubic-spline wavelet. This was chosen by Ruttimann for the following reasons;

Orthogonality is desirable for the subsequent statistical analysis

The basis is symmetric

Splines are able to reduce spectral overlap between resolutions. This will result in good decorrelation of the data.



(a) High Pass Filter (b) Low Pass Filter (c) W Matrix

Figure 7.3: Battle-Lemarie Wavelet Basis Quadrature Filters.

The high and low pass filters, along with the matrix transform are given in Figure 7.3.

Other wavelet bases that have been used for neuroimaging include Daubechies wavelets (Raz and Turetsky, 1999), but as the Battle-Lemarie has been shown to have good functional support for both fMRI (Ruttimann et al., 1998) and PET (Turkheimer et al., 1999), it was preferred to other bases.

7.2.4 Variance Estimation

An extension of the wavelet denoising procedures above is the calculation of variance maps of the resulting parameters in image space. Whilst the calculation of the parameters is straightforward through the use of the inverse transform, the calculation of variance components from the variance of the wavelet components is a more complicated problem especially in large multi-dimensional data sets.

The wavelet transform (and indeed inverse transform) can be seen as a similar operation to the smoothing operation of the partial volume techniques (chapter 4 Section 4.4.1). In the case of partial volume the transformed variance components were not calculated and hence a back transform was not needed, but in the case of wavelets the variance is calculated in the transformed space, and hence a variance transform to image space is required. Whilst PVC was a linear transform which could easily be expressed in terms of its transform in each direction, due to the decimated process of the wavelet transform, it is a little more difficult to directly express the linear transform, although it is indeed linear, and can be expressed in terms of $k \times d$ matrices where k is the number of decimation levels, and d is the dimension size of the data, unless $d = 1$ when this can be described in terms of a single matrix.

If W is the wavelet transform, β the parameters, then

$$\begin{aligned} \text{Param} \quad \beta_I &= W^{-1}(\beta_W) \\ \text{Variance} \quad \text{Var}(\beta_I) &= \text{Var}(W^{-1}(\beta_W)) \\ &= (W^{-1})\text{Var}(\beta_W)(W^{-1})' \end{aligned} \tag{7.14}$$

with the dimension of β equal to $mnp \times 1$ where m, n and p are the size of three original image dimensions. This allows estimation of the variance components from one space to the other, theoretically. It should be noted that W as a linear transform has dimensions of $mnp \times mnp$ when formulated in this way, and as such direct calculation of the above equation is impractical for measured data.

There are, however, certain assumptions and simplifications that can be made to the above equations which render calculation feasible. It should first be noted that traditionally neuroimaging is only concerned with pointwise voxel variance estimation and that covariance information between voxels is usually not explicitly calculated. Thus the number of terms to be calculated in the above equation is now reduced to the square root of the original (mnp calculations), as the portion of the variance matrix of interest is the leading diagonal. Secondly, one of the properties that originally made wavelet analysis appealing, was the assumption that the noise in the data was decorrelated by the wavelet transform. This would lead the covariance structure of β_W to be diagonal in nature. This greatly eases the computational burden of calculation of matrix products.

As has been noted, the structure of the wavelet transform is that of the tensor structure seen before (except now with levels of decimation), and as such can be written in a similar form

$$W = (W_{x_1} \otimes W_{y_1} \otimes W_{z_1}) \oplus (W_{x_2} \otimes W_{y_2} \otimes W_{z_2}) \oplus \ldots \oplus (W_{x_k} \otimes W_{y_k} \otimes W_{z_k}) \tag{7.15}$$

where $\otimes$ is the kronecker product of the individual 1-D wavelet transforms (in matrix form) in each dimension, and $\oplus$ the decimation operation.

However, it has been shown for the wavelet transform (and hence the inverse transform) that the 1-D wavelet transform of $\text{diag}(WDW')$ where D is a diagonal matrix is given by the square of the components of W multiplied by the diagonal elements of D (Nowak and Baraniuk, 1999). This is also the case for the 3-D wavelet transform, we consider that if

$$W_{1\text{D}} = ((W_{x_1} \otimes W_{y_1} \otimes W_{z_1}) \oplus (W_{x_2} \otimes W_{y_2} \otimes W_{z_2}) \oplus \ldots \oplus (W_{x_k} \otimes W_{y_k} \otimes W_{z_k})) \tag{7.16}$$

where $\otimes$ indicates a tensor operation, and if D is a three dimensional array, with D_{v} the

equivalent vectorisation of D, then

$$\Lambda(W\Lambda(D_{\mathrm{v}})W) = W_{1\mathrm{D}}^{[2]} D_{1\mathrm{D}} \tag{7.17}$$

$$= \left((W_{x_1}^{[2]} \otimes W_{y_1}^{[2]} \otimes W_{z_1}^{[2]}) \oplus \ldots \oplus (W_{x_k}^{[2]} \otimes W_{y_k}^{[2]} \otimes W_{z_k}^{[2]})\right) \circ D \tag{7.18}$$

where $W^{[2]} = \{w_{ij}^2\}$ and Λ is the diagonal operator converting a vector into a diagonal matrix or taking the diagonal vector of a matrix.

However for the inverse transform, the inverse decimation operator cannot be represented by a matrix multiplication for multidimensional data. This is due to the decimation step, where the decimation level is used in the level above, whereas in the wavelet transform the decimation of the data does not utilise data from the level below except data involved in that step.

However, the decimation can be expressed as a linear transform, just not in the tensor algorithm notation used above. This means that the variance of the parameter in image space at voxel co-ordinate (i, j, m) is given by

$$\begin{aligned}\mathrm{Var}(\beta_{ijk}) = {} & ((\{IW_{x_1}\}_i \otimes \{IW_{y_1}\}_j \otimes \{IW_{z_1}\}_m) \oplus \ldots \oplus (\{IW_{x_k}\}_i \otimes \{IW_{y_k}\}_j \otimes \{IW_{z_k}\}_m) \odot S)' \\ & ((\{IW_{x_1}\}_i \otimes \{IW_{y_1}\}_j \otimes \{IW_{z_1}\}_m) \oplus \ldots \oplus (\{IW_{x_k}\}_i \otimes \{IW_{y_k}\}_j \otimes \{IW_{z_k}\}_m) \odot S)\end{aligned} \tag{7.19}$$

where S is the standard deviation at each point in wavelet space, $\{IW\}_m$ is the m row of IW and $\odot$ the Khatri-Row product (Appendix A.1). This formulation also allows the calculation of the covariance between any two points

$$\begin{aligned}C_{ijmnpq} = {} & ((\{IW_{x_1}\}_i \otimes \{IW_{y_1}\}_j \otimes \{IW_{z_1}\}_m) \oplus \ldots \oplus (\{IW_{x_k}\}_i \otimes \{IW_{y_k}\}_j \otimes \{IW_{z_k}\}_m) \odot S)' \\ & ((\{IW_{x_1}\}_n \otimes \{IW_{y_1}\}_p \otimes \{IW_{z_1}\}_q) \oplus \ldots \oplus (\{IW_{x_k}\}_n \otimes \{IW_{y_k}\}_p \otimes \{IW_{z_k}\}_q) \odot S)\end{aligned} \tag{7.20}$$

where $C_{ijmnpq} = \mathrm{Cov}(\beta_{ijm}, \beta_{npq})$.

The calculation of the linear inverse transform for a voxel in image space is as follows: Calculate the inverse transform for a one level transformation for the entire data set. This can be expressed in a tensor form, but then reassessed for the ijmth voxel. Then calculate the one level transformation for the subset of the data set that would be included in a 2-level transform, and apply this, in a tensor way, to the ijmth voxel transformation. Repeat this until the kth level is reached, and this is the transform for the ijm voxel for the entire process. This can then be used in the calculation of the variance component in Eqn 7.19.

These transforms will be especially useful in the case of linear threshold estimators (Turkheimer et al., 2002a). In the case of non-linear estimators, the variance estimates will be more difficult to calculate, although this does not necessarily exclude calculation.

7.3 Wavelet Denoising in Neuroimaging

There have previously been studies in which wavelets have been used to denoise neuroimaging data sets. This can be seen as a subject level estimation or inference problem in the inference hierarchy (Figure 7.4). The first methods to use wavelets (Ruttimann

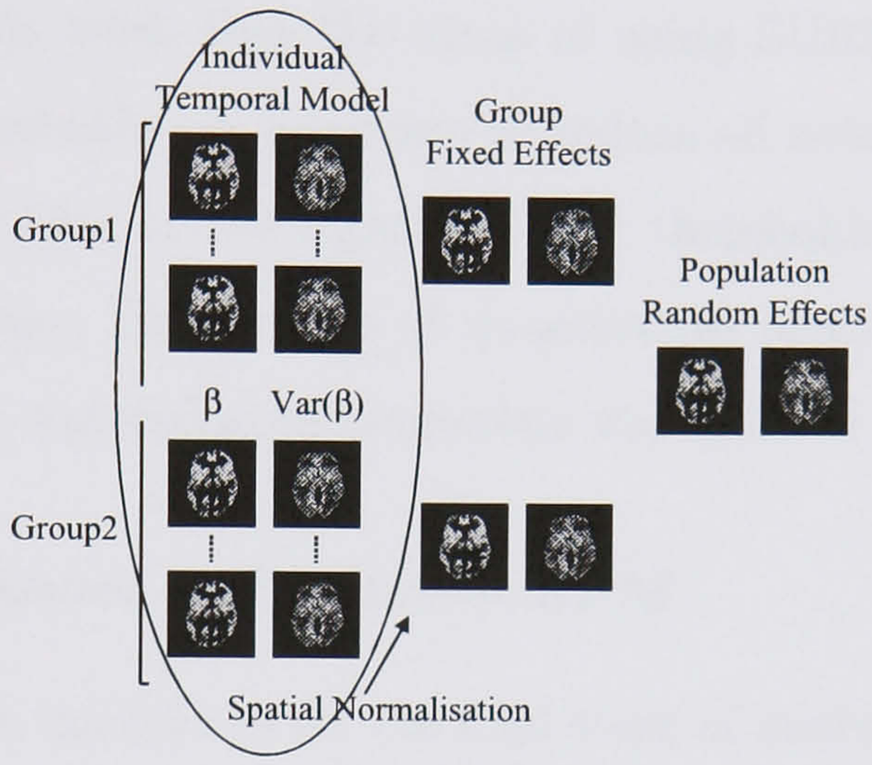


Figure 7.4: Subject Level Estimation

et al., 1994; Turkheimer et al., 1999) were to spatially model the signal using wavelets and then to denoise this spatial model to reconstruct signal images. It was shown that Battle-Lemarie wavelets (Ruttimann et al., 1994) provided a good functional base for PET images, and it was later shown that this also can be extended to fMRI images (Ruttimann et al., 1998).

Spatial denoising took the form of transforming the images into the spatial domain, and then using local variance estimates from the wavelet coefficients themselves to set thresholds to reconstruct the data (Turkheimer et al., 1999).

7.3.1 PET Wavelet Kinetic Modelling

Turkheimer and Aston (Turkheimer et al., 2000a) suggested that there was a superior approach to the estimation of variance for the wavelet coefficients based on the fourth dimension of the data set, the temporal dimension. If point-wise wavelet variance could be calculated from the temporal properties of the data, then this variance estimate could

be used to threshold each wavelet coefficient. It was shown that this was indeed possible depending on the type of temporal model used.

It was deemed important that the model parameters be reproducible in either wavelet or image space, and that only the thresholding would yield a difference in the recovered signal. This requirement limited the temporal models that can be used to linear models which would be commutative across the spatial domain. Linear models are additive with respect to the parameters derived from the data, whilst non-linear models are most often non-commutative. However linear models are available for temporally transformed PET data (Patlak et al., 1983; Logan et al., 1990).

It was also in this work that the ideas of using SURE thresholds were introduced. Whilst universal thresholds can be shown to reduce all noise with a fixed probability, this is at the expense of bias in the signal. SURE thresholds reduce this bias, whilst still eliminating some noise. In the case of quantitative analysis, the SURE threshold and minimising the mean squared error properties was deemed to be more useful.

7.3.2 Wavelet Anova and Wavelet SPM

Wavelet has also been considered for the final stage of analysis, the combination of images into group comparisons (Raz and Turetsky, 1999; Turkheimer et al., 2000b). Here wavelets are used to model the parametric images and then used to calculate different contrasts across these parameters. This is an equivalent analysis to SPM (Ashburner et al., 1999) except carried out in the wavelet domain as opposed to the image domain.

It has also been noted (Raz and Turetsky, 1999) that often SPM results are obtained by smoothing. This as Raz comments is "particularly inappropriate in fMRI research, because it reduces the good spatial resolution afforded by the method". Wavelets provide a method of denoising the data whilst retaining the resolution of the signal.

7.4 fMRI Spatio-Temporal Analysis

There has been little previous work on applying spatio-temporal models to fMRI analysis. There is however growing interest in these ideas, as it is understood that there is often more sensitive analysis available if local information is combined. Indeed there has been investigation into the use of fMRI in the wavelet domain, and a preliminary study carried out (Desco et al., 2001). This study looked at how different wavelet bases performed at different noise and signal levels. However, these studies tend to focus on ideal conditions

and as such further work is needed to evaluate methods using more complex analysis schemes with more realistic experimental noise conditions.

The following methods are performed using a current temporal model for fMRI (see 7.4.1), which takes into account the correlated temporal noise structure. The wavelet basis functions are evaluated using the different thresholding rules. This is firstly performed on simulated data, and the results obtained from the simulations used to guide the analysis of the measured fMRI data set.

7.4.1 fMRI Temporal Analysis

The temporal scheme that was used to analyse the wavelet coefficient is an autoregressive linear model, with estimated autoregressive parameters at each point. The original linear method has been proposed by Worsley (2002) and the scheme followed will be identical except for the use of wavelet coefficients instead of real data. The autocorrelation structure however will not be smoothed as in image data, as this would be inappropriate in a wavelet basis with no correlation between neighbouring wavelet coefficients.

The temporal model is summarised as follows

$$\begin{aligned} y &= X\beta + \epsilon_n \\ \epsilon_n &= \rho_1\epsilon_{n-1} + \rho_2\epsilon_{n-2} + \ldots + \rho_k\epsilon_{n-k} + \eta \end{aligned} \tag{7.21}$$

where η is white noise, ρ the autocorrelation parameters up to lag k, X the model, y the data, and β the parameters to estimate. Firstly the autocorrelation parameters are estimated (see Appendix A.3), and then these used to prewhiten the data. The linear model is then fitted and the β parameters estimated in wavelet space. This gives a set of parameters and their associated errors in wavelet space. Appropriate thresholding is then carried out, and the parameters maps transformed into image space along with the variance estimates.

The linear model itself is dependent on the data and the experiment but will typically also include a drift term to account for the intrinsic drift in the scanner. This can be modelled as a linear drift or a higher order polynomial. The signal will be modelled as a response convolved with a hemodynamic response function. This model used in the experiments below is given by the difference of two gamma functions (Friston et al., 1998) with the parameters determined by Glover (1999) .

7.4.2 Simulation Study

In order to evaluate the performance of the wavelet transforms under noise conditions with the same properties as the assumed noise conditions of the data, the following simulation was performed.

A noise-free signal image was generated, with a brain region, a small region where the signal was deemed present and the background (Figure 7.5). The signal was designed as

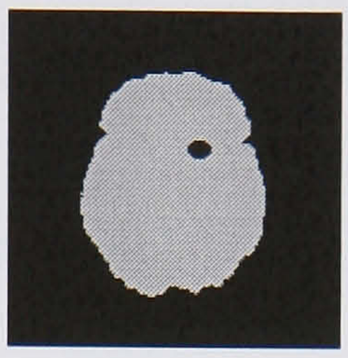
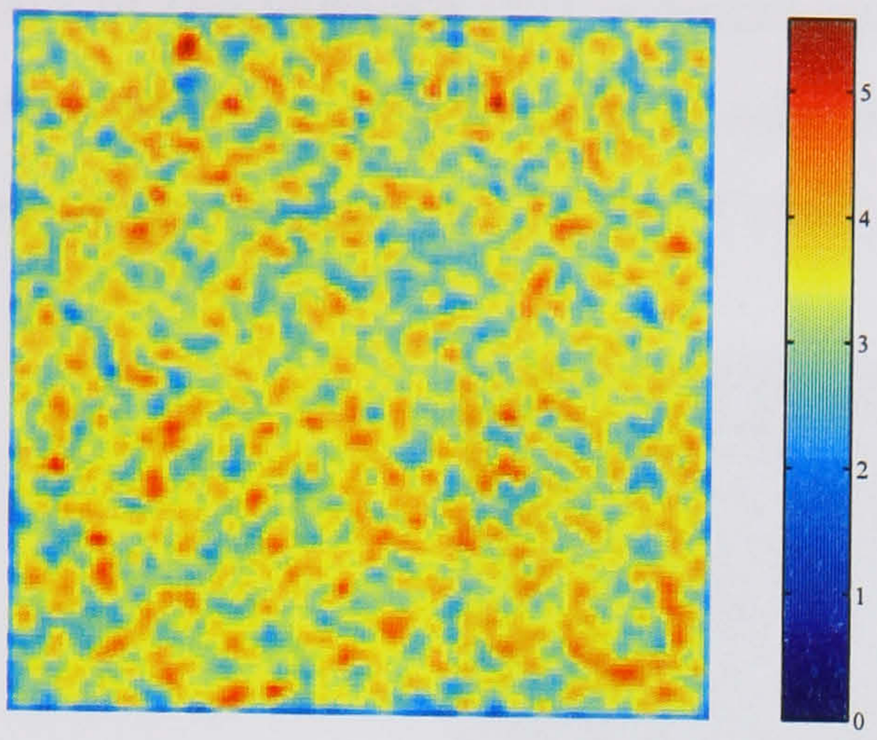


Figure 7.5: Simulation Template

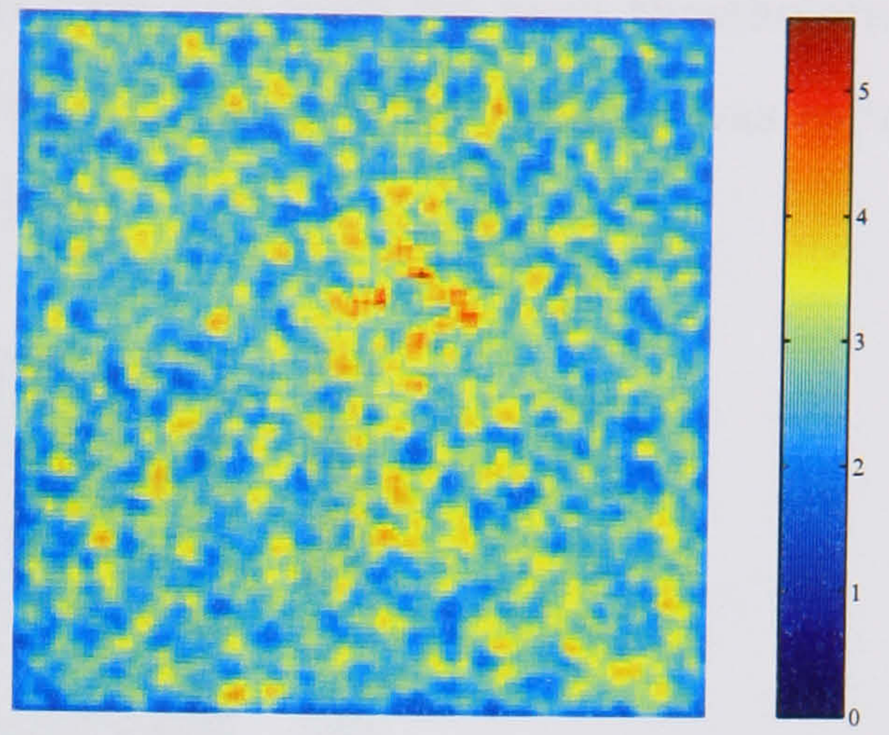
a block fMRI study using an activation / baseline design with 128 frames of data. The noise was set to be 20% of the signal strength and 100 realisations of the study were generated. The temporal noise structure was correlated with an AR(4) model, and the images were spatially smoothed with a covariance structure equivalent to a 6mm FHWM (approximately the same as an fMRI data set). The data sets were analysed using 4 different methods; Firstly, in image space with the linear model, secondly, in wavelet space with universal thresholding, thirdly in wavelet space with SURE soft thresholding, and finally in wavelet space with SURE hard thresholding. The mean squared error maps across the different realisations were then calculated for the differing methods. Both the maximum and mean MSE across the image were considered, as the signal needs to be estimated well both locally and globally if possible. A Variance map was also generated in the hard universal thresholding case.

Figure 7.6 shows the MSE images produced from the simulations. Table 7.1 gives descriptive values for the MSE. It shows that the MSE is minimised in the case of the SURE hard threshold for the combined maximum and mean, in the sense that although the maximum is not different from the image case, it is much better on average. The other thresholds minimise the error in the places where no signal is present (due to the high threshold values) but bias the signal so that the maximum MSE is very high in the areas of the signal, compared with the image space methods.

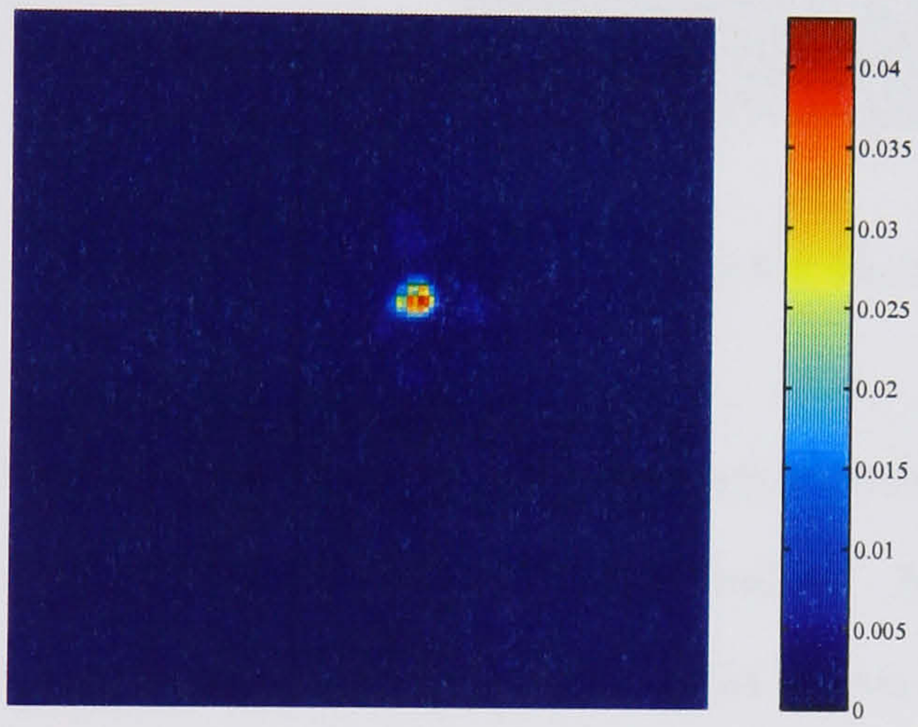
The measures of variance of the universal threshold also yielded results consistent with



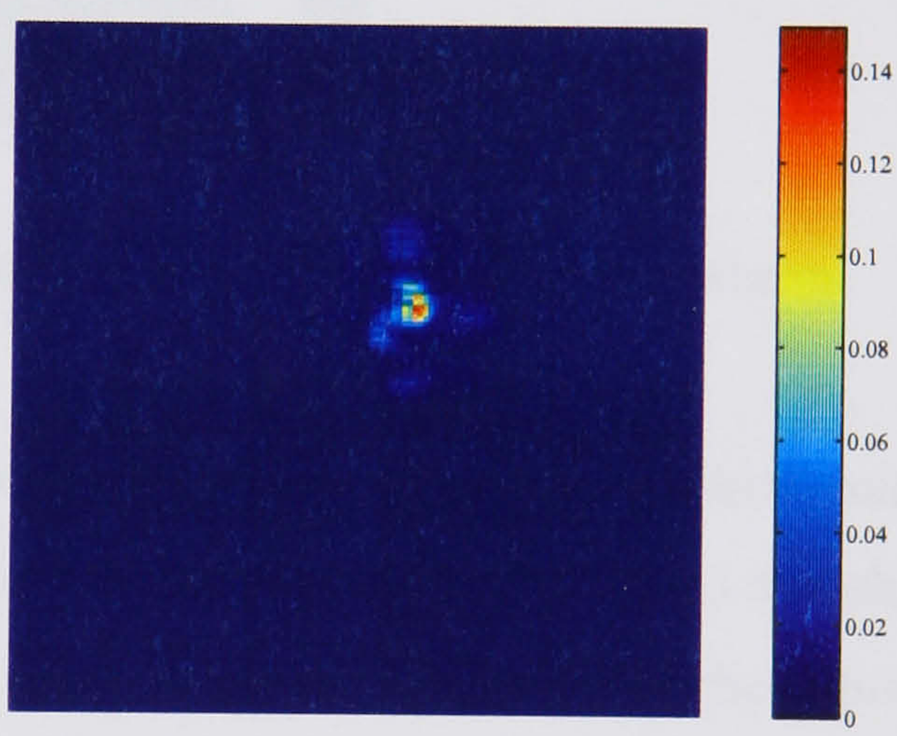
(a) MSE Image



(b) MSE Hard SURE



(c) MSE Soft SURE



(d) MSE Universal

Figure 7.6: MSE for different thresholding procedures.

Type	Bias Mean	Bias Max	Var Mean	Var Max	MSE Mean	MSE Max
Image	3.5e-005	0.000491	0.00335	0.00544	1	1.62
Hard Sure	5.16e-005	0.00226	0.00269	0.00442	0.818	1.66
Soft Sure	0.000114	0.0402	0.000682	0.00338	0.237	12.8
Hard Uni	0.00049	0.138	0.000217	0.0144	0.211	44.5

Table 7.1: MSE Mean and Max Values for Analysis Methods across the Image (MSE normalised to the Image)

those expected (Figure 7.7). The variance on the universal estimate was very low (or zero) outside the signal area, whilst being relatively high in the signal region itself. A crude estimate of the variance that is transformed back was used for hard thresholding. The estimates were assumed to contain only signal, and as such the variance was assumed to be that of the signal which survived thresholding.

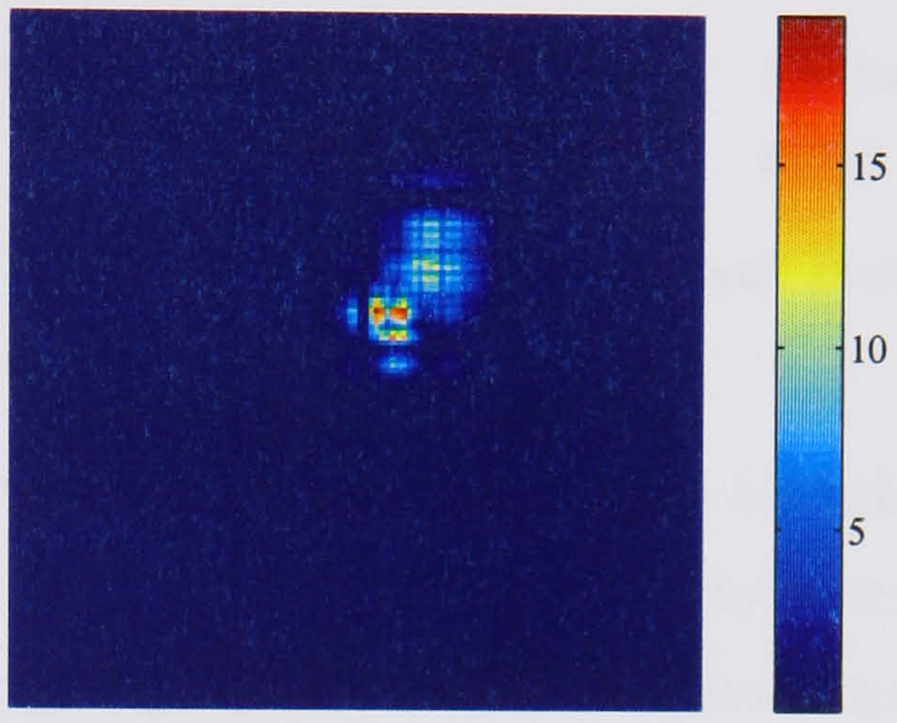


Figure 7.7: Variance Images for Hard Universal thresholding procedures.

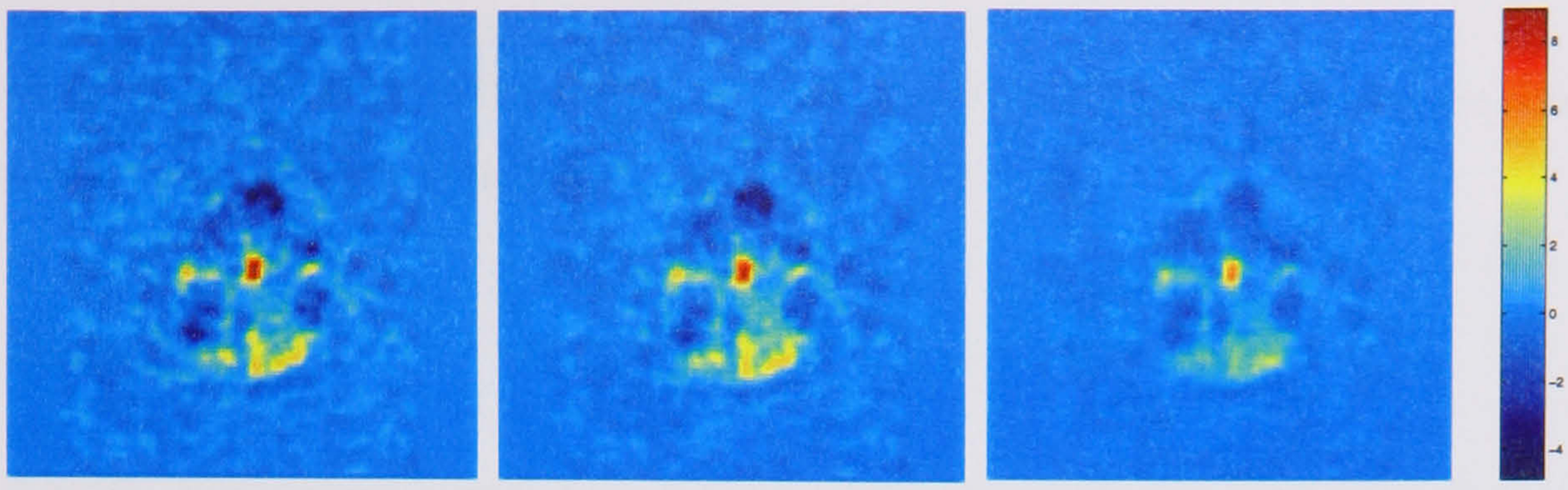
The main purpose of the simulation was to determine the methods which might be best applied to the measured data below. As a result the SURE with hard thresholding will be applied to the measured data in an effort to reduce the noise in the signal, but to also determine the best estimate of signal itself. The SURE soft threshold will also be calculated as it provides a method of reducing the noise across the image, at less expense than the universal threshold.

7.4.3 Measured Data

Measured data previously analysed (Worsley et al., 2002) in the image domain was also used to compare the methods. This analysis was carried out in 2-D due to the slice timing effects. Each slice was analysed separately and compared with the image space analysis.

The fMRI data set came from a study with a pain stimulus. A hot stimulus and warm stimulus were applied to the skin of a subject, with interleaved periods of rest. The contrast of interest was that of whether there was a difference between the regions that were activated with hot and warm, and a characterisation of the magnitude of the differences.

The results of the analysis are shown in Figure 7.8. The SURE hard threshold retains the pattern and magnitude of the differences and does reduce slightly the background



(a) Parameter Image (b) Parameter after Hard SURE (c) Parameter after Soft SURE

Figure 7.8: Estimation of Effect for Wavelet and Image based methods.

noise. The SURE soft threshold reduces the noise to a much greater extent, but at the expense of a reduction in the magnitude of the signal. However the spatial pattern remains.

These results show that dependent on what is required from the image, an appropriate image thresholding technique can be selected with the desired properties.

7.5 Future Work - Four Dimensional Wavelet Modelling

The methods of analysis used have incorporated a 4-D modelling structure, through the use of 2-D wavelets for each 1-D slice in the spatial domain, followed by a linear temporal model varying for each slice. A consideration of the use of four dimensional wavelets would be an interesting extension to this work. However, there are some considerations that need to be the taken into account before such modelling is undertaken. The data set itself, whilst being four dimensional, is not a repeated four dimensional object. The spatial dimensionals are intrinsically different to the temporal dimension, and a modelling procedure that works in the spatial dimension is unlikely to be appropriate in the temporal dimension and visa versa. It is more likely that a similar approach to the method undertaken here would be more appropriate, with a different wavelet modelling analysis in the temporal dimension than in the spatial. The spatial domain itself is of interest as the slice dimension has a temporal element as the slices are acquired at slightly different times. Interleaved protocols for acquisition can result in differences between neighbouring slices on the order of seconds.

Alternative spatial modelling methods could also be used if appropriate temporal methods can be found. These include complex wavelets (Kingsbury, 2001), which have the advantage of being translation invariant, such that the positioning of the signal is not

important. Translation invariant techniques are available without resorting to complex wavelets, but these are computationally very expensive.

7.6 Summary

In this chapter, methods of analysis for neuroimaging data using wavelet transforms have been reviewed and developed. Wavelets have previously been shown to enhance analysis of neuroimaging data sets through the use of more appropriate domains for analysis. A theoretical derivation of the variance of parameters in image space has been developed using the variance in the wavelet domain. The analysis methods have been applied to fMRI data using a linear model with correlated errors in the wavelet domain. This has been analysed with the differing methods and compared using simulated and measured data. These methods will facilitate analysis of neuroimaging data using the wavelet transform, and will allow image space variance estimates of the estimated parameters.

Chapter 8

Random Effects

No study of statistical techniques in neuroimaging would be complete without the inclusion of a discussion of random effects. These are the random components that need to be included in statistical models to allow generalisation to inferences about the population (Figure 8.1). Random Effects are the current 'in-vogue' issue in statistics of functional neuroimaging, and as such methods which address this problem need to be considered and developed (Friston et al., 1999). This chapter will discuss methods that are currently in use, and detail new developments that allow for more sophisticated analyses to account for random effects. These new techniques make greater use of information available in the data set. These methods have primarily been developed for use with fMRI, but here will be considered with respect to PET neuroreceptor ligand studies.

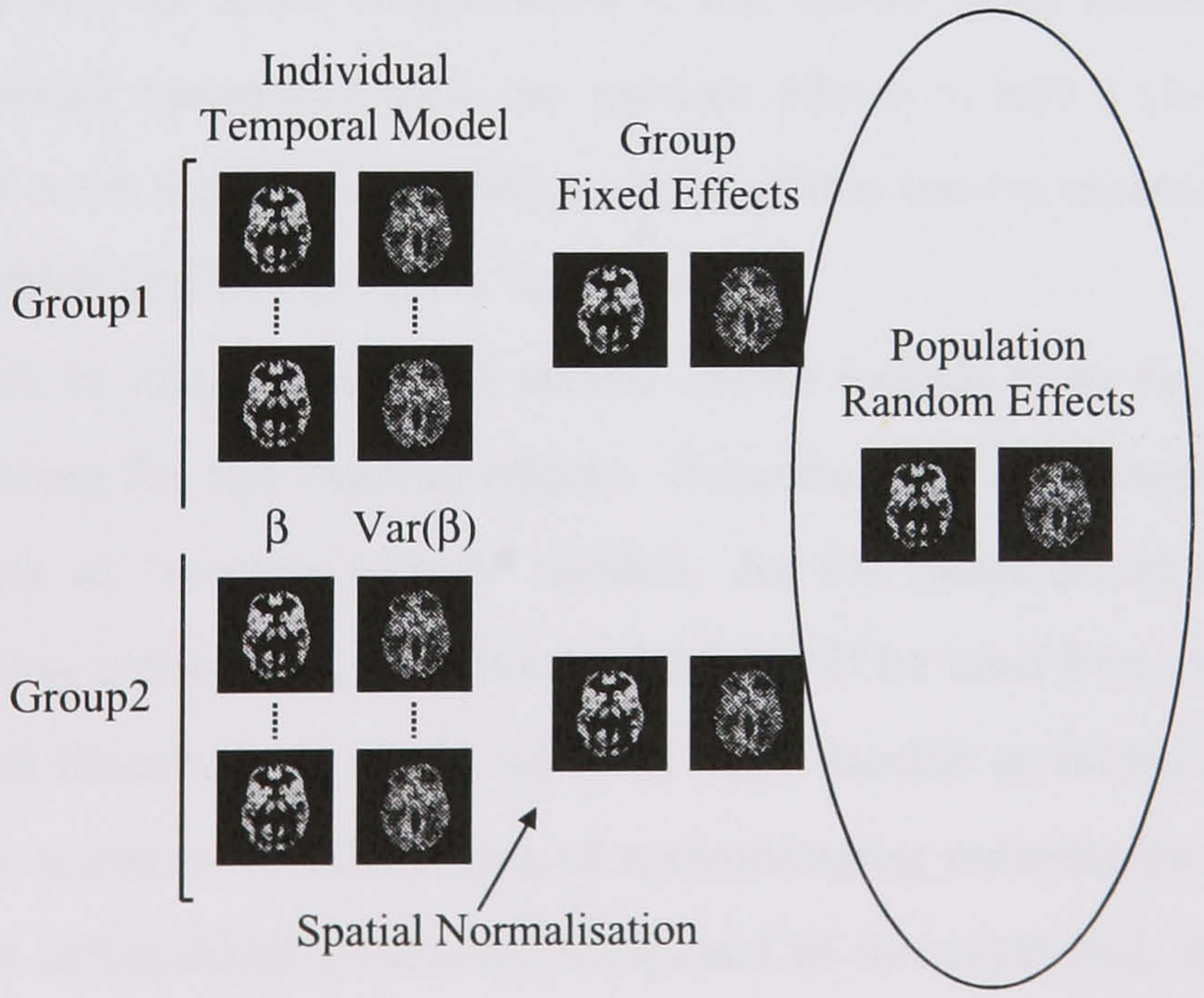


Figure 8.1: Population Level Inference

8.1 Random Effects Models

Random effects models are stochastic models which account for both fixed and random components in the data. Effects can be considered as the parameters associated with each linear component in the model. Fixed effects are those parameters associated with the model which are estimated from the data, but assumed to be fixed with respect to repetition of the experiment. An example of a fixed effect is the parameter associated with a covariate such as age where it is assumed the data is affected linearly by age, and the affect of age is the same across the population from which the data is drawn. Random effects are parameters that can change from repetition to repetition, but which come from some underlying distribution. A random effect for example could be the effect of measuring different subjects drawn from a population. The parameter of interest is not fixed for the population but changes from individual to individual according to some distribution in the population.

This can also be expressed in terms of a mixed effect model, a model which contains both fixed and random effects (Searle et al., 1992)

$$y = X\alpha + Z\gamma + \epsilon \tag{8.1}$$

where

$$\begin{aligned} E[\gamma] = 0 \quad \text{Var}[\gamma] = V \\ E[\epsilon] = 0 \quad \text{Var}[\epsilon] = \sigma^2 \end{aligned} \tag{8.2}$$

and where X are the fixed components in the model, with associated effects α, Z represents the model connected with the random effects γ, and ϵ the fixed effects error (or measurement error if preferred). The random effects have a variance matrix V associated with them, which can be known or unknown.

The object in neuroimaging of mixed effects models is to estimate the fixed effects whilst accounting for the random effects. Neuroimaging literature tends to label "mixed effects" models as "random effects" models. As the thesis is concerned with application to neuroimaging techniques, this nomenclature will be used here, whilst remaining aware that statistical literature properly refers to these models as mixed effects models.

Statistical variance in estimation of neuroimaging parameters can be discussed with reference to a hierarchical structure, composed of measurement, intra-subject and inter-subject levels. Sources of error on the measurement will affect all measurements made. If a subject is repeatedly scanned, it is possible that the parameter of interest will vary

biologically from one scan to the next. This is the second level of variance. The third level of variance accounts for the fact that the biological parameter may also be randomly distributed across the population itself, of which the subjects are a sample. Hence, if β is the parameter of interest

$$\beta_{ij} = \bar{\beta} + \epsilon_i + \epsilon_{ij} + \epsilon_{ijk} \tag{8.3}$$

where i is the subject number, j the scan number, k the measurement taken, and ϵ the errors with $E(\epsilon) = 0$.

Most, if not all, random effects models that will be considered in neuroimaging can be expressed in the framework of Eqn 8.1. The exact specification of the different terms will depend on the application and the level at which the analysis is carried out. Assumptions may also be made about parameters that come from non-linear models, in order to extend the methods to these models.

8.2 Current Random Effect Methods

Principally there are two methods currently in use which account for random effects. These methods have only recently been considered for the application as random effects models. The implicit use of random effects models was originally widespread, but more advanced statistical techniques for estimation of measurement error have resulted in a wider usage of purely fixed effects models. The neuroimaging community is now returning to the use of original models as they are now explicitly seen to account for random effects.

8.2.1 SPM Random Effect Model

Statistical Parametric Mapping (SPM) software (Ashburner et al., 1999) is the primary software package used in the neuroimaging community. However SPM has also become synonymous with particular paradigms of analysis of functional neuroimaging data sets, both fMRI and PET, and is used as such interchangeably with the software package. The random effects component (Holmes and Friston, 1998) is one of paradigms that are defined in terms of SPM, which is also a known paradigm outside the neuroimaging literature as a repeated measures analysis.

The SPM random effect model is based on the fact that subjects are essentially repeated measure studies and that they are essentially balanced and separable. This facilitates the use of a multi-level analysis (Holmes and Friston, 1998) where contrasts are calculated

for each subject (summary statistics) and then these contrasts are taken to the next level where they are analysed for random effects. This can be formulated in the following way (Holmes and Friston, 1998)

$$\begin{aligned} \text{Level 1:} \quad y_i &= X_i\beta_i + \epsilon_i \\ \alpha_i &= c^T\beta_i \\ \text{Level 2:} \quad \alpha &\sim N(\bar{\alpha}, \sigma^2) \end{aligned} \tag{8.4}$$

The number of degrees of freedom in this model for inference is equal to the number of degrees of freedom in the Level 2 model. Thus in most situations this is equal to one less than the number of subjects.

There are many assumptions made in order to use these models, which are documented in the SPM documentation (Ashburner et al., 1999). However, most of these are reasonable for neuroimaging data sets, where the only use of the random effects model is to make inferences about the global contrast. However these methods would not be suitable to estimate the variance components themselves. The fixed effects variances which can be calculated in Level 1, could lead to negative estimates of variance in Level 2, as the variances are calculated by taking one variance minus another, and there is no guarantee that this quantity is non-negative in this framework.

8.2.2 Voxel Pooling

Another method for increasing the sensitivity for detection is voxel pooling (Worsley et al., 1992). Whilst not strictly a random effects method, it can be used in both fixed and random effects models in the same way, and is therefore considered here for the random effects case. It should really be considered as a method for increasing the degrees of freedom of the estimator. Often the problem of random effects is that of much reduced degrees of freedom. The pooling method relies on the fact that each voxel's variance can be taken as an estimate of the global variance of the system. It is primarily used in PET rCBF studies, where the variance at each voxel is assumed to be constant throughout the image. Thus an estimate of the variance is made, using all the data from the entire image, giving an essentially known variance for the data set. This, then, allows inferences to be made about the data set, using normal statistics, and so the degrees of freedom problem in the random effects model no longer remains an issue. This method relies on the fact that each voxel's variance can be taken as an estimate of the global variance of the system. For rCBF studies this appears to be a viable assumption, although it is

increasingly believed that the variance is heterogeneous across the image and as such voxel estimates should be used, but for other tracers and imaging modalities this assumption must be rigorously assessed. If this is not satisfied then the voxel pooling approach cannot be used, as heterogeneity in the variance would lead to local under or over estimates of the variance. This would result in false positives or negatives in subsequent hypothesis testing.

8.3 Neuroreceptor Ligand Studies

The use of the SPM approach for neuroreceptor studies is perfectly valid. However it suffers from a lack of sensitivity due to the low number of degrees of freedom in most cases, equal to the number of subjects less one. Therefore it would be highly desirable to find methods to assess the studies which take into account the random effects but are more sensitive and use the variance components estimated in the previous chapters.

The use of voxel pooling as described above requires the fundamental assumption of homogeneous variance across the image. Therefore it is necessary to assess the assumptions in the case of neuroreceptor ligand data sets.

8.3.1 Voxel Pooling

The assumptions required to make use of voxel pooling were assessed for the ligand $[^{11}C]$SCH 23390. The sd image (Figure 8.2) has anatomical structure, therefore, unlike in rCBF PET scans (Worsley et al., 1992), the variance is not constant throughout the image. One can see that the variance appears to be higher in areas of high ligand binding. Therefore the method of increasing the df by pooling the voxel sd across the image is not applicable for $[^{11}C]$SCH 23390. It is also likely that this method will not be valid for any other ligand of the dopamine system, where there will be high variability in binding sites, and therefore in radioactivity distribution. This is also likely to be the case for other non-uniformly distributed receptor systems.

8.3.2 Variance Ratio

It has been shown above that it is not possible to use voxel pooling for neuroreceptor ligand studies. However local pooling might be possible if the variance or a function of the variance was locally homogeneous. As can be seen in Figure 8.2, the variance itself is not locally homogeneous, but it will be shown that the ratio of the fixed effects variance to

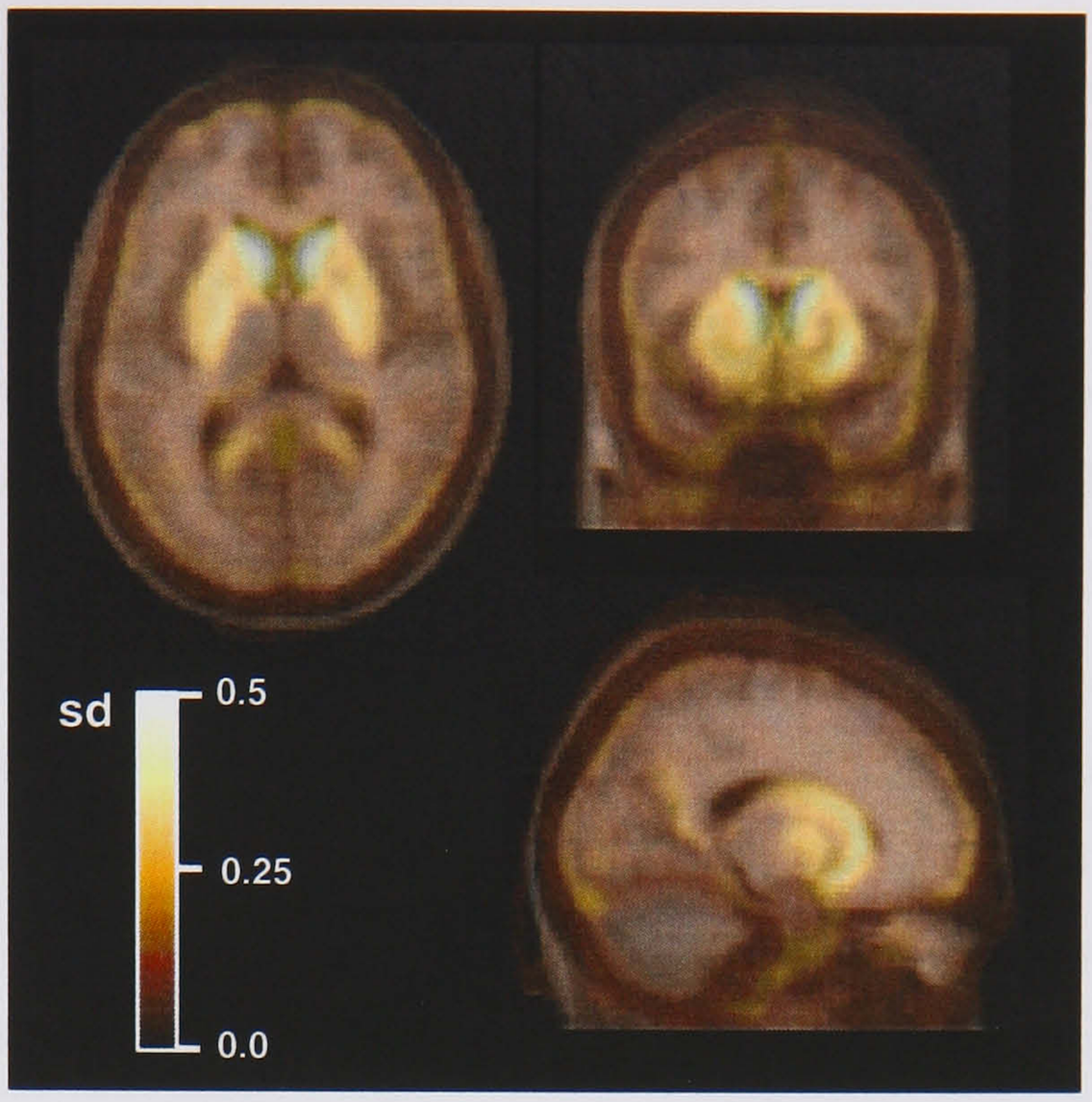


Figure 8.2: Standard deviation image of BP generated from 34 normal subjects who each underwent two $[^{11}C]$SCH 23390 scans. The sd map is in colour overlayed on the average MRI from all the subjects. The sd distribution has anatomical structure, with high sd in areas of high ligand binding. This precludes the use of pooling the sd over voxels.

the random effects variance is more homogeneous. However before this variance ratio can be studied, it is necessary to calculate the differing components of the variance, namely the random and the fixed effect variances.

8.3.3 Restricted Maximum Likelihood (ReML) Algorithm

ReML is an algorithm to calculate differing variance components. It is now one of the most widely used of the algorithms to calculate the variance components. This is due to the properties that the variance estimates are non-negative, the estimates themselves are less biased than with traditional ML as the degrees of freedom lost in the calculation are accounted for, and the estimates in the balanced case are identical to the Analysis of Variance (Anova) estimates.

The algorithms used here will be based on the following model,

$$\alpha = X\gamma + Zu + \epsilon \tag{8.5}$$

where X is a design matrix for any covariates that are subject specific (such as age, smoking, etc.), Z is a random effects matrix (often the identity), γ the fixed effects vector, u a random vector, ϵ the fixed effects error, and α the contrasts estimated in the previous

level. For example in the SPM analysis the X matrix is a vector of ones, and Z is the identity, yields the following

$$\alpha = \mathbf{1}\gamma + \eta \tag{8.6}$$

where η is a combination of the errors with variance $\sigma^2_{\text{fixed}} + \sigma^2_{\text{random}}$ and γ contains the contrasts ($\hat{\alpha}$) from the within subject model. However in the SPM analysis only the total variance is required, not the individual components, so the use of the ReML algorithm is not required.

There is another useful consequence of this framework. In neuroreceptor ligand studies, the original model is often nonlinear (see chapters 5 & 6) and as such it would be difficult to combine the non-linear components into the mixed model. The use of the summary statistics of the contrast and its variance facilitates the use of the mixed model in a hierarchical ordering.

The ReML algorithm due to Laird et al (1987) is very applicable to the above formulation. In the formulation of the above model, u is distributed N(0,σ^2_{random}) and ϵ is distributed N(0,D) where D is a diagonal matrix of the fixed effects variances. The exact specification of D is dependent on the assumed model and will be discussed later.

If the fixed effects variances are assumed to be known then the algorithm for updating the random variance is then given by

$$\sigma^2_{i+1} = (\sigma^2_i(n - \sigma^2_i tr(R_\Sigma)) + \sigma^4_i \alpha' R^2_\Sigma \alpha)/n \tag{8.7}$$

where $\sigma^2_0 = \alpha' R_I \alpha$, $R_\Sigma = \Sigma^{-1} - \Sigma^{-1}X(X'\Sigma^{-1}X)^{-1}X'\Sigma^{-1}$ and $\Sigma = D + I\sigma^2_{\text{random}}$.

The ReML algorithm facilitates the estimation of the two variance components which can then be studied separately to increase the sensitivity by local smoothing. Although unlikely in most situations to be critical, the choice of D is open to interpretation. If there is reason to infer that there are differing error rates in the differing experiments then the choice of D should be such that the data is appropriately weighted ($D = \Lambda(\text{Var}(\alpha_i))$). In most situations, it is reasonable that the experimental error on the parameter (ie fixed error) is the same for each subject, thus the best estimate of the fixed error is from the weighted average of the error on the parameter, ie

$$\sigma^2_{\text{fixed}} = \sum_{j=1}^{n} \frac{\nu_j \text{Var}(\alpha_j)}{\sum_{i=1}^{n} \nu_i} \tag{8.8}$$

where ν are the degrees of freedom associated with each parameter. Then $D = I\sigma^2_{\text{fixed}}$. It is unlikely however, that D need be more complex than a diagonal matrix, as the subjects can reasonably be deemed independent.

8.3.4 Variance Ratio Smoothing

In neuroreceptor ligand studies, as can been seen in Figure 8.2 above, the variance is not homogeneous. However it will be seen that the ratio of the fixed variance to the random variance is far more homogeneous.

This can be used to increase the sensitivity of the analysis, by using a local variant of the voxel pooling method. This method involves smoothing the ratio by a Gaussian kernel (Worsley et al., 2002). The amount of smoothing is determined by the properties of the random and fixed field and is set to ensure that the number of degrees of freedom in the resulting image are sufficient that an error in approximation of these makes little difference to the resulting thresholds (ie DFs are large).

If σ^2_{fixed} is the variance of the fixed field and σ^2_{random} is the variance of the random field, then

$$\tilde{\sigma}^2_{\text{random}} = \text{smooth}\left(\frac{\sigma^2_{\text{random}}}{\sigma^2_{\text{fixed}}}\right) \times \sigma^2_{\text{fixed}} \tag{8.9}$$

where smooth() is the smoothing operator. This leads to a smoothed variance ratio, and hence a smoothed random variance map. This can then be used for making inferences about the parameter or the contrast.

8.3.5 Degrees of Freedom

The effective degrees of freedom from the smoothed model have been calculated by Worsley (2002) . The resulting formula for the degrees of freedom is given by

$$\nu_{\text{ratio}} = \nu_{\text{random}}\left(2\left(\frac{\text{FWHM}_{\text{ratio}}}{\text{FWHM}_{\text{effect}}}\right)^2 + 1\right)^{3/2} \tag{8.10}$$

where FWHM is the filter applied to the differing images. The final effective degrees of freedom is then given by

$$\frac{1}{\tilde{\nu}_{\text{random}}} = \frac{1}{\nu_{\text{ratio}}} + \frac{1}{\nu_{\text{fixed}}} \tag{8.11}$$

This shows that by altering the smoothing through changing the FWHM of the filter, it is possible to alter the effective degrees of freedom. If FWHM is set to 0 then a full random effects analysis is performed, whilst if FWHM is set to ∞, a fixed effects analysis is performed. As mentioned above, as these formulae are based on approximations, in order that the distributions are not overly affected by estimation errors, FWHM needs to be chosen to be large enough so that the effective degrees of freedom are large.

8.4 Validation Studies

The validation of the variance ratio smoothing was carried out using the control data from chapter 5 Section 5.5.2. The results from chapter 5 gave a fixed effects signal (Figure 8.3) and error estimate for each of the paired studies.

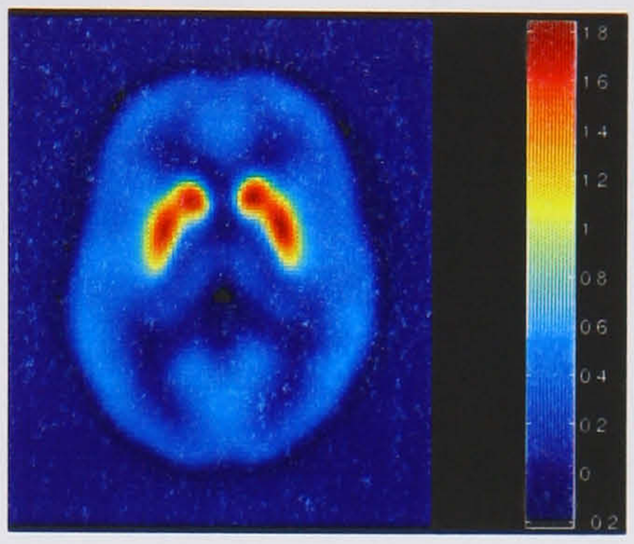
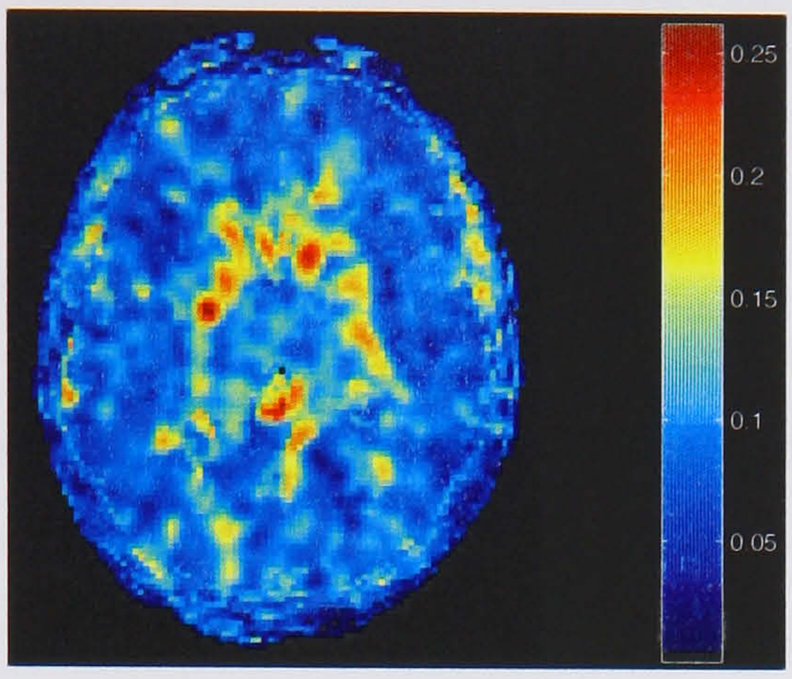


Figure 8.3: Mean Binding Potential Image of Control Data.

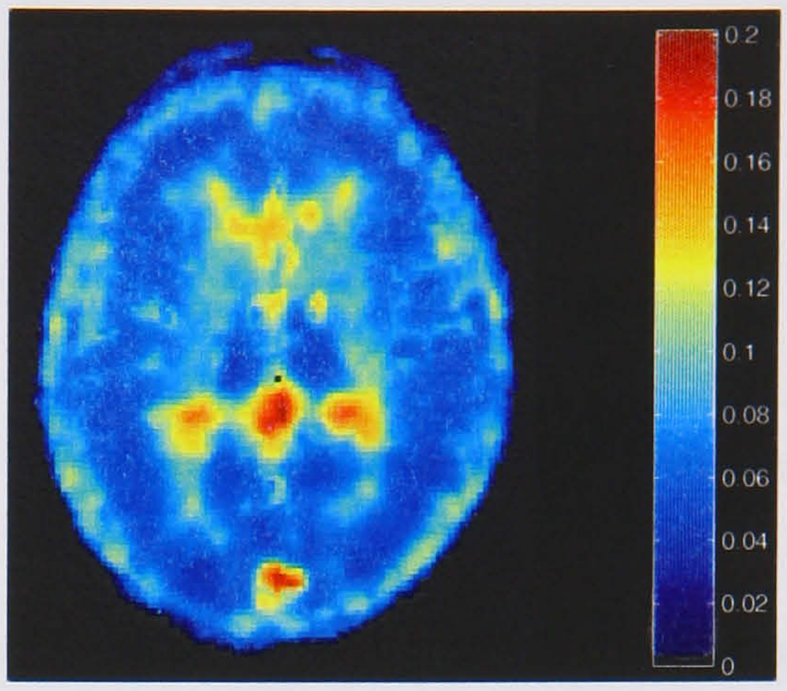
The usual PET and indeed fMRI experimental design is that of Activation / Baseline subtraction, and thus this design was chosen here. The contrast of interest was therefore the first scan subtracted from the second scan. As has already been seen, this contrast does not yield false positives when tested even under a fixed effects model. Thus a random effects model which is less sensitive is also highly unlikely to yield any false positives. The primary interest for this analysis, however, is not detection but to compare the fixed and random effect variance estimates.

The variance estimates were generated as above, and the mean fixed variance was used as the variance estimate for all the studies. This was chosen as there is no evidence that the measurement of BP within a scan is subject to changes between subjects. When the variance ratios were calculated, structure was found on one side. However this was found to be the result of misregistration which increased the variance in the random effects image over that expected from the purely fixed effects images. The misregistered scans were detected by visual inspection and removed from the analysis. This yielded the following results from the resulting eight pairs of scans.

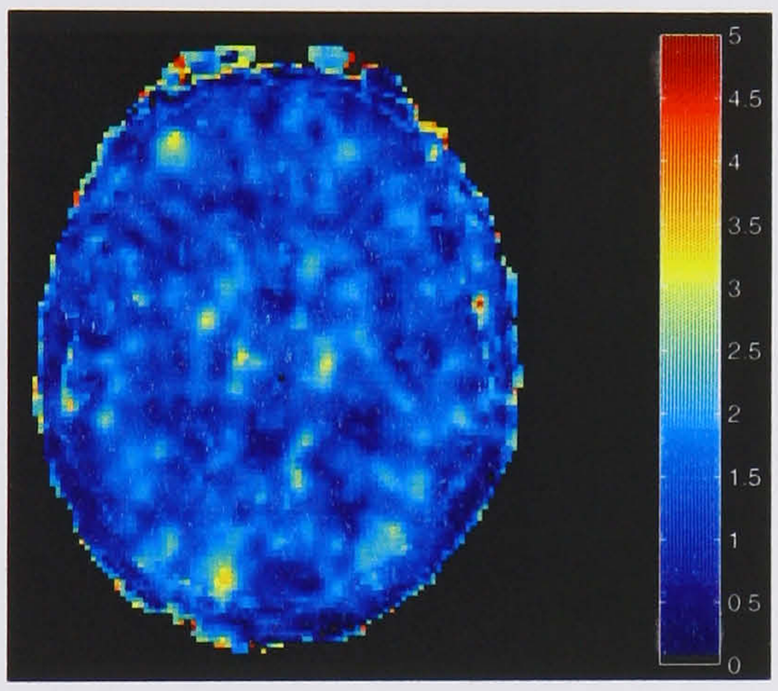
Figure 8.4 is a composite of the different elements that are required or calculated in the method. The random effects map clearly has structure. The fixed effects model also contains similar structure, although it is not as pronounced in real terms, the multiplicative factor is moderately stable as can be seen in the ratio image. The region in the middle of the fixed effects map, contains no signal (see Figure 8.3) and thus whilst its estimate of variance in the fixed effects model is high, it is stable in the random effects map. However



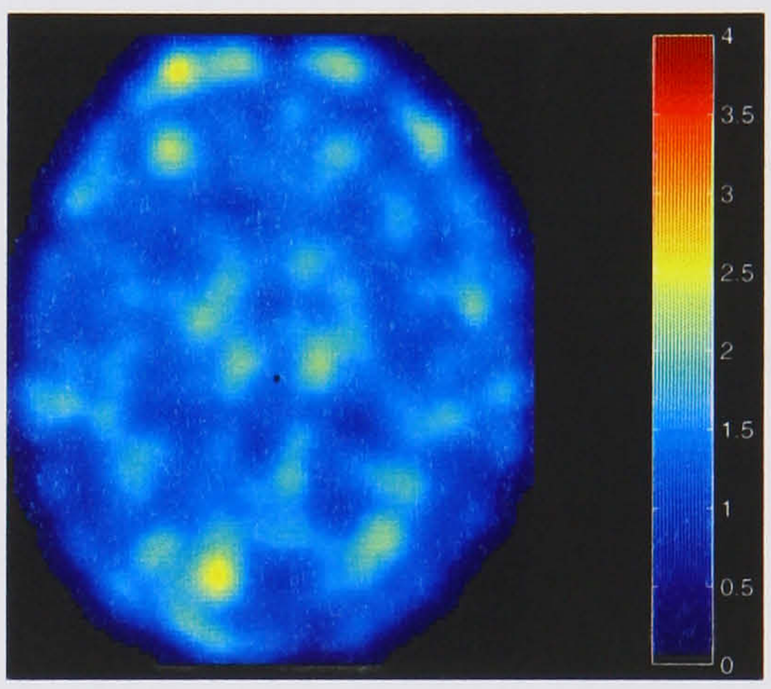
(a) Random Effects Image



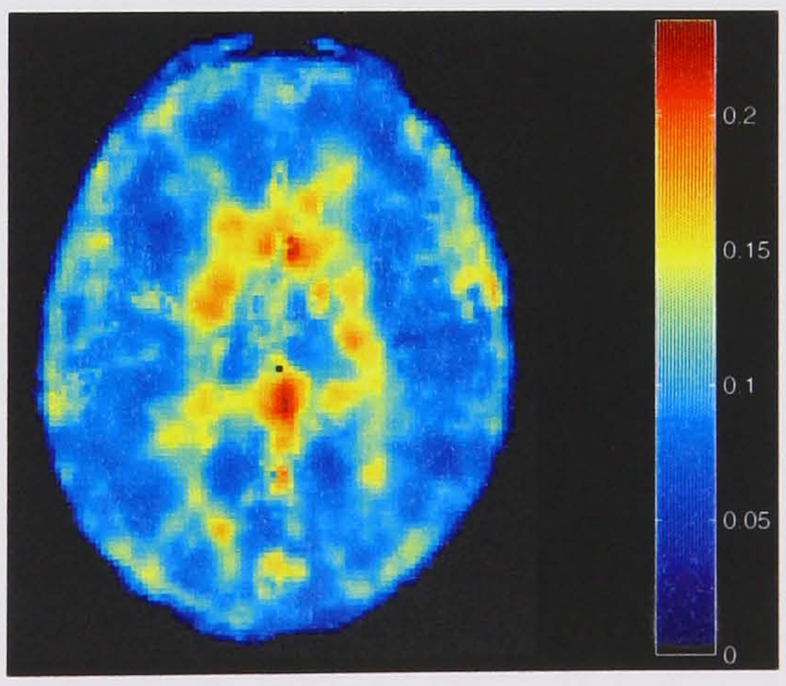
(b) Fixed Effects Image



(c) Ratio Image



(d) Smoothed (FWHM=10mm) Ratio Image



(e) Final Random Effects Image

Figure 8.4: Variance Ratio Smoothing.

this will not be a problem in the analysis, as no hypotheses will be tested in regions of no signal. The smoothed ratio image is then generated, and then remultiplied by the fixed variance to produce the final variance map. The FWHM 10mm smoothing yielded approximately 150 degrees of freedom.

8.5 Summary

A review of the current methods used to account for random effects has been presented here, and a new method expanded and validated for neuroreceptor ligand studies. This method allows for random effects, whilst using the spatial information to facilitate detection. It provides a spatial link between the random and fixed effects model, retaining a large number of degrees of freedom of the fixed effects model, whilst accounting for the random effects, which are needed to make true inference about data sets. Whilst the methods here have been developed previously for the use of fMRI data, here they are validated for PET and the whole method expressed in terms of a mixed effects model framework. This will facilitate the understanding and choice of the particular model and parameters which are required in different types of analyses.

Chapter 9

Concluding Remarks

The goal of this thesis was to present novel methods of analysis for Spatial, Temporal and Spatio-Temporal data within a statistical framework. Previous methods have concentrated on either estimation or inference. Here a combined framework for both estimation and inference has been developed across the differing data dimensions.

Novel algorithms and theory have been developed to account for the multidimensional nature of the data. Tensor algorithms in partial volume have allowed noise models to be incorporated into the analysis, whilst variance formulations of wavelet reconstruction have also been calculated using a similar tensor structure.

New methods for the analysis of temporal data have also been developed based on existing estimation techniques. These techniques have primarily been associated with estimation error variances on parameters of interest, through theoretical or empirical approaches. These approaches have been generalised to spatio-temporal data, through the use of the wavelet transform, and the transform of data from one domain to another, with a better functional representation of the data.

Finally random effects methods have been developed and discussed using the variance estimates obtained from the previously developed analyses. This will enable a true random effects analysis of the data, without some of the limitations imposed by the multiple comparison nature of the data sets.

Ideas for future work are considered in the relevant chapters themselves. However, it should be emphasised that neuroimaging is developing faster than ever before, and as new techniques are developed, new methods of analysis will be required. More complex questions and ideas are continuously being posed, and this requires ever more sensitive statistical procedures to estimate their effects and infer their validity.

Appendix A

Mathematical Functions and Algorithms

A.1 Khatri-Rao Row Product

This product is the row-wise kronecker ($\otimes$)product between the rows of A, a $k \times m$ matrix and B, a $k \times n$ matrix giving a $k \times mn$ matrix (Rao and Mitra, 1971). The product takes the following form

$$A \odot B = \begin{bmatrix} a_1 \otimes b_1 \\ a_2 \otimes b_2 \\ \cdots \\ a_k \otimes b_k \end{bmatrix} = \begin{bmatrix} a_{11}b_1\ a_{12}b_1\ \cdots\ a_{1n}b_1 \\ a_{21}b_2\ a_{22}b_2\ \cdots\ a_{2n}b_2 \\ \cdots \\ a_{k1}b_k\ a_{k2}b_k\ \cdots\ a_{kn}b_k \end{bmatrix} \tag{A.1}$$

where a_{ij} is the (i, j) element of A and a_i, b_i are the ith rows of A and B respectively.

A.2 Residuals Bootstrap

The description of the bootstrap procedure for Spectral Analysis (Turkheimer et al., 1998) is given here. If α is the solution from spectral analysis, with the model matrix X, to the data C_T then if we define r_k, the residual at time point k to be

$$r_k = C_T(t_k) - (X\alpha)_k \tag{A.2}$$

then we define a bootstrap sample * for $k = 1, \ldots, T$ as

$$C_T^*(t_k) = (X\alpha)_k + r_k^* \tag{A.3}$$

where r_k^* is the bootstrap residual resulting from sampling with replacement from the original residuals. Spectral Analysis is then applied to the new data to generate a new α^*. This is then repeated to build up a distribution of the α. The methods can be extended to include weights in the data, and details of these resampling methods are given in Turkheimer et al (1998).

A.3 Bias Reduction of Autocorrelations

A method for the reduction of bias in the estimated autocorrelation parameters of an AR(p) model has been given by Worsley et al (2002). The bias reduction formulae have been reproduced from this paper.

Let D_l be a matrix of zeros with ones on the lth upper off-diagonal, so that the expectation of the lag l is given by

$$E(r'D_l r) = \mathrm{tr}(RD_lRV)\sigma^2 \approx \mathrm{tr}(RD_l)\nu_0 + \sum_{j=1}^{p} \mathrm{tr}(RD_lR(D_j + D_j'))\nu_j \qquad \text{(A.4)}$$

where $V\sigma^2$ is approximated by v_j on the jth off-diagonal, $0 \leq j \leq p$, allows can be solved to give approximate unbiased estimators. To do this, let

$$a_l = \sum_{i=l+1}^{n} r_i r_{i-l} \qquad \text{(A.5)}$$

$$m_{ij} = \begin{cases} \mathrm{tr}(RD_l) & j = 0 \\ \mathrm{tr}(RD_lR(D_j + D_j')) & 1 \leq j \leq \rho \end{cases} \qquad \text{(A.6)}$$

and the estimated covariances are given by

$$\nu = M^{-1}a \qquad \text{(A.7)}$$

and the autocorrelations at lag l are estimated by

$$\rho_l = \nu_l/\nu_0 \qquad \text{(A.8)}$$

A.4 Random Field Theory for Multiple Comparisons

Random field theory is now routinely used to calculate thresholds for use in determining inferences for neuroimaging studies. Whilst the results that are used are given here, the

derivations are given by Worsley (1994). The results for the Gaussian and t Field cases are given below, and the results for χ^2 and F field are given in Worsley (1996a).

The overall probabilities are approximated by the following formulae

$$P(M \geq t) \approx \sum_{D=0}^{3} R_D(V)\rho_D(t) \tag{A.9}$$

where $R_D(V)$ are given by the following for voxel data

$$\begin{aligned}
R_0(V) &= P - (E_x + E_y + Ez) + (F_{xy} + F_{xz} + F_{yz}) - C && \text{(A.10)}\\
R_1(V) &= (E_x - F_{xy} - F_{xz} + C)r_x + (E_y - F_{yz} - F_{xy} + C)r_y + && \text{(A.11)}\\
&\quad \ldots + (E_z - F_{yz} - F_{xz} + C)r_z \\
R_2(V) &= (F_{xy} - C)r_x r_y + (F_{xz} - C)r_x r_z + (F_{yz} - C)r_y r_z && \text{(A.12)}\\
R_3(V) &= C r_x r_y r_z && \text{(A.13)}
\end{aligned}$$

where P are the points in the region, E are the edges, F are the faces, and C the number of simple cubes. r_x, r_y, r_z are the resel dimensions, given by redefining the voxel sizes by the FWHM in each direction. The values of ρ are dependent on the field.

Gaussian ρ Functions

$$\begin{aligned}
\rho_0(t) &= \int_t^\infty \frac{1}{(2\pi)^{1/2}} e^{-u^2/2} du && \text{(A.14)}\\
\rho_1(t) &= \frac{(4\log 2)^{1/2}}{2\pi} e^{-t^2/2} && \text{(A.15)}\\
\rho_2(t) &= \frac{(4\log 2)}{(2\pi)^{3/2}} t e^{-t^2/2} && \text{(A.16)}\\
\rho_3(t) &= \frac{(4\log 2)^{3/2}}{(2\pi)^2} (t^2 - 1) e^{-t^2/2} && \text{(A.17)}
\end{aligned}$$

T Field ρ Functions

$$\begin{aligned}
\rho_0(t) &= \int_t^\infty \frac{\Gamma\left(\frac{\nu+1}{2}\right)}{(2\pi)^{1/2}\Gamma\left(\frac{\nu}{2}\right)} \left(1 + \frac{u^2}{\nu}\right)^{-\frac{\nu-1}{2}} du && \text{(A.18)}\\
\rho_1(t) &= \frac{(4\log 2)^{1/2}}{2\pi} \left(1 + \frac{t^2}{\nu}\right)^{\frac{\nu-1}{2}} && \text{(A.19)}\\
\rho_2(t) &= \frac{(4\log 2)}{(2\pi)^{3/2}} \frac{\Gamma\left(\frac{\nu+1}{2}\right)}{\left(\frac{\nu}{2}\right)^{1/2}\Gamma\left(\frac{\nu}{2}\right)} \left(1 + \frac{t^2}{\nu}\right)^{\frac{\nu-1}{2}} && \text{(A.20)}\\
\rho_3(t) &= \frac{(4\log 2)^{3/2}}{(2\pi)^2} \left(1 + \frac{t^2}{\nu}\right)^{\frac{\nu-1}{2}} \left(\frac{\nu-1}{\nu} t^2 - 1\right) && \text{(A.21)}
\end{aligned}$$

Bibliography

Allen, E. J., Baglama, J., and Boyd, S. K. (2000). Numerical approximation of the product of the square root of a matrix with a vector. *Linear Algebra and Its Applications*, 310(1-3):167–181.

Anderson, T. W. (1971). *The statistical analysis of time series.* Wiley, New York,.

Ashburner, J. and Friston, K. (1997). Multimodal image coregistration and partitioning–a unified framework. *Neuroimage*, 6(3):209–17.

Ashburner, J., Friston, K., Holmes, A. P., and Poline, J. B. (1999). *Statistical Parametric Mapping.* Wellcome Department of Cognitive Neurology, London, 99 edition.

Ashburner, J. and Friston, K. J. (1999). Nonlinear spatial normalization using basis functions. *Hum Brain Mapp*, 7(4):254–66.

Ashburner, J. and Friston, K. J. (2000). Voxel-based morphometry–the methods. *Neuroimage*, 11(6 Pt 1):805–21.

Asselin, M.-C., Cunningham, V. J., Turjanski, N., Wahl, L. M., Bloomfield, P. M., Gunn, R. N., and Nahmias, C. (2001). Venous sinuses vs on-line arterial sampling as input functions in PET. In A. Gjedde, S. B. Hansen, G. M. K. and Paulson, O. B., editors, *Physiological Imaging of the Brain with PET*, pages 73–81. Academic Press.

Aston, J. A. D., Gunn, R. N., Worsley, K. J., Ma, Y., Evans, A. C., and Dagher, A. (2000). A statistical method for the analysis of positron emission tomography neuroreceptor ligand data. *Neuroimage*, 12:245–256.

Axelsson, O. (1994). *Iterative solution methods.* Cambridge University Press, Cambridge New York.

Bailey, D. L. (1992). 3D acquisition and reconstruction in positron emission tomography. *Ann Nucl Med*, 6(3):123–30.

Bailey, D. L. and Meikle, S. R. (1994). A convolution-subtraction scatter correction method for 3D PET. *Physics in Medicine and Biology*, 39(3):411–424.

Bailey, D. L., Young, H., Bloomfield, P. M., Meikle, S. R., Glass, D., Myers, M. J., Spinks, T. J., Watson, C. C., Luk, P., Peters, A. M., and Jones, T. (1997). ECAT ART - a continuously rotating PET camera: Performance characteristics, initial clinical studies, and installation

considerations in a nuclear medicine department. *European Journal of Nuclear Medicine*, 24(1):6–15.

Bernardo, J. and Smith, A. (1994). *Bayesian Theory*. Wiley, Chichester.

Bookstein, F. L. (2001). "voxel-based morphometry" should not be used with imperfectly registered images. *Neuroimage*, 14(6):1454–62.

Buechel, C. and Friston, K. (1997). Characterising functional integration. In Frackowiak, R., Friston, K., Frith, C., Dolan, R., and Mazziotta, J. C., editors, *Human Brain Function*, pages 467–86. Academic Press, London.

Buxton, R. B. and Frank, L. R. (1997). A model for the coupling between cerebral blood flow and oxygen metabolism during neural stimulation. *J Cereb Blood Flow Metab*, 17(1):64–72.

Buxton, R. B., Wong, E. C., and Frank, L. R. (1998). Dynamics of blood flow and oxygenation changes during brain activation: the balloon model. *Magn Reson Med*, 39(6):855–64.

Carson, R. E. (1986). Parameter estimation in positron emission tomography. In Phelps, M. E., Mazziotta, J. C., and Schelbert, H. R., editors, *Positron emission tomography and autoradiography : principles and applications for the brain and heart*, pages xii, 690. Raven Press, New York.

Carson, R. E., Yan, Y., Daube-Witherspoon, M. E., Freedman, N., Bacharach, S. L., and Herscovitch, P. (1993). An approximation formula for the variance of PET region-of- interest values. *IEEE Transactions on Medical Imaging*, 12(2):240–250.

Collins, D. L., Neelin, P., Peters, T. M., and Evans, A. C. (1994). Automatic 3D intersubject registration of MR volumetric data in standardized talairach space. *J Comput Assist Tomogr*, 18(2):192–205.

Comar, D., Berridge, M., Maziere, B., and Crouzel, C. (1982). Radiopharmaceuticals labelled with positron-emitting radioisotopes. In Ell, P. and Holman, B., editors, *Computed Emission Tomography*, pages 42–91. Oxford University Press, Oxford.

Cunningham, V. J., Gunn, R. N., Byrne, H., and Matthews, J. (1998). Suppression of noise artifacts in spectral analysis of dynamic PET studies. In Carson, R. E., Daube-Witherspoon, M. E., and Herscovitch, P., editors, *Quantitative Functional Brain Imaging with Positron Emission Tomography*, pages 329–337. Academic Press.

Cunningham, V. J. and Jones, T. (1993). Spectral analysis of dynamic PET studies. *J Cereb Blood Flow Metab*, 13(1):15–23.

Cunningham, V. J. and Lammertsma, A. A. (1994). Radioligand studies in brain: Kinetic analysis of PET data. *Medicinal Chemistry Research*, 5:79–96.

Dagher, A., Bleicher, C., Aston, J. A. D., Gunn, R. N., Clarke, P., and Cumming, P. (2001). Reduced dopamine D1 receptor binding in the ventral striatum of cigarette smokers. *Synapse*, 42(1):48–53.

Daubechies, I. (1992). *Ten lectures on wavelets.* CBMS-NSF regional conference series in applied mathematics ; 61. Society for Industrial and Applied Mathematics, Philadelphia, Pa.

Desco, M., Hernandez, J. A., Santos, A., and Brammer, M. (2001). Multiresolution analysis in fMRI: sensitivity and specificity in the detection of brain activation. *Hum Brain Mapp*, 14(1):16–27.

Donoho, D. L. and Johnstone, I. M. (1994). Ideal spatial adaptation by wavelet shrinkage. *Biometrika*, 83:425–455.

Donoho, D. L. and Johnstone, I. M. (1995). Adapting to unknown smoothness via wavelet shrinkage. *Journal of the American Statistical Association*, 90(432):1200–1224.

Durbin, J. and Watson, G. (1950). Testing for serial correlation in least squares regression: I. *Biometrika*, 37(3/4):409–428.

Durbin, J. and Watson, G. (1951). Testing for serial correlation in least squares regression: Ii. *Biometrika*, 38(1/2):159–177.

Durbin, J. and Watson, G. (1971). Testing for serial correlation in least squares regression: Iii. *Biometrika*, 58(1):1–19.

Efron, B. and Tibshirani, R. (1993). *A Introduction to the Bootstrap.* Chapman and Hall, New York.

Farde, L., Eriksson, L., Blomquist, G., and Halldin, C. (1989). Kinetic-analysis of central ^{11}C-raclopride binding to D_2- dopamine receptors studied by pet - a comparison to the equilibrium-analysis. *Journal of Cerebral Blood Flow and Metabolism*, 9(5):696–708.

Friston, K., Frith, C., Liddle, P., and Frackowiak, R. (1993). Functional connectivity: The principal-component analysis of large (PET) data sets. *Journal of Cerebral Blood Flow and Metabolism*, 13:5–14.

Friston, K., Poline, J. B., Holmes, A. P., Frith, C., and Frackowiak, R. (1996). A multivariate analysis of PET activation studies. *Human Brain Mapping*, 4:140–151.

Friston, K. J., Fletcher, P., Josephs, O., Holmes, A., Rugg, M. D., and Turner, R. (1998). Event-related fMRI: characterizing differential responses. *Neuroimage*, 7(1):30–40.

Friston, K. J., Holmes, A. P., and Worsley, K. J. (1999). How many subjects constitute a study? *Neuroimage*, 10(1):1–5.

Geman, S. and Geman, D. (1984). Stochastic relaxation, gibbs distributions, and the bayesian restoration of images. *IEEE Transactions on Pattern Analysis and Machine Intelligence*, 6:721–741.

Genovese, C. (2000). A bayesian time-course model for functional magnetic resonance imaging data. *Journal of the American Statistical Association*, 95:691–719.

Geweke, J. (1996). Bayesian inference for linear models subject to linear constraints. In Johnson, W., Lee, J., and Zellner, A., editors, *Modeling and Prediction: Honoring Seymour Geisser*,

pages 248–263. Springer-Verlag, New York.

Glover, G. H. (1999). Deconvolution of impulse response in event-related BOLD fMRI. *Neuroimage*, 9(4):416–29.

Golub, G. H. and Van Loan, C. F. (1983). *Matrix Computations*. The Johns Hopkins University Press, Baltimore, USA.

Grootoonk, S. (1995). *Dual energy window correction for scattered photons in 3D positron emission tomography*. PhD thesis, University of Surrey.

Gunn, R. N. (1996). *Mathematical modelling and identifiability applied to positron emission tomography*. PhD thesis, University of Warwick.

Gunn, R. N., Ashburner, J., Aston, J. A. D., and Cunningham, V. J. (2001a). Analysis of functional imaging datasets via functional segmentation. In Gjedde, A., Hansen, S., Knudsen, G., and Paulson, O. B., editors, *Physiological Imaging of the Brain with PET*, pages 45–50. Academic Press, London.

Gunn, R. N., Gunn, S. R., and Cunningham, V. J. (2001b). Positron emission tomography compartmental models. *J Cereb Blood Flow Metab*, 21(6):635–52.

Gunn, R. N., Lammertsma, A. A., Hume, S. P., and Cunningham, V. J. (1997). Parametric imaging of ligand-receptor binding in PET using a simplified reference region model. *Neuroimage*, 6(4):279–287.

Hammers, A., Koepp, M. J., Free, S., Brett, M., Richardson, M. P., Labbé, C., Cunningham, V. J., Brooks, D. J., and Duncan, J. S. (2002). Implementation and application of a new brain template for multiple volumes of interest. *Human Brain Mapping*, in press.

Hirvonen, J., Nagren, T., Kajander, J., and Hietala, J. (2001). Measurement of cortical dopamine D-1 receptor binding with C-11 SCH 23390: A test-retest analysis. *Journal of Cerebral Blood Flow and Metabolism*, 21(10):1146–1150.

Hoffman, E. J., Huang, S. C., and Phelps, M. E. (1979). Quantitation in positron emission computed tomography: 1. effect of object size. *J Comput Assist Tomogr*, 3(3):299–308.

Holmes, A. P. (1994). *Statistical Issues in Functional Brain Mapping*. PhD thesis, University of Glasgow.

Holmes, A. P. and Friston, K. (1998). Generalisability, random effects and population inference. *Neuroimage*, 7(4-2/3):S754.

Holmes, C. J., Hoge, R., Collins, L., Woods, R., Toga, A. W., and Evans, A. C. (1998). Enhancement of MR images using registration for signal averaging. *J Comput Assist Tomogr*, 22(2):324–33.

Huang, S. C. and Phelps, M. E. (1986). Principles of tracer kinetic modeling in positron emission tomography and autoradiography. In Phelps, M. E., Mazziotta, J. C., and Schelbert, H. R.,

editors, *Positron emission tomography and autoradiography : principles and applications for the brain and heart*, pages xii, 690. Raven Press, New York.

Huesman, R. H. (1997). Equivalent methods to analyse dynamic experiments in which the input function is noisy. *Phys Med Biol*, 42(1):147–53.

Iida, H., Law, I., Pakkenberg, B., Krarup-Hansen, A., Eberl, S., Holm, S., Hansen, A. K., Gundersen, H. J., Thomsen, C., Svarer, C., Ring, P., Friberg, L., and Paulson, O. B. (2000). Quantitation of regional cerebral blood flow corrected for partial volume effect using $[^{15}O]$ water and PET: I. theory, error analysis, and stereologic comparison. *J Cereb Blood Flow Metab*, 20(8):1237–51.

Johnstone, I. M. and Silverman, B. (1997). Wavelet threshold estimators for data with correlated noise. *Journal of the Royal Statistical Society Series B*, 59:319–351.

Jones, A. K. P., Cunningham, V. J., Hakawa, S. K., Fujiwara, T., Qi, L. Y., Luthra, S. K., Ashburner, J., Osman, S., and Jones, T. (1994). Quantitation of ^{11}C-diprenorphine cerebral kinetics in man acquired by PET using presaturation, pulse-chase and tracer-only protocols. *Journal of Neuroscience Methods*, 51(2):123–134.

Jones, T. (1982). The application of positron emission tomography. In Ell, P. and Holman, B., editors, *Computed Emission Tomography*, pages 211–242. Oxford University Press, Oxford.

Judge, G. and Takayama, T. (1966). Inequality restrictions in regression analysis. *Journal of the American Statistical Association*, 61:166–181.

Karp, J. S., Daube-Witherspoon, M. E., and Muehllehner, G. (1991). Factors affecting accuracy and precision in PET volume imaging. *J Cereb Blood Flow Metab*, 11(2):A38–44.

Kety, S. and Schmidt, C. (1948). The nitrous oxide method for the quantitative determination of cerebral blood flow in man: theory, procedure and normal values. *Journal of Clinical Investigations*, 27:476–483.

Kiebel, S. J., Goebel, R., and Friston, K. J. (2000). Anatomically informed basis functions. *Neuroimage*, 11(6 Pt 1):656–67.

Kinahan, P. E. and Rogers, J. G. (1989). Analytic 3D image-reconstruction using all detected events. *IEEE Transactions on Nuclear Science*, 36(1):964–968.

Kingsbury, N. (2001). Complex wavelets for shift invariant analysis and filtering of signals. *Applied and Computational Harmonic Analysis*, 10:234–253.

Koepp, M. J., Richardson, M. P., Brooks, D. J., Poline, J. B., Van Paesschen, W., Friston, K. J., and Duncan, J. S. (1996). Cerebral benzodiazepine receptors in hippocampal sclerosis. An objective in vivo analysis. *Brain*, 119 (Pt 5):1677–87.

Labbé, C., Froment, J. C., Kennedy, A., Ashburner, J., and Cinotti, L. (1996). Positron emission tomography metabolic data corrected for cortical atrophy using magnetic resonance imaging. *Alzheimer Dis Assoc Disord*, 10(3):141–70.

Labbé, C., Koepp, M. J., Ashburner, J., Spinks, T., Richardson, M., Duncan, J., and Cunningham, V. J. (1998). Absolute PET quantification with correction for partial volume effects within cerebral structures. In Carson, R. E., Daube-Witherspoon, M. E., and Herscovitch, P., editors, *Quantative Functional Brain Imaging with Positron Emission Tomography*, pages 59–66. Academic Press.

Laird, N., Lange, N., and Stram, D. (1987). Maximum likelihood computations with repeated measures: Application of the em algorithm. *Journal of the American Statistical Association*, 82(397):97–105.

Lammertsma, A. A. and Hume, S. P. (1996). Simplified reference tissue model for PET receptor studies. *Neuroimage*, 4(3):153–8.

Lange, K. and Carson, R. E. (1984). Em reconstruction algorithms for emission and transmission tomography. *Journal of Computer Assisted Tomography*, 8:306–316.

Lange, N. and Zeger, S. (1997). Non-linear fourier time series analysis for human brain mapping by functional magnetic resonance imaging. *Journal of the Royal Statistical Society Applied Statistics*, 46(1):1–29.

Laruelle, M. (2000). Imaging synaptic neurotransmission with in vivo binding competition techniques: a critical review. *J Cereb Blood Flow Metab*, 20(3):423–51.

Law, I., Iida, H., Holm, S., Nour, S., Rostrup, E., Svarer, C., and Paulson, O. B. (2000). Quantitation of regional cerebral blood flow corrected for partial volume effect using ^{15}O-water and PET: Ii. normal values and gray matter blood flow response to visual activation. *J Cereb Blood Flow Metab*, 20(8):1252–63.

Lawson, C. L. and Hanson, R. J. (1974). *Solving Least Squares Problems*. Prentice-Hall, New York.

Leahy, R. M. and Qi, J. Y. (2000). Statistical approaches in quantitative positron emission tomography. *Statistics and Computing*, 10(2):147–165.

Lemieux, L., Hagemann, G., Krakow, K., and Woermann, F. G. (1999). Fast, accurate, and reproducible automatic segmentation of the brain in T1-weighted volume MRI data. *Magn Reson Med*, 42(1):127–35.

Logan, J., Fowler, J. S., Volkow, N. D., Wolf, A. P., Dewey, S. L., Schlyer, D. J., MacGregor, R. R., Hitzemann, R., Bendriem, B., Gatley, S. J., and et al. (1990). Graphical analysis of reversible radioligand binding from time-activity measurements applied to [n-11c-methyl]-(-)-cocaine PET studies in human subjects. *J Cereb Blood Flow Metab*, 10(5):740–7.

Lucignani, G., Schmidt, K. C., Moresco, R. M., Striano, G., Colombo, F., Sokoloff, L., and Fazio, F. (1993). Measurement of regional cerebral glucose-utilization with fluorine-18-FDG and PET in heterogeneous tissues - theoretical considerations and practical procedure. *Journal of Nuclear Medicine*, 34(3):360–369.

Ma, Y. and Evans, A. (1997). Analytical modeling of PET imaging with correlated functional and structural images. *IEEE Trans Nucl Sci*, 44:2439–2444.

Ma, Y., Kamber, M., and Evans, A. C. (1993). 3D simulation of PET brain images using segmented MRI data and positron tomograph characteristics. *Comput Med Imaging Graph*, 17(4-5):365–71.

Mazziotta, J. C., Phelps, M. E., Plummer, D., and Kuhl, D. E. (1981). Quantitation in positron emission computed tomography: 5. physical–anatomical effects. *J Comput Assist Tomogr*, 5(5):734–43.

McColl, J., Holmes, A. P., and Ford, I. (1994). Statistical methods in neuroimaging with particular application to emission tomography. *Statistical Methods in Medical Research*, 3:63–86.

McCullagh, P. and Nelder, J. A. (1989). *Generalized linear models*. Chapman and Hall, London New York, 2nd – edition.

McIntosh, A. R. (1998). Understanding neural interactions in learning and memory using functional neuroimaging. *Ann N Y Acad Sci*, 855:556–71.

McKeown, M., Jung, T.-P., Makeig, S., Brown, G., Kindermann, S., Lee, T.-W., and Sejnowski, T. (1998). Spatially independent activity patterns in functional MRI data during the stroop color-naming task. *Proc Natl Acad Sci U S A*, 95(3):803–810.

Meltzer, C. C., Cantwell, M. N., Greer, P. J., Ben-Eliezer, D., Smith, G., Frank, G., Kaye, W. H., Houck, P. R., and Price, J. C. (2000). Does cerebral blood flow decline in healthy aging? a PET study with partial-volume correction. *J Nucl Med*, 41(11):1842–8.

Meltzer, C. C., Leal, J. P., Mayberg, H. S., Wagner, H. N., J., and Frost, J. J. (1990). Correction of PET data for partial volume effects in human cerebral cortex by MR imaging. *J Comput Assist Tomogr*, 14(4):561–70.

Mintun, M. A., Raichle, M. E., Kilbourn, M. R., Wooten, G. F., and Welch, M. J. (1984). A quantitative model for the in vivo assessment of drug binding sites with positron emission tomography. *Ann Neurol*, 15(3):217–27.

Muehllehner, G. and Colsher, J. (1982). Instrumentation. In Ell, P. and Holman, B., editors, *Computed Emission Tomography*, pages 3–41. Oxford University Press, Oxford.

Muller-Gartner, H. W., Links, J. M., Prince, J. L., Bryan, R. N., McVeigh, E., Leal, J. P., Davatzikos, C., and Frost, J. J. (1992). Measurement of radiotracer concentration in brain gray matter using positron emission tomography: MRI-based correction for partial volume effects. *J Cereb Blood Flow Metab*, 12(4):571–83.

Nichols, T. E. and Holmes, A. P. (2002). Nonparametric permutation tests for functional neuroimaging: A primer with examples. *Human Brain Mapping*, 15:1–25.

Nowak, R. and Baraniuk, R. (1999). Wavelet-domain filtering for photon imaging systems. *IEEE Transactions on Image Processing*, 8(5):666–678.

Ogawa, S., Lee, T. M., Kay, A. R., and Tank, D. W. (1990). Brain magnetic resonance imaging with contrast dependent on blood oxygenation. *Proc Natl Acad Sci U S A*, 87(24):9868–72.

Pajevic, S., Daube-Witherspoon, M. E., Bacharach, S. L., and Carson, R. E. (1998). Noise characteristics of 3-D and 2-D PET images. *IEEE Trans Med Imaging*, 17(1):9–23.

Patlak, C., Blasberg, R., and Fenstermacher, J. D. (1983). Graphical evaluation of blood-to-brain transfer constants from multiple-time uptake data. *Journal of Cerebral Blood Flow and Metabolism*, 3:1–7.

Price, J. C., Mayberg, H. S., Dannals, R. F., Wilson, A. A., Ravert, H. T., Sadzot, B., Rattner, Z., Kimball, A., Feldman, M. A., and Frost, J. J. (1993). Measurement of benzodiazepine receptor number and affinity in humans using tracer kinetic modeling, positron emission tomography, and c-11 flumazenil. *Journal of Cerebral Blood Flow and Metabolism*, 13(4):656–667.

Rao, C. R. and Mitra, S. K. (1971). *Generalized inverse of matrices and its applications*. Wiley, New York.

Raz, J. and Turetsky, B. (1999). Wavelet ANOVA and fMRI. In *Wavelet Applications in Signal and Image Processing VII*, volume 3813, pages 561–570. SPIE.

Rice, J. A. (1995). *Mathematical statistics and data analysis*. Duxbury Press, Belmont, CA, 2nd edition.

Richardson, M. P., Koepp, M. J., Brooks, D. J., Fish, D. R., and Duncan, J. S. (1996). Benzodiazepine receptors in focal epilepsy with cortical dysgenesis: an ^{11}C-flumazenil PET study. *Ann Neurol*, 40(2):188–98.

Rousset, O., Ma, Y., Kamber, M., and Evans, A. C. (1993). 3D simulations of radiotracer uptake in deep nuclei of human brain. *Comput Med Imaging Graph*, 17(4-5):373–9.

Rousset, O. G., Deep, P., Kuwabara, H., Evans, A. C., Gjedde, A. H., and Cumming, P. (2000). Effect of partial volume correction on estimates of the influx and cerebral metabolism of 6-^{18}F-fluoro-l-dopa studied with PET in normal control and Parkinson's disease subjects. *Synapse*, 37(2):81–9.

Rousset, O. G., Ma, Y., and Evans, A. C. (1998). Correction for partial volume effects in PET: principle and validation. *J Nucl Med*, 39(5):904–11.

Ruttimann, U. E., Unser, M., Rawlings, R. R., Rio, D., Ramsey, N. F., Mattay, V. S., Hommer, D. W., Frank, J. A., and Weinberger, D. R. (1998). Statistical analysis of functional MRI data in the wavelet domain. *IEEE Trans Med Imaging*, 17(2):142–54.

Ruttimann, U. E., Unser, M., Rio, D., and Rawlings, R. R. (1994). Use of the wavelet transform to investigate differences in brain PET images between patients. In *Mathematical Methods in Medical Imaging II*, volume 2035. SPIE.

Schmidt, K. (1999). Which linear compartmental systems can be analyzed by spectral analysis of PET output data summed over all compartments? *J Cereb Blood Flow Metab*, 19(5):560–9.

Schneider, M. K. and Willsky, A. S. (2001). Krylov subspace estimation. *Siam Journal on Scientific Computing*, 22(5):1840–1864.

Searle, S. R., Casella, G., and McCulloch, C. E. (1992). *Variance components*. Wiley series in probability and mathematical statistics. Applied probability and statistics. Wiley, New York.

Seber, G. and Wild, C. (1989). *Nonlinear Regression*. Wiley.

Slifstein, M. and Laruelle, M. (2000). Effects of statistical noise on graphic analysis of PET neuroreceptor studies. *J Nucl Med*, 41(12):2083–8.

Slifstein, M., Mawlawi, O., and Laruelle, M. (2001). Partial volume effect correction: Methodological considerations. In Gjedde, A., Hansen, S., Knudsen, G., and Paulson, O., editors, *Physiological Imaging of the Brain with PET*, pages 65–71. Academic Press.

Sokoloff, L., Reivich, M., Kennedy, C., Des Rosiers, M. H., Patlak, C. S., Pettigrew, K. D., Sakurada, O., and Shinohara, M. (1977). The ^{14}C-deoxyglucose method for the measurement of local cerebral glucose utilization: theory, procedure, and normal values in the conscious and anesthetized albino rat. *J Neurochem*, 28(5):897–916.

Strafella, A. P., Paus, T., Barrett, J., and Dagher, A. (2001). Repetitive transcranial magnetic stimulation of the human prefrontal cortex induces dopamine release in the caudate nucleus. *J Neurosci*, 21(15):RC157.

Studholme, C., Hill, D. L., and Hawkes, D. J. (1997). Automated three-dimensional registration of magnetic resonance and positron emission tomography brain images by multiresolution optimization of voxel similarity measures. *Med Phys*, 24(1):25–35.

Taylor, J. E. (2001). *Euler characteristics for Gaussian fields on manifolds*. PhD, McGill University.

Turkheimer, F., Aston, J. A., Banati, R. B., Riddell, C., and Cunningham, V. J. (2002a). A linear wavelet filter for parametric imaging with dynamic PET. *IEEE Trans Med Imaging*, page in revision.

Turkheimer, F., Aston, J. A. D., and Cunningham, V. J. (2002b). A "no free lunch" theorem for neuroimaging. *Neuroimage*, page submitted.

Turkheimer, F., Sokoloff, L., Bertoldo, A., Lucignani, G., Reivich, M., Jaggi, J. L., and Schmidt, K. (1998). Estimation of component and parameter distributions in spectral analysis. *J Cereb Blood Flow Metab*, 18(11):1211–22.

Turkheimer, F. E., Banati, R. B., Visvikis, D., Aston, J. A., Gunn, R. N., and Cunningham, V. J. (2000a). Modeling dynamic PET-SPECT studies in the wavelet domain. *J Cereb Blood Flow Metab*, 20(5):879–93.

Turkheimer, F. E., Brett, M., Aston, J. A., Leff, A. P., Sargent, P. A., Wise, R. J., Grasby, P. M., and Cunningham, V. J. (2000b). Statistical modeling of positron emission tomography images in wavelet space. *J Cereb Blood Flow Metab*, 20(11):1610–8.

Turkheimer, F. E., Brett, M., Visvikis, D., and Cunningham, V. J. (1999). Multiresolution analysis of emission tomography images in the wavelet domain. *J Cereb Blood Flow Metab*, 19(11):1189–208.

Turner, R., Howseman, A., Rees, G., and Josephs, O. (1997). Functional imaging with magnetic resonance. In Frackowiak, R., Friston, K., Frith, C., Dolan, R., and Mazziotta, J. C., editors, *Human Brain Function*, pages 467–86. Academic Press, London.

Verhoeff, N. (2001). Imaging of dopaminergic transmission in neuropsychiatric disorders. *Current Opinion in Psychiatry*, 14(3):227–239.

Vidakovic, B. (1999). *Statistical Modeling by Wavelets*. Wiley, New York.

Vidakovic, B. and Muller, P. (1999). An introduction to wavelets. In Muller, P. and Vidakovic, B., editors, *Bayesian Inference in Wavelet-Based Models*. Springer, New York.

Watson, C. C., Newport, D., and Casey, M. (1996). A single-scatter simulation technique for scatter correction in 3D PET. In Amans, P. G. and JL, editors, *Three-Dimensional Image Reconstruction in Radiation and Nuclear Medicine.*, pages 255–268. Kluwer Academic Publishers, Dordrecht.

Westbrook, C. and Kaut, C. (1998). *MRI in Practice*. Blackwell Science, Oxford.

Worsley, K., Marrett, S., Neelin, P., and Evans, A. (1996a). Searching scale space for activation in PET images. *Human Brain Mapping*, 4:74–90.

Worsley, K., Marrett, S., Neelin, P., Vandal, A., Friston, K., and Evans, A. (1996b). A unified statistical approach for determining significant signals in images of cerebral activation. *Human Brain Mapping*, 4:58–73.

Worsley, K. J. (1994). Local maxima and the expected euler characteristic of excursion sets of χ^2, F and t fields. *Advances in Applied Probability*, 26:13–42.

Worsley, K. J., Evans, A. C., Marrett, S., and Neelin, P. (1992). A three-dimensional statistical analysis for CBF activation studies in human brain. *J Cereb Blood Flow Metab*, 12(6):900–18.

Worsley, K. J., Liao, C., Aston, J. A., Petre, V., Duncan, G., and Evans, A. C. (2002). A general statistical analysis for fMRI data. *Neuroimage*, 15(1):1–15.

UNIV.